ALMA MATER STUDIORUM
UNIVERSITÀ DI BOLOGNA

DOTTORATO DI RICERCA IN

AUTOMOTIVE ENGINEERING FOR INTELLIGENT MOBILITY

Ciclo 38

Settore Concorsuale: 09/B1 - TECNOLOGIE E SISTEMI DI LAVORAZIONE

Settore Scientifico Disciplinare: ING-IND/16 - TECNOLOGIE E SISTEMI DI LAVORAZIONE

PHYSICS-INFORMED NEURAL NETWORK (PINN) – BASED MODELLING AND POST-PROCESSING INVESTIGATION IN LASER POWDER BED FUSION (LPBF) OF ALUMINUM ALLOYS

Presentata da: Dexiang Zha

Coordinatore Dottorato

Davide Moro

Supervisore

Alessandro Fortunato

Co-supervisore

Erica Liverani

Esame finale anno 2026

Contents

Abstract:

Laser Powder Bed Fusion (LPBF), as a representative technique of metal additive manufacturing, demonstrates tremendous potential for producing complex, high-performance metal components. However, the process still faces critical challenges in thermal behavior modelling, process parameter optimization, and performance enhancement. Traditional numerical methods, such as the Finite Element Method (FEM) and Computational Fluid Dynamics (CFD), can accurately capture the temperature evolution and melt pool dynamics but suffer from extremely high computational costs and parameter sensitivity, making them unsuitable for fast or real-time process prediction. In contrast, data-driven machine learning models are computationally efficient but rely heavily on large experimental datasets and lack physical consistency and generalization capability. Furthermore, for high-performance aluminum alloys—Scalmalloy® (Al–Mg–Sc–Zr)—systematic investigations remain limited. Although Scalmalloy® exhibits superior strength and fatigue performance in LPBF processing, the understanding of its post-processing behavior, surface integrity, and performance-response mechanisms remains incomplete, hindering its broader industrial application.

To address the aforementioned issues, this study aims to improve the modelling accuracy and performance stability of the LPBF process through a systematic investigation covering two main stages: pre-process temperature field modelling and parameter calibration, and post-process performance optimization. The goal is to provide new theoretical support and technical pathways for rapid temperature field prediction, process parameter optimization, and performance enhancement in LPBF.

Firstly, in the modelling stage, focusing on the thermal conduction mechanisms and numerical modelling challenges of the keyhole-mode LPBF process, a three-dimensional transient heat transfer model was developed based on the Physics-Informed Neural Network (PINN) framework. The model embeds the heat conduction equation and boundary conditions directly into the neural network loss function, enabling high-accuracy temperature prediction under limited or unsupervised data conditions. A double-conical volumetric heat source was employed to describe the energy distribution in the keyhole regime, providing both geometric tunability and physical interpretability, while also being extendable to conduction-mode melting. Through systematic optimization of hyperparameters and sampling strategies, the constructed PINN model achieved high prediction accuracy with a computational cost reduced by several orders of magnitude compared with traditional CFD models, significantly improving modelling efficiency.

Secondly, in the model calibration and validation stage, an automatic heat source parameter calibration method was developed by integrating Pearson correlation-based sensitivity analysis with inverse optimization. Experimental results demonstrated that the lower cone height (H_l) and top radius (R_t) are the key parameters governing melt pool depth and width, respectively. By establishing empirical mappings between these parameters and the laser process variables (power and scanning speed) through inverse analysis, the PINN model acquired physically consistent self-adaptive calibration capability. Comparative validation against experimental measurements and CFD simulations showed that the model achieved an average relative error below 5% in predicting melt pool geometry and could generate stable temperature field predictions within milliseconds, significantly outperforming traditional numerical simulations in both prediction efficiency and computational cost. Furthermore, a case study was carried out, the PINN rapidly identified the optimal power–speed combination to achieve the desired penetration depth, confirming the practical feasibility of this method in laser processing.

Finally, in the post-processing stage, a systematic investigation was conducted on high-strength Scalmalloy® (Al–Mg–Sc–Zr) components fabricated by LPBF to evaluate the effects of machining (M), shot peening (SP), and their combined treatment (M+SP) on surface and mechanical properties. The results revealed that shot peening induced a significant hardening effect up to a depth of approximately 200 μm, while generating beneficial compressive residual stresses extending to around 300 μm beneath the surface. Low-intensity shot peening (150 mm, 4 bar, 20 s) provided a favorable balance between surface smoothness and stress induction, whereas high-intensity peening further increased surface hardness but caused surface damage and ceramic particle embedding. Fatigue testing demonstrated that shot peening enhanced fatigue life by approximately 55–60%, with the combined machining and shot peening (M+SP) process exhibiting the best overall mechanical performance, offering an optimized route for improving both surface integrity and structural reliability of LPBF-processed Scalmalloy® components.

Key words: Physics-informed neural network; Laser powder bed fusion; Modeling; Post process; Aluminum alloy

Chapter 1 Introduction

1.1 Research Background and Significance

In recent years, laser technology has become a key enabler in industrial production, offering advantages such as low thermal load, high processing quality, fast processing speed, precise energy delivery to the workpiece, and a high degree of automation. The versatility of laser operations spans a wide range of processes, including additive-manufacturing microstructures [1][2], multi-material additive manufacturing [3], rapid additive manufacturing [4], directed energy deposition [5], cladding [6], hot-wire cladding [7], surface polishing [8][9], coatings [10], engraving [11], hardening [12], drilling [13], sintering [14], vision sensing [15], laser-assisted machining [16][17], laser-assisted milling [18], and marking [19].

Metal laser additive manufacturing has rapidly gained widespread industrial adoption due to its speed and precision. It includes LPBF and laser-directed energy deposition (LDED). LPBF is a widely used AM method that has attracted significant attention from both academia and industry [20][21]. The LPBF process involves multiple coupled physical fields-(1) solid mechanics, (2) solid-state transformations, (3) thermal fluid dynamics, and (4) particle dynamics—as illustrated in Fig. 1a. During LPBF, a series of complex physical and chemical phenomena occur. These include the absorption of laser energy, which induces localized heating within the powder; subsequent melting and solidification that transform the solid material into a liquid phase and then into solid crystals upon cooling; and rapid cooling rates that yield refined microstructures with unique properties. LPBF is a layer-by-layer manufacturing process in which each powder layer is melted by a laser beam scanned over the prescribed geometry, as shown in Fig. 1b. Owing to the smaller powder particles and tighter laser spot size, LPBF achieves higher dimensional accuracy and superior surface quality compared with other metal AM methods. When the powder is irradiated by the laser beam, transient interactions typically arise among the powder material, the laser, and the evolving states of the powder, leading to steep temperature gradients and high cooling rates [22]. These distinctive advantages promote grain refinement and thus offer substantial microstructural tailoring capability, which has driven the application of LPBF to a variety of alloy systems—including aluminum alloys—for processing and fabrication [23].

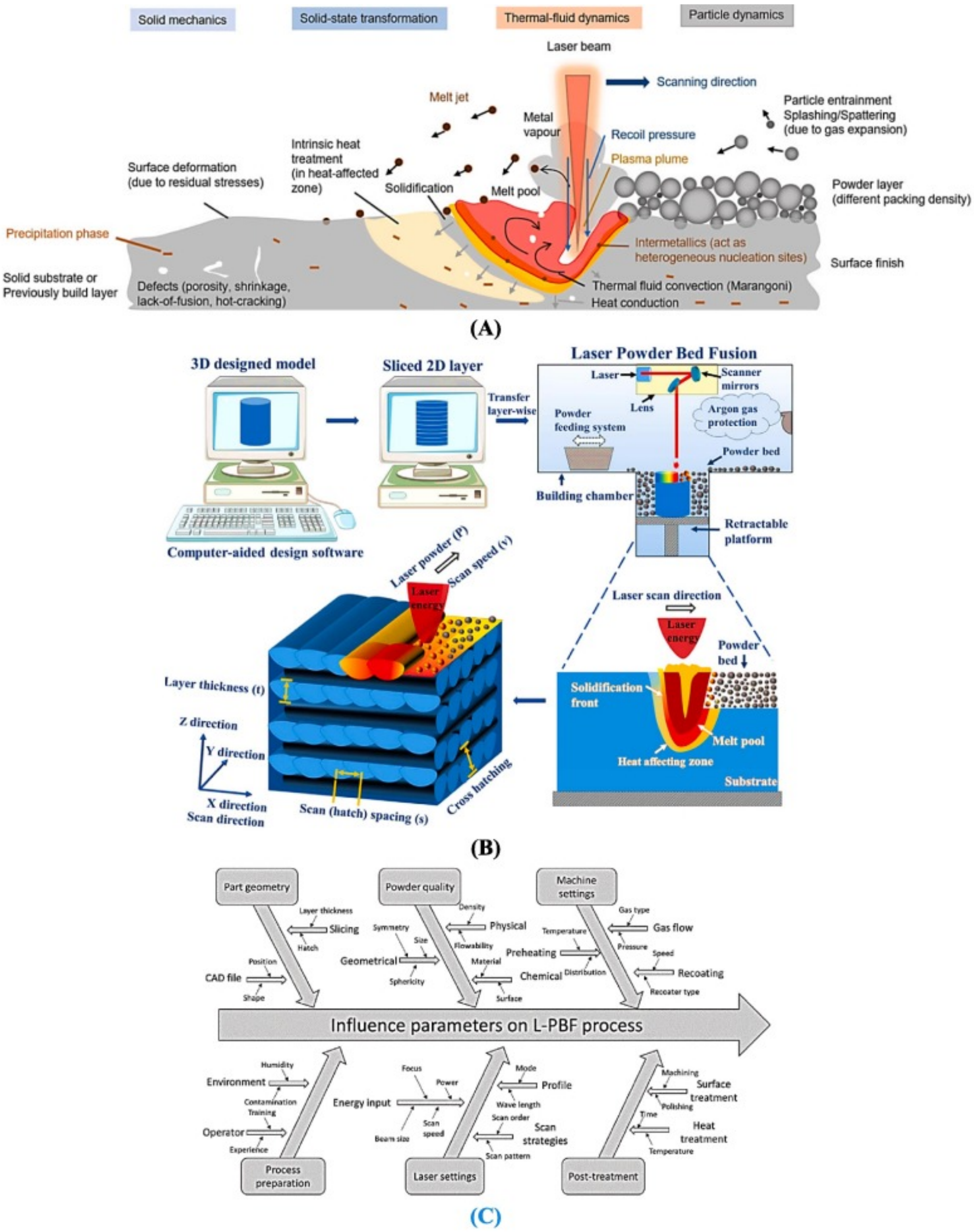

Fig. 1Schematic illustration of the Laser-Powder Bed Fusion (LPBF) process; A) Associated physical and chemical phenomena during the process of laser-powder interaction, solidification, and solid-state transformation[24],[25], B) Diagram of the process [26], C) The main influencing factors and processing parameters[27].

Despite these advantages, LPBF also faces significant challenges. Due to the complexity of the LPBF process, the large number of process parameters that are difficult to control, and the inherently multi-physics and multi-scale nature of the phenomena involved—including laser–powder interactions, melt pool dynamics, and grain growth—the process is prone to various defects. The difficulty in precisely tuning the numerous parameters can lead to the formation of pores, cracks, and other defects during fabrication, which severely affect the quality and service performance of the produced parts [28][29]. Figure 1c illustrates the main process parameters that influence LPBF production.

Typical LPBF defects—such as gas entrapment, lack of fusion (LoF), and keyhole porosity—can significantly degrade the mechanical and fatigue properties of printed components [30]. Phenomena such as balling, excessive surface roughness, and spatter adhesion may further deteriorate the surface quality. The formation of these defects is governed by the complex interplay of multiple factors, including processing parameters (e.g., laser characteristics such as scanning speed, laser power, and scanning strategy), material properties (e.g., powder morphology and particle size distribution), and environmental conditions (e.g., chamber atmosphere and temperature) [31].

In LPBF production, the primary concerns regarding part performance include mechanical properties (e.g. strength, hardness, and fatigue life) and surface quality, including surface roughness and dimensional accuracy. These properties directly determine the service reliability and operational lifespan of the manufactured components. However, due to the aforementioned complex physical mechanisms and strong parameter coupling, accurately predicting process characteristics and their influence on part performance remains highly challenging[32].

Optimization of part performance in LPBF production is typically pursued from three main perspectives:

(1) **Pre-processing stage:** Computational modelling and numerical simulation are employed to predict the laser-induced temperature field, melt pool dynamics, porosity formation, and microstructural evolution. These predictions enable proactive adjustment of process parameters by identifying potential defects or assessing their impact on material properties.

(2) **In-processing stage:** In-situ monitoring and in-process feedback control techniques are utilized for real-time defect detection, melt pool stability assessment, and quality prediction. Such approaches allow delayed or real-time adjustments of process parameters—such as laser power and scan speed—to prevent defect formation.

(3) **Post-processing stage:** Techniques such as heat treatment and surface strengthening are applied to further improve the microstructure and mechanical performance of the parts.

Moreover, the integration of these three stages provides a systematic framework for holistic process control and quality optimization throughout the entire LPBF production chain.

Current in-situ monitoring approaches in LPBF primarily aim to detect melt pool anomalies, porosity, and other defects by either extracting features from sensor data or applying deep learning algorithms for data classification. The monitoring data are mainly acquired from two categories of sensors: radiation-based sensors, which capture melt pool surface temperature, spatter, and plume dynamics, and non-radiation-based sensors, which record optical, acoustic, and other process-related signals.

In most cases, these monitoring systems perform inspection after the completion of a processed layer, followed by parameter adjustments for the subsequent layer. For example, infrared thermography is often employed to measure surface temperature distributions, analyze spatter and plume behavior, and assess thermal gradients. Similarly, X-ray diffraction imaging has been utilized to elucidate the effects of laser power on melt pool geometry, keyhole mode formation, and particle motion.

Nevertheless, the massive volume of data generated by these in-situ systems demands high-bandwidth data transmission and powerful computational algorithms for real-time processing. This requirement poses a substantial challenge to achieving genuine online defect detection. Consequently, most existing systems are limited to post-process analysis or delayed feedback control. Research on real-time, closed-loop feedback control in LPBF remains limited. Ensuring adequate processing speed during online control—particularly for real-time defect detection and reliable early warning generation—continues to be one of the most critical and unresolved issues in the field.

Although optimized process parameters can minimize defect formation to some extent, porosity in laser powder bed fusion (LPBF) components remains unavoidable. The surface integrity and structural soundness of LPBF-manufactured parts therefore continue to pose major challenges for industrial applications. Numerous studies have reported similar findings: fatigue failures are highly sensitive to surface defects, and the closer the pores are to the component surface, the more detrimental they become during cyclic loading, as they tend to serve as crack initiation sites leading to premature fracture [33][34]. Post-processing techniques can alleviate surface and subsurface defects, thereby creating favorable conditions for enhancing both surface and structural integrity. However, data on the effects of different post-processing treatments for LPBF-produced Scalmalloy components remain limited in the literature [35][36].

Therefore, to address the limitations of existing in-situ monitoring techniques in LPBF and the lack of systematic research on post-processing strategies for Scalmalloy components, this study primarily focuses on two critical stages of the LPBF process: the pre-processing stage, involving modelling and predictive analysis, and the post-processing stage, aimed at performance optimization.

In this study, focusing on the pre-processing stage of LPBF—a physics-informed neural network (PINN) model was developed for predicting the temperature field in keyhole-mode. Specifically, a double-conical heat source was incorporated into the PINN framework, and the model hyperparameters were optimized within a narrowed input domain. A transfer learning strategy was introduced to accelerate model convergence, while a limited set of experimental data was employed for inverse analysis to calibrate and validate the model accuracy. On this basis, the calibrated model was further applied to an aluminum alloy overlap welding case study. The near-instantaneous (<50 ms) PINN-predicted results exhibited good agreement with experimental observations in terms of melt pool morphology and temperature distribution., confirming the model's reliability and generalization capability under multiple process conditions. Finally, the potential of the proposed model for real-time temperature field monitoring and melt pool stability prediction during laser processing (corresponding to the second stage: real-time detection and control) was explored, along with its prospective extension to LPBF applications. This work establishes a solid foundation for developing an integrated online monitoring and control platform for laser welding and LPBF manufacturing processes.

On the post-processing stage, this study systematically investigates the effects of different post-treatment methods on the surface integrity and structural integrity of LPBF-produced components. The employed post-processing techniques include shot peening (SP), machining (M), and machining followed by shot peening (M+SP). By comprehensively analyzing the microstructure, hardness, tensile properties, fatigue performance, and residual stress, the study evaluates and compares the performance of Scalmalloy components subjected to different post-processing routes.

1.2 Research Status

This section analyzes the current development status from three aspects for optimizing the performance of LPBF-manufactured components: pre-processing modelling and prediction, in-process monitoring and control, and post-processing performance enhancement and integrity optimization of the fabricated LPBF parts.

1.2.1 Pre-processing Stage — Process Modelling and Prediction

Research in the pre-processing stage aims to predict heat transfer, melt pool dynamics, defect formation, and microstructural evolution during the laser processing stage through modelling and numerical simulation, thereby providing a theoretical basis for process parameter optimization. The following subsections classify the modelling approaches for LPBF pre-processing according to their methodological framework. As shown in Fig. 2, modelling of the Laser Powder Bed Fusion (LPBF) process can generally be divided into two main branches based on the modelling methodology and approach: (1) Theory-Based (TB) models and (2) Empirical-Based (EB) models.

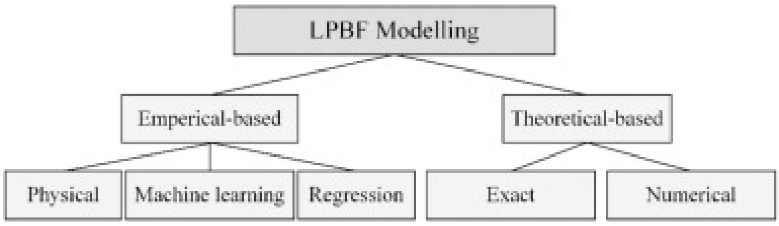

Fig. 2 Classification of LPBF modelling based on methods approach[37].

(1) Theoretical Models

Theory-based LPBF models are constructed according to the fundamental principles governing the laser beam welding process. Research in this area is generally divided into two subcategories: 1-Exact and 2- Numerical. Exact models derive process outputs based on the energy balance among the input, output, and losses during the laser beam welding process, providing exact solutions to the governing equations. Numerical models, including the finite element method (FEM) and various software-based approaches, are also employed to solve the theoretical equations that describe the process behavior.

[38] proposed a method based on thermal finite element simulation to calibrate the laser penetration depth and absorption rate, aiming to analyze the melt pool characteristics of Alloy 718 in LPBF. The results showed a strong correlation between these two parameters and the modified energy density: the penetration depth primarily influenced the melt pool depth, while the absorption rate determined the melt pool width. The calibrated results were consistent with both analytical models and experimental data, revealing the underlying physical mechanisms of the laser–melt pool interaction under varying energy inputs.

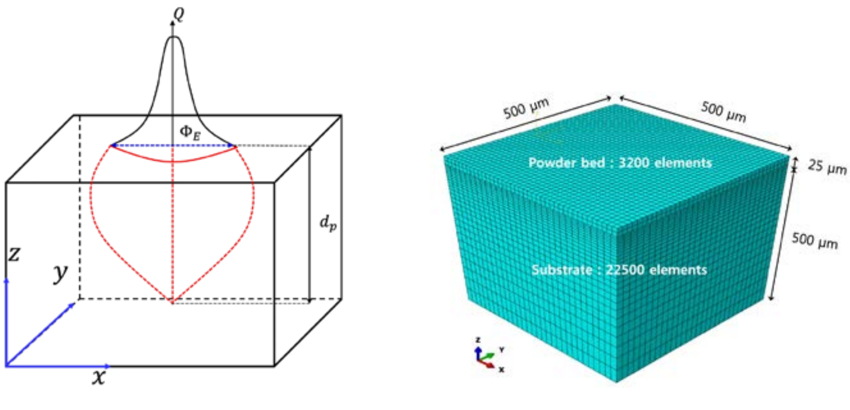

a) *b)*

Fig. 3 a) Illustration of the heat source model used in the present thermal FEM simulations b) Geometries for the substrate and powder bed for finite element method simulations of single track PBF

[39] investigated the influence of preheating temperature on the melt pool morphology of Inconel 718 during L-PBF through experiments combined with CtFD numerical simulations.

The results showed that increasing the preheating temperature significantly deepened the melt pool—by up to 49%—across the conduction, transition, and keyhole melting modes. In the keyhole region, higher preheating temperatures enhanced evaporation and recoil pressure effects, resulting in a deeper melt pool and longer melt tracks. This study elucidated the mechanistic role of preheating temperature in regulating melt pool dynamics and provided important insights for optimizing L-PBF process parameters.

[40] developed a multiphysics model combining the Discrete Element Method (DEM) and Computational Fluid Dynamics (CFD) to investigate the effect of layer thickness on the thermo-fluid behavior and single-track formation of AISI H13 steel during L-PBF, as illustrated in Fig. 4. The results indicated that layer thickness had a pronounced influence on melt pool depth: a smaller layer thickness (30 μm) reduced the melt depth due to enhanced heat conduction. By adjusting laser power and scan speed, the melt depth could be effectively controlled for different layer thicknesses. The simulations further revealed that a layer thickness of 50–70 μm, combined with a moderate energy density, yielded continuous melt tracks with sufficient penetration depth, providing valuable guidance for L-PBF process parameter optimization.

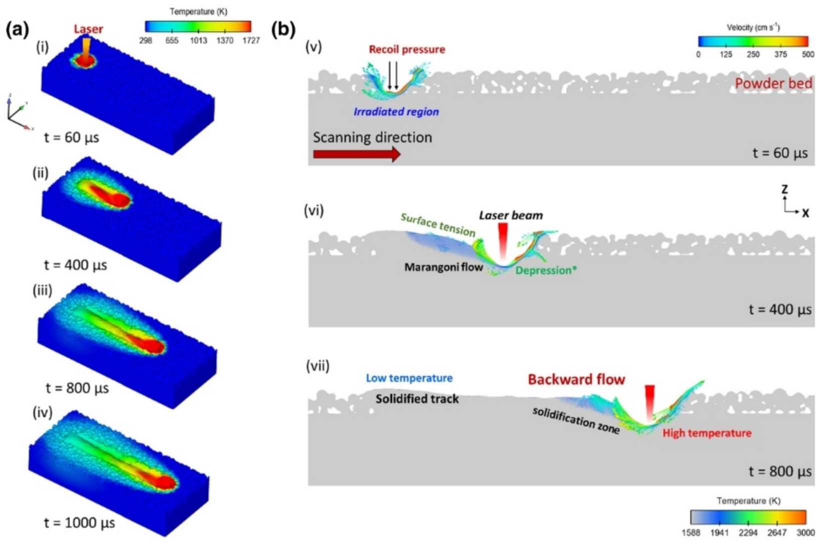

*Fig. 4 Temperature distribution at different times with laser power of 200 W, scanning speed of 1000 mm/s, LED of 0.2 J/mm, and layer thickness of 50 μm (**a**) and molten metal flow and velocity flow field (**b**)[40].*

[41] proposed a finite element thermal conduction model based on consolidation geometry to efficiently predict the temperature field and melting behavior of Inconel 718 during the LPBF process. The model accounts for phase transformation and the influence of powder consolidation on laser–material interaction, with the interaction parameters calibrated through experimental data. The results demonstrated that this approach can accurately predict melt pool dimensions and temperature distribution without explicitly simulating powder densification.

This method provides an efficient tool for the rapid thermal analysis and process optimization of multilayer LPBF fabrication.

[42] established a three-dimensional finite element heat transfer model to predict melt pool dimensions and surface morphology during the LPBF process, and conducted a comparative analysis of eight commonly used heat source models. To improve simulation accuracy, a new model incorporating anisotropy-enhanced thermal conductivity and variable laser absorptivity was proposed. Validation results showed that this model more accurately reproduced the experimental melt pool geometry and surface features, while the linear heat source formulation significantly enhanced predictive consistency with reduced model complexity. This modelling approach provides an efficient means for LPBF process parameter optimization.

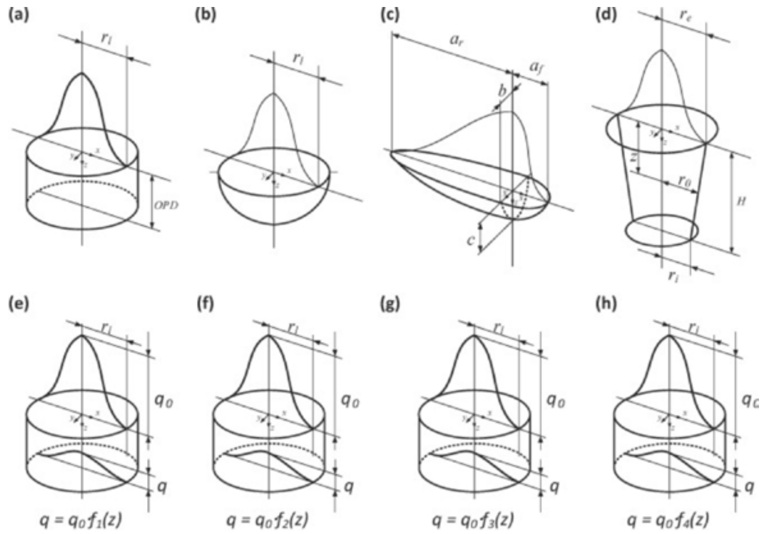

Fig. 5 Schematic representations of various heat source models used for melt pool modelling in LPBF (a) cylindrical shape, (b) semi-spherical shape, (c) semi-ellipsoidal shape, (d) conical shape, (e) radiation transfer method, (f) ray-tracing method, (g) linearly decaying method, (h) exponentially decaying method [42].

[43] developed a three-phase numerical model based on the Volume of Fluid (VOF) method to systematically investigate the heat transfer and fluid dynamics of the melt pool during the LPBF process. The model comprehensively accounts for surface tension, the Marangoni effect, recoil pressure, and laser energy absorption characteristics. The results revealed that the melt pool morphology is strongly influenced by laser power and scan speed, while larger layer thicknesses tend to cause unmelted powder and pore formation. The model successfully reproduced the key physical phenomena of powder melting and solidification in LPBF, providing a reliable numerical tool for understanding melt pool evolution mechanisms.

[44] proposed a multiscale finite element modelling framework for efficiently predicting warpage deformation and residual stress in LPBF-manufactured metal parts. The framework integrates three hierarchical levels: microscale, mesoscale, and macroscale. At the microscale,

the powder–melt–solidification phase transition is modeled to extract an effective heat source; at the mesoscale, intrinsic strain is derived; and at the macroscale, these data are utilized to rapidly compute the residual stress and deformation of large-scale components, as illustrated in Fig. 6. A simulation using a dual-cantilever beam as a case study demonstrated that this approach effectively reveals the influence of process parameters on structural responses, providing a multiscale analytical pathway for LPBF process optimization.

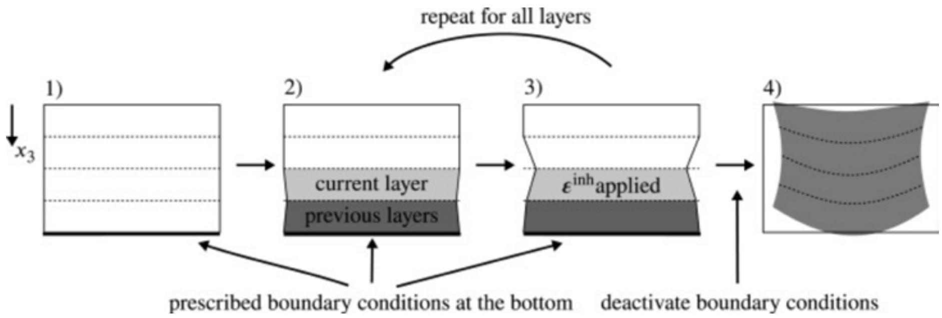

Fig. 6 Schematic view of layer activation concept: (1) all (solid) layers initially deactivated, (2) one current layer activated, (3) inherent strain ε^{Inh} applied as external load to current layer, (4) warpage of part after deactivation of boundary conditions.

[45] proposed an analytical model for predicting residual stress in LPBF, which accounts for volume conservation during plastic deformation. The model captures the interactions among thermal gradients, phase transformations, and plastic strains, linking thermal expansion during heating and contraction during cooling to stress formation. By incorporating densification and anisotropic deformation, the model is capable of predicting both tensile and compressive stress distributions, while also exploring the effects of key process parameters such as laser power and scan speed. This approach provides critical insights for optimizing LPBF process parameters to improve component quality and minimize defect formation.

Study[46] developed an analytical model to predict molten pool dimensions and vapor depression depth in the keyhole melting mode of LPBF, addressing the critical role of molten pool geometry in process-induced defects. The model combines a moving point heat source, representing plasma effects at the keyhole mouth, and a finite-length moving line heat source to account for laser power absorption along the keyhole walls. Using a closed-form solution for temperature distribution, the model determines molten pool width, depth, and vapor depression depth by comparing predicted temperatures with the material's melting and boiling points. Validated against experimental data for Ti6Al4V, the model demonstrates high accuracy and low computational cost, avoiding finite element simulations. Sensitivity analyses reveal the influence of process parameters, providing a practical tool for optimizing LPBF conditions to reduce defects and improve component quality.

Study[47] present a thermodynamically consistent phase transformation model tailored for multiphase alloys, with a specific application to Ti6Al4V in LPBF processes. The model integrates thermodynamic and kinetic principles to capture the complex interplay between thermal history, phase stability, and transformation kinetics in multiphase systems. By accounting for the rapid thermal cycles and non-equilibrium conditions inherent in LPBF, the model accurately predicts the evolution of microstructures, including the α-β phase transformations and their interactions. The framework incorporates energy dissipation, phase-field dynamics, and constitutive equations to ensure thermodynamic consistency across all phases. Validation against experimental data for Ti6Al4V alloys demonstrates the model's capability to predict phase fractions and transformation pathways under varying process conditions. This work offers a robust tool for understanding and optimizing the microstructural evolution in LPBF, enabling better control over mechanical properties and minimizing defects in fabricated components. The computed CCT, crystal structures of β- and α-phases and presented parameters are provided in parts A, B, and C of Fig. 7.

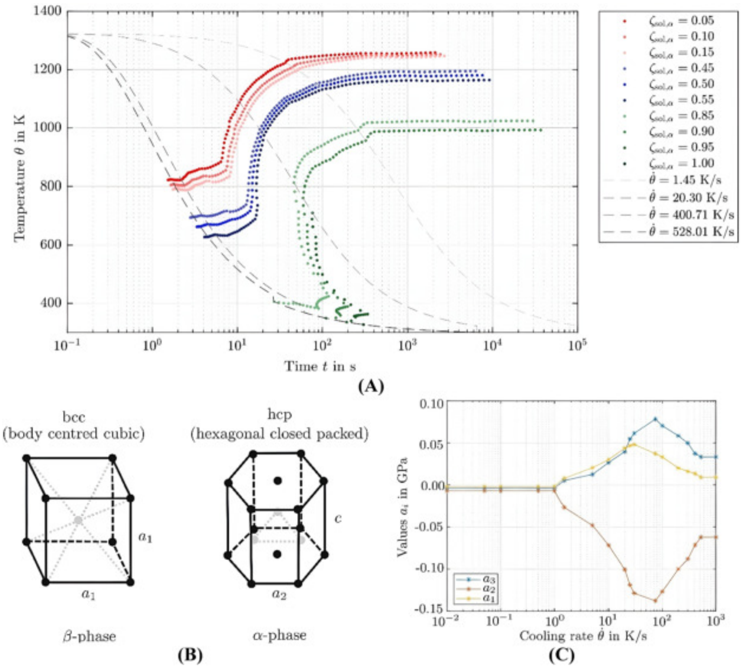

Fig. 7 A) Computed CCT diagram for 100 cooling rates (0.01–600 K/s) visualizing mass fractions $\zeta_{sol,\alpha}$, with four characteristic rates[47], B) Crystal structures of β- and α-phases of Ti6Al4V, with lattice parameters: a1 = 0.319 nm (bcc) and a2 = 0.2925 nm, c = 0.4670 nm (hcp) C) parameters a1, a2, a3 [47].

Study[48] propose an analytical model for predicting the quantitative texture of single-phase materials in LPBF, incorporating heat transfer dynamics. The model establishes a direct relationship between thermal gradients, cooling rates, and crystallographic texture evolution during the rapid solidification process of LPBF. By considering the directional heat flow and solidification behavior, it predicts the preferred grain orientations and texture intensity based on process parameters such as laser power, scan speed, and layer thickness. The study highlights the model's efficiency in capturing texture development without requiring computationally expensive numerical simulations. Validation with experimental data demonstrates its accuracy in predicting crystallographic texture for single-phase materials. This work provides a valuable framework for controlling microstructural anisotropy in LPBF, offering insights for optimizing process conditions to enhance material performance in various applications.

(2) Empirical Models

Empirical models for Laser Powder Bed Fusion (LPBF) establish relationships between process input parameters and process responses or performance outputs through data fitting or empirical correlations. The core concept of such models is to replace complex physical derivations with data-driven approaches, enabling rapid prediction and optimization. These models aim to construct a multiscale "Process–Thermodynamics–Structure–Performance (PTSP)" mapping framework, which links the entire chain from energy input (e.g., laser power, scanning speed) to melt pool behavior and microstructural evolution, and ultimately to part performance (e.g., strength, density, fatigue life).According to the modelling methodology, empirical models can be categorized into three types: ① Regression-based or traditional empirical models; ② Semi-empirical models based on simplified physics; and ③ Modern machine learning-based models.

① Regression and Semi-Empirical Models

Regression models are among the earliest forms of empirical modelling. They typically establish predictive relationships by fitting empirical curves between process input and output variables—such as laser power, scan speed, melt pool dimensions, and part density. Although these models provide limited physical interpretability, they offer high computational efficiency and are well-suited for the rapid estimation of process parameter windows.

[50]employed the Smoothed Particle Hydrodynamics (SPH) method to investigate the balling mechanism in single-track melt formation during PBF-LB/M. The results revealed that balling is primarily driven by the Marangoni effect and capillary forces, which cause melt accumulation at the tail and insufficient local deposition. After the onset of melt necking, the competition between spreading and contraction further influences balling formation. Although the balling characteristics were similar under different laser powers, their sizes varied. The study demonstrated that the SPH approach is capable of accurately capturing interfacial dynamics, providing an effective tool for elucidating the formation mechanism of balling defects in LPBF.

[51]developed an analytical model to construct a power–velocity (PV) process map capable of

predicting melt pool geometry and defect formation, thereby evaluating densification and defect distribution during the LPBF process. By combining the melt pool governing equations with defect criteria, the model enables rapid estimation of the process window for different materials, showing good agreement with experimental results. This study proposed an analytical-solution-based framework for process parameter design, providing an efficient guideline for LPBF process optimization of new metals and alloys.

Study[52] focuses on determining the α\alphaα-to-β\betaβ phase transformation kinetics in laser powder bed fused (LPBF) Ti–6Al–2Sn–4Zr–2Mo-0.08Si and Ti–6Al–4 V alloys. Utilizing a combination of experimental techniques and modelling, the research quantifies the transformation rates under various thermal conditions typical of LPBF processing. The study analyzes the effect of alloy composition, cooling rates, and thermal gradients on the transformation pathways, highlighting the distinct kinetics driven by the rapid solidification inherent to LPBF. By incorporating thermodynamic and kinetic principles, the authors provide insights into microstructural evolution, including grain morphology and phase stability, which are critical for optimizing mechanical properties such as strength and creep resistance. This work offers a valuable framework for tailoring post-processing heat treatments to achieve desired performance in LPBF-fabricated titanium alloys for aerospace and biomedical applications.

② Machine Learning-Based Modelling

In recent years, machine learning (ML) methods have been extensively explored for additive manufacturing (AM) process modelling, leveraging ML's powerful pattern recognition and data-driven capabilities to interpret process complexity. In general, ML techniques can be categorized into two learning paradigms—unsupervised learning and supervised learning—and four main application scenarios: clustering, dimensionality reduction, regression, and classification. The most widely adopted ML techniques have been summarized in [53][54].

The selection of an appropriate ML technique depends on various factors, including the application scenario (i.e., the four mentioned categories), the type of target system (e.g., linear vs. nonlinear, deterministic vs. probabilistic), the availability of labeled or unlabeled data, the response-time requirement (e.g., real-time vs. offline processing), and the available computational resources. Modelling the multiscale PTSP (Process–Thermodynamics–Structure–Performance) relationships is generally regarded as a multimodal nonlinear regression problem, since data collected from different printing stages vary in format and exhibit complex interdependencies. On the other hand, anomaly detection and process control tasks are typically formulated as classification problems.

Depending on the nature of the sensor data, different ML techniques may be applied—for example, multivariate regression and decision trees (DTs) for discrete feature data, support vector machines (SVMs) and neural networks for continuous time-series data, and convolutional neural networks (CNNs) for image or video frame data.

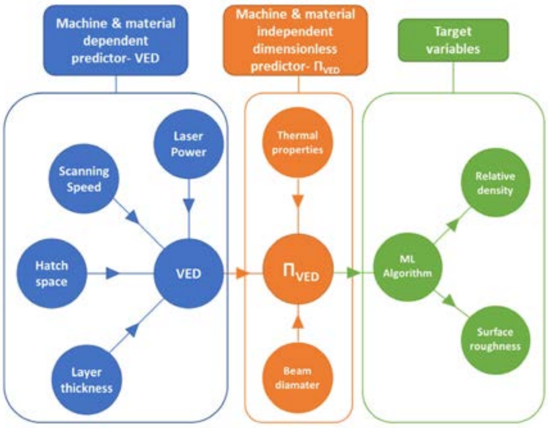

Fig. 8 Flow diagram describing the data curation approach for streamlining different parameters employed during ML-based prediction for LPBF

[55] addressed the challenge of achieving high density and good surface quality in Laser Powder Bed Fusion (LPBF) by employing six supervised machine learning algorithms, as illustrated in Fig. 8, to predict relative density and surface roughness based on only 33 experimental datasets. The results showed that using volumetric energy density as an input parameter significantly improved model accuracy, reducing the mean absolute percentage error (MAPE) by 30% and 21.94%, respectively. This dimensionless parameter enhanced the generality and transferability of the model. When the dataset was expanded to include different machines and materials, the model achieved R^2 values of 79.11% and 80.3% for density and roughness predictions, respectively, validating the effectiveness and generalization capability of the proposed approach.

[57] employed a statistical machine learning (ML) model to establish the correlation between the thermal history and subsurface porosity formation in laser-melted Ti-6Al-4V powder. When incorporating thermal history, the model was able to capture the complex distribution of heat accumulation within actual components—an effect that models relying solely on laser and basic build parameters could not reproduce. The location and type of pores were extracted from high-speed X-ray imaging, while the thermal history was obtained from infrared (IR) thermography, as shown in Fig. 9(left). For each experiment, the energy density (J/mm^3) was calculated and compared with the maximum observed porosity, as illustrated in Fig. 9(right). A total of 15 experiments were conducted, covering seven laser power levels, six scanning speeds, two scanning strategies, and different laser spot sizes. The relationship between porosity and

thermal history features was established by combining physical insights with computational reasoning, focusing particularly on the locations of overheating, which are most likely to induce instability and porosity formation.

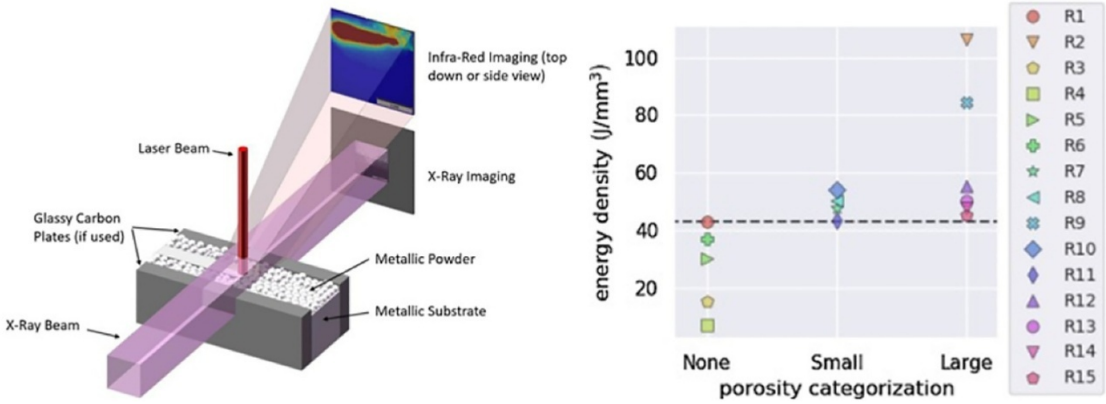

Fig. 9. The thermal history-subsurface porosity correlation (left: the experimental setup; right: the porosity categorization versus energy density in each experiment) [57].

[58]investigated the relationship between porosity characteristics (such as maximum pore size, pore number, and pore location) and fatigue life of LPBF-fabricated Inconel 718 components using Kernel Regression (KR), Support Vector Regression (SVR), and Kernel Ridge Regression (KRR) [94]. The results showed that an increase in pore size and number, as well as a decrease in the distance between pores and the specimen surface, led to a reduction in fatigue life. Furthermore, ML and statistical analysis results indicated that fatigue life was most strongly correlated with pore location compared with pore size and number; when the effects of pore location, size, and number were excluded, the R-squared (R^2) values decreased by 75.1%, 47.9%, and 4.16%, respectively.

In another study [59], an Artificial Neural Network (ANN) was applied to correlate local pore features (such as size, shape, volume fraction, and porosity distribution) with the evolution of local strain, plastic anisotropy, and fracture behavior during the tensile deformation of LPBF-produced AlSi10Mg, as illustrated in Fig. 10. The developed model successfully predicted the strain values, the locations of crack initiation during tensile loading, and the evolution of small-scale plastic anisotropy. A key highlight of this study is that, during the data processing stage, unsupervised learning was employed to identify pixels belonging to pores and aggregate them into pore structures, thereby improving the efficiency of data processing.

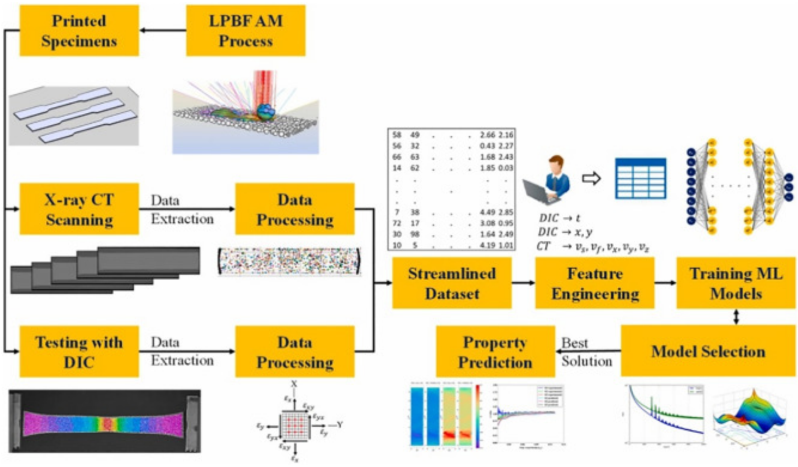

Fig. 10 ANN framework for the prediction of the local strains and tensile fracture, from[59].

[60] proposed a Gaussian Process (GP)-based surrogate modelling approach to establish material data standards for the L-PBF process and to achieve robust partitioning of processing regimes for different materials. The model predicts melt pool depth using laser power, scanning speed, and spot size, and generates power–velocity maps to distinguish between conduction and keyhole melting regions. The results showed that the proposed statistical framework exhibits strong robustness against low-quality experimental data, and that high-fidelity numerical simulations can effectively replace experiments for model training, providing an efficient method for the rapid evaluation of L-PBF processability of new materials.

[61]A Physics-Informed Neural Network (PINN) incorporating physical principles into the loss function was developed to characterize and predict the temperature and melt pool fluid dynamics (i.e., velocity, pressure, and temperature) of LPBF-fabricated Inconel 625 samples. The study integrated momentum, mass, and energy conservation into the loss function to regularize and accelerate network training and derived Dirichlet boundary conditions for melt pool velocity, pressure, and temperature from these conservation parameters. Using the established PINN framework, three different sets of process parameters were investigated to estimate melt pool length, width, depth, and solidification cooling rate (see Fig. 11). The results were further compared with FEM and thermal model predictions reported in [63][64]. The developed PINN model demonstrated good accuracy in predicting temperature and melt pool dynamics during the LPBF process using only a moderately sized dataset; however, it cannot fully capture the complexities of AM processes, such as the surrounding gas phase and free surface deformation of the melt pool.

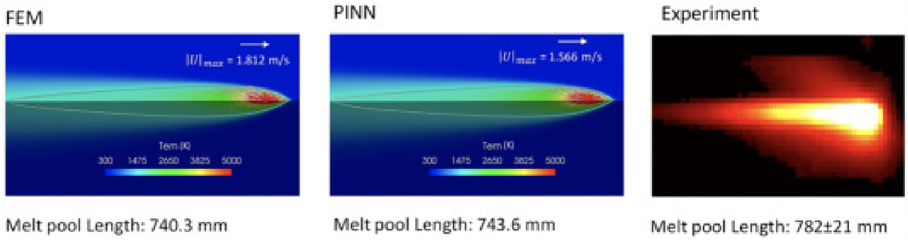

Fig. 11 Comparison of the predictions of temperature and melt pool fluid dynamics of FEM, PINN, and experiment [61]

[62] proposed a computational intelligence modelling approach based on Ensemble Multi-Gene Genetic Programming (EN-MGGP) to analyze the effects of SLS process parameters on properties such as porosity. The method enhances model generalization through statistical and classification strategies and outperforms the standard MGGP model. The results showed that EN-MGGP effectively identifies dominant process parameters and reveals nonlinear relationships in the SLS process, providing a more robust intelligent algorithmic framework for additive manufacturing process modelling and optimization.

[65]investigated the surface morphology of LPBF-fabricated Inconel 625 using focus variation microscopy, revealing the significant influence of energy density and scanning strategy on surface texture. A machine learning-based predictive model was developed to establish the relationship between process parameters and surface texture characteristics, enabling the prediction of surface quality. This study demonstrated the potential of data-driven approaches for process planning and optimization in LPBF.

1.2.2 In-Processing Stage — Process Monitoring and Control

Research in the in-process stage focuses on real-time quality monitoring and defect detection during the laser processing stage, aiming to identify defects in a timely manner and adjust process parameters accordingly. Depending on whether real-time feedback control is implemented, such methods can be categorized into **in-situ feedback control** and **in-process feedback control**. Fig. 12 illustrates the general framework of an ML-supported LPBF feedback control loop.

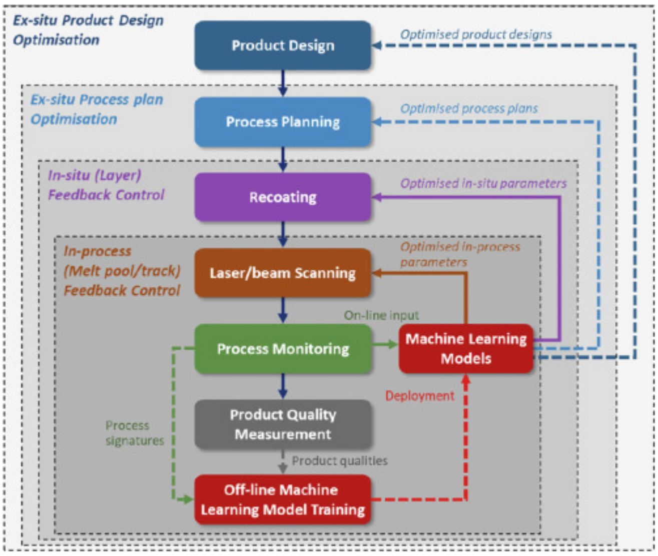

Fig. 12 Generic framework of ML-enabled feedback loops for LPBF process[66].

Compared with post-process structural scanning and performance testing, in-situ sensing (e.g., layer-wise optical and thermal monitoring) enables defect detection, quality prediction, and process adjustment for defect compensation and quality assurance during the build process. Grasso and Colosimo [67] summarized the common defects in LPBF processes—such as porosity, residual stress and cracking, balling, and geometric deviations—their root causes, and the commercial sensing tools and process features applicable for in-situ detection of each defect type. Yadav et al. [68] further expanded this summary of in-situ monitoring systems for LPBF. The two most commonly used sensing methods for in-situ quality monitoring are thermal imaging and optical imaging, as they provide direct information related to melt pool behavior, geometry, and structural defects. Acoustic and energy-based sensing approaches have also been investigated as cost-effective indirect methods for quality monitoring and defect detection.

Regarding sensor data analysis, two common approaches are employed: (1) feature extraction—typically based on domain knowledge—combined with classification, and (2) direct classification of raw data or images using deep learning techniques. Among various deep learning architectures, Convolutional Neural Networks (CNNs) have been extensively studied due to their strong capability in automatically representing spatiotemporal patterns and performing image classification.

Mahmoudi et al. [69] proposed a systematic approach for processing layer-wise melt pool images and identifying anomalous fabrication in LPBF of 17-4 PH stainless steel. The method involves combining multiple melt pool images into a single image representing each printed layer, filtering potential regions of interest (ROIs) through pixel binarization, quantifying the spatial patterns of ROIs using Gaussian Process (GP) regression, and classifying these spatial patterns based on ROI labels obtained from offline inspection.

Mitchell et al. [70] investigated high-temperature imaging techniques for detecting pore formation in LPBF of 316L stainless steel. By analyzing volumetric images obtained from sequential high-temperature imaging, melt pool characteristics such as size, shape, and orientation were extracted. The results showed that anomalous melt pool images typically contained multiple discontinuous high-temperature regions distributed asymmetrically, resulting in outliers in the relationship between melt pool aspect ratio and orientation, as shown in Fig. 13. Therefore, these features can be used as indicators of porosity percentage. Although neighborhood search techniques were explored to correlate these features with defect percentages, other classification methods achieved comparable or even better performance. Similarly, weld pool characteristics such as fusion zone profile height were found to effectively reveal geometric defects [71].

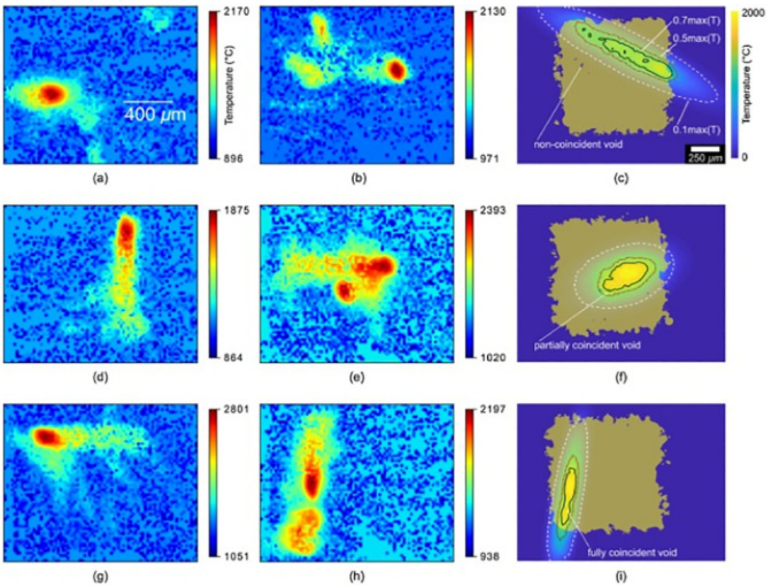

Fig. 13 Normal pyrometry images (left column), abnormal pyrometry images (middle column), fitted ellipse (right column) for each outlier image overlaid on micro-CT data that could reveal pool aspect[70].

Gobert et al. [72] applied a high-resolution digital single-lens reflex (DSLR) camera for in-situ anomaly detection in LPBF of stainless steel. Optical images collected from adjacent layers were fused and fed into a 3D convolutional filter for feature extraction. The extracted features were then classified into two categories—normal build and undesired defect occurrence—using an ensemble SVM-based binary classifier. Owing to the hierarchical representation capability of deep learning, the acquired in-situ images could be directly processed and classified without the need for preprocessing or manual feature extraction. Snow et al. further investigated hierarchical defect detection using CNNs and reported that direct image classification based on CNNs achieved better performance than feature extraction and classification using conventional ANNs [73]. Caggiano et al. [74] also studied in-situ optical inspection for detecting structural defects—such as track discontinuities and insufficient layer densification—in LPBF of pre-alloyed Inconel 718 powder, which are typically caused by improper process settings. Unlike methods relying solely on part surface images, this study also incorporated powder layer images, since the surface texture of the powder layer is influenced by the preceding manufactured layer and may affect the surface pattern of subsequent layers. Therefore, a dual-stream CNN was developed to integrate images from both domains, as shown in Fig. 14. A performance comparison of commonly used optical inspection and classification techniques showed that the dual-stream CNN achieved a classification accuracy of 99.4%, outperforming other ML-based methods.

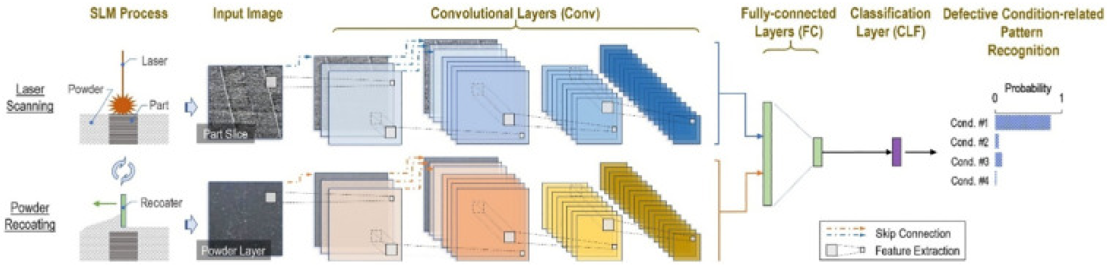

Fig. 14 The bi-stream CNN for recognition of defects induced by improper process conditions, from [74] .

Acoustic sensing has also been evaluated for process monitoring and defect detection in LPBF. Unlike image processing and pattern analysis, acoustic time-series data typically require analysis in the time–frequency domain to reveal how frequency components evolve over time. Shevchik et al. [75][76] investigated the application of acoustic emission for in-situ porosity estimation in LPBF of stainless steel. Acoustic signals were collected using a fiber Bragg grating sensor and converted into time–frequency spectra through standard wavelet packet transformation. The resulting spectrograms were then processed using a CNN to classify porosity into three levels (1.42 ± 0.85%, 0.3 ± 0.18%, and 0.07 ± 0.02%), achieving an average classification accuracy of 85%.

Although the aforementioned monitoring approaches perform well in layer-wise inspection and defect identification, they generate massive amounts of data that require high bandwidth and substantial computational resources for real-time processing. Consequently, most in-situ systems remain limited to delayed analysis or post-process correction, making true online feedback control difficult to achieve. Unlike offline or interlayer adjustments, in-process feedback control aims to dynamically stabilize melt pool behavior by instantaneously adjusting process parameters such as laser power and scanning speed based on sensor data.

Asadi et al. [77] proposed a Model Predictive Control (MPC) approach based on Gaussian

Process (GP) modelling, which learns the influence of laser power and scanning speed on the melt pool cross-sectional area to establish a constrained optimization model for real-time power regulation. Another study [78] designed a feedforward controller based on a Radial Basis Function Neural Network (RBF-NN), implemented on an FPGA to enable rapid adjustments of laser power and scanning speed. This approach reduced the standard deviation of the melt pool temperature field by 48%, demonstrating the feasibility of real-time control.

It is worth noting that due to the limitations of AM machines—such as the lack of open architecture for flexible in-situ process control modification—and restricted computational capability, online machine learning-assisted process control remains at a conceptual stage.

1.2.3 Post-Processing Stage — Performance Enhancement and Integrity Optimization

Despite parameter optimization, the complex phenomena occurring during melting and solidification in LPBF materials [79][80][81][82]—including rapid solidification, spattering, and balling [83][84][85]—result in high thermal gradients and nonuniform cooling effects, which inevitably lead to defects such as porosity, cracking, residual stress, and surface roughness in the fabricated parts. These defects not only degrade the mechanical performance of the components but also compromise their surface and structural integrity.

Therefore, post-processing techniques have become a critical step in ensuring the quality and service performance of LPBF-fabricated components. Their primary aims are to improve surface finish, eliminate internal defects, relieve residual stress, and optimize microstructural features, thereby enhancing the overall performance of the parts.

Currently, various post-processing methods are commonly applied to LPBF-fabricated components, including surface treatment[86], heat treatment [87], hot isostatic pressing (HIP) [88], and machining [89]. These techniques act on different levels of the component, improving properties from the external surface to the internal microstructure. For example, mechanical grinding, polishing, and shot peening can effectively reduce surface roughness and improve surface morphology; chemical etching or electrochemical polishing helps achieve smoother surfaces; heat treatments such as solution treatment, aging, or annealing can relieve residual stress and refine grain structures; and HIP processing can eliminate porosity, enhance densification, and improve mechanical performance while maintaining geometric accuracy. In some cases, machining operations such as milling, turning, or drilling are required to achieve strict dimensional tolerances or remove excess material from printed parts. Hybrid manufacturing methods that combine LPBF with subtractive machining enable the production of complex geometries with high precision. Through the application of these post-processing techniques, the quality, functionality, and performance of LPBF components can be significantly improved, making them suitable for a wide range of industrial applications.

In Study [90], to address technical challenges and quality issues, researchers systematically investigated the LPBF manufacturing process and post-processing techniques using 17-4PH stainless steel. The researchers explored post-processing methods such as mechanical polishing, physical vapor deposition (PVD) coating, and hot isostatic pressing (HIP) to improve surface quality and densification. By combining experimentally optimized LPBF process parameters with post-processing treatments, significant improvements in surface roughness, glossiness, and porosity were achieved, bringing the quality of LPBF products to or above commercial standards. Defects such as carbide formation were observed under specific laser power and scanning speed conditions, prompting researchers to adjust process parameters and apply HIP treatment to minimize defects and enhance density. Mechanical polishing and PVD coating further improved surface quality, thereby enhancing gloss and tactile smoothness, making LPBF products suitable for various engineering applications.

Heat treatment is a common post-processing technique in which components undergo heating and cooling cycles to achieve a uniform microstructure and improved physical and mechanical properties [91]. LPBF-316L samples subjected to heat treatment for 2 hours at temperatures between 600°C and 1095°C exhibited inferior mechanical properties—such as yield strength, ultimate tensile strength, and microhardness—compared with the as-built condition [91][92][93][133], as shown in Fig. 15. After heat treatment, the cellular substructure and melt pool boundaries in the LPBF-316L samples disappeared, and only grains were observed (Fig. 15a–b). Researchers [92][93][94] found that the grain size of samples heat-treated above approximately 1000°C increased relative to the as-built samples. The cellular substructure contributes to higher mechanical strength, and its disappearance results in a significant reduction in strength [93][95]. Kong et al. [92] further reported that heat-treated samples exhibited poorer corrosion resistance due to the increased density of oxide inclusions and thinning of the passive film.

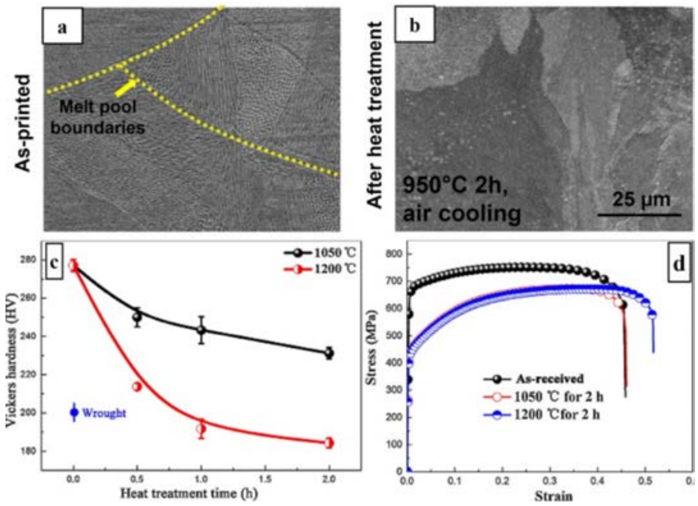

Fig. 15Microstructure and mechanical performance of LPBF-316L after heat treatments

In another study [96], the evolution of porosity in Ti-6Al-4V alloy parts during laser post-processing of LPBF was investigated, focusing on key defect issues such as porosity that affect part quality. The top surface was rescanned with a laser beam, and the internal morphology and porosity distribution were examined using micro-computed tomography (micro-CT). The results showed that after laser post-processing, the porosity significantly decreased from 2.51% to 0.77%. Furthermore, a multiphysics coupled finite element model employing a level-set method was developed to analyze the mechanisms of pore evolution, taking into account factors such as energy density, Marangoni flow, and mass transfer. The model elucidated the typical processes and provided insights into pore evolution under various post-processing parameters, contributing to a better understanding of how to mitigate porosity-related defects in LPBF manufacturing.

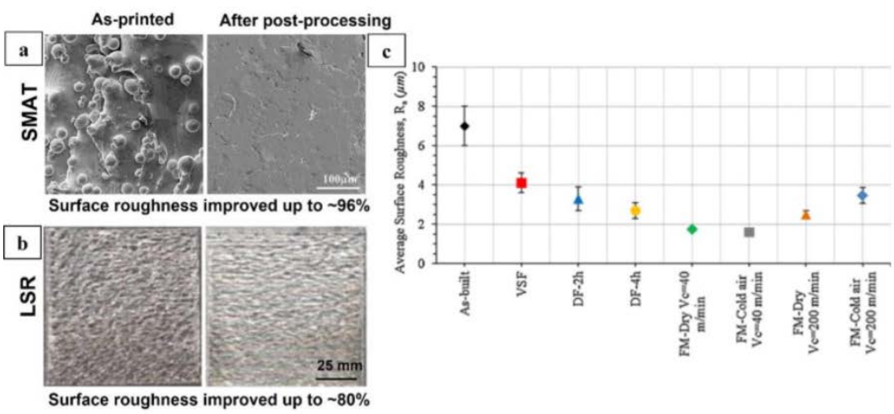

Fig. 16 Comparing surface roughness of LPBF-316L components in as-printed and after (a) SMAT (b) LSR (c) VSF, DF and FM post-processing condition[102] [105] [106].

Severe Plastic Deformation (SPD) is widely used in manufacturing to enhance corrosion resistance[97], mechanical [98], and tribological[99] properties. Shot peening, ultrasonic shot peening, and sandblasting are collectively referred to as Surface Mechanical Attrition Treatment (SMAT), which induces severe plastic deformation on the substrate surface, leading to surface nano crystallization [100][101]. For example, shot peening is an SPD process that involves bombarding the surface with hard spherical particles made of ceramic, glass, or metal at a specific velocity sufficient to induce high plastic deformation in the near-surface region. As a result, the physical and mechanical properties of the outermost surface layer are improved. Using SMAT [102], the surface roughness of LPBF-316L was improved by 96%, as shown in Fig. 16 The high-energy impact of hard particles produced a flattening effect on the surface, thereby enhancing surface quality. Researchers[102][103] reported that material properties such as compressive yield strength, wear resistance, and hardness were improved due to grain refinement and phase transformation. For 17-4 stainless steel, the martensitic transformation temperature is relatively low; therefore, during shot peening strengthening, austenite-to-martensite transformation occurs as a result of the higher work-hardening effect, which may explain the observed increase in hardness[104].

1.3 Existing Problems

In summary, significant progress has been made in recent years by researchers in the areas of modelling and prediction, process monitoring and control, and post-processing optimization of Laser Powder Bed Fusion (LPBF). However, despite substantial achievements in theory, algorithms, and experimental techniques, several key scientific challenges and technical bottlenecks remain to be addressed.

(1) High computational cost in LPBF modelling and insufficient physical interpretability of data-driven machine learning approaches.

Current LPBF modelling approaches can be categorized into 1.Theory-Based (TB) models and 2.Empirical-Based (EB) models. The former (e.g., FEM, CFD, and DEM–CFD coupled models) can accurately capture the complex interactions among the laser, material, and melt pool, but they require extensive computational resources, making real-time prediction and multiscale process optimization difficult to achieve. The latter (e.g., traditional machine learning and deep learning models) have achieved significant improvements in prediction efficiency by rapidly establishing mappings between process parameters and response variables; however, they generally suffer from the following issues:

•Strong dependence on large-scale, high-quality datasets, while experimental data acquisition in the LPBF process is costly;

•Limited generalization capability, making it difficult to adapt to complex conditions across different materials and machines;

•Lack of physical interpretability, which hinders the model's ability to reveal the underlying thermo-mechanical–microstructural evolution mechanisms.

Therefore, it is urgently necessary to develop machine learning models with low data dependence and embedded physical constraints. The Physics-Informed Neural Network (PINN), which integrates physical laws into the neural network loss function, provides a feasible approach to address these challenges. This type of model reduces reliance on experimental data while significantly enhancing the physical consistency, interpretability, and computational efficiency of predictions, thereby offering a new research direction for rapid modelling and optimization of the LPBF process.

(2) Complex data processing and limited real-time feedback control in process monitoring

Existing LPBF in-situ monitoring primarily relies on two types of sensing methods: (i) radiative sensors (e.g., infrared thermography) used to capture melt pool temperature fields, spatter, and plume signals; and (ii) non-radiative sensors (e.g., optical or acoustic sensors) used to obtain information on melt pool morphology, energy fluctuations, and abnormal events. However, these monitoring approaches are mostly designed for inter-layer, where imaging analysis of the processed layer is performed before adjusting the process parameters for the next layer. Their main limitations include:

- The data are massive and high-dimensional, requiring high bandwidth and powerful algorithmic support for real-time processing;
- The monitoring–analysis–feedback cycle is relatively long, making it difficult to achieve true online closed-loop control;
- Most existing systems remain limited to post-process analysis or delayed response stages

At present, research on real-time feedback control for LPBF remains relatively limited. Existing offline optimization approaches are mostly based on statistical or empirical methods and fail to fully account for dynamic disturbances and stochastic effects during the manufacturing process. Due to the closed architecture of additive manufacturing systems (i.e., the lack of open interface protocols) and limited hardware computational capability, online machine-learning-assisted control is still at the proof-of-concept stage. Therefore, it is imperative to develop a real-time adaptive system that integrates online monitoring with intelligent control to dynamically adjust process parameters, compensate for defects, and improve printing quality based on sensor data.

In this context, fast-solving models such as PINN can play a key role in online monitoring and real-time decision-making, providing efficient physical consistency prediction support for closed-loop control.

(3) Research on high-performance LPBF-processed materials (Scalmalloy) remains insufficient.

In recent years, with the increasing demand for lightweight and high-strength structural materials in aerospace and advanced manufacturing, Scalmalloy®, a high-strength, heat-treatable aluminum alloy, has demonstrated excellent mechanical and fatigue properties in Laser Powder Bed Fusion (LPBF) fabrication. However, systematic research on this material system is still in its early stage. In particular, studies on post-processing techniques and performance response mechanisms are relatively limited, and existing literature lacks comprehensive summaries and mechanistic interpretations.

1.4 Overall Framework and Workflow

To address the challenges in the Laser Powder Bed Fusion (LPBF) process—namely the high computational cost of modelling, lack of physical interpretability, delayed in-situ monitoring feedback, and the incomplete research framework for the high-performance aluminum alloy Scalmalloy®—this study establishes a multi-stage research framework that integrates process modelling, model calibration and validation, process optimization, and post-processing performance enhancement. The modelling stage is centered on the Physics-Informed Neural Network (PINN), achieving high-precision thermal conduction modelling, model calibration through inverse analysis. The objective of this research is to develop a PINN-based temperature field prediction model that combines physical consistency, computational efficiency, and engineering scalability by embedding physical laws into the neural network framework. The calibrated model is successfully applied to practical production scenarios, which shows the potential for real-time prediction and intelligent control of the LPBF process. Finally, in the post-processing stage, a systematic investigation is conducted on the effects of machining (M), shot peening (SP), and combined machining plus shot peening (M+SP) on the surface and structural integrity of LPBF-fabricated Scalmalloy®, thereby deepening the understanding of its structure–performance correlations.

Chapter 1: Introduction. This chapter reviews the current research on LPBF along three main lines and clarifies the motivation of this work:(1) Process modelling and prediction: Physics-based models (FEM, CFD, VOF) are accurate but computationally expensive and parameter-sensitive, while empirical and machine learning models are efficient but data-dependent and lack physical interpretability. Thus, fast and physics-constrained surrogate models such as PINNs are needed to bridge this gap; (2) In-situ monitoring and control: Thermal, optical, and acoustic sensing generate large data volumes that are difficult to process in real time, so most systems remain at interlayer or post-process analysis. Real-time closed-loop control requires fast and physically consistent predictors; (3) Post-processing and performance optimization: Techniques like heat treatment, machining, HIP, and surface strengthening (e.g., shot peening, SMAT) improve integrity and fatigue resistance, but systematic studies on Scalmalloy® alloys remain limited.

Chapter 2: Physics-Informed Thermal Modelling of LPBF Keyhole Mode. This chapter investigates the laser process under the keyhole mode of LPBF by introducing a double-conical volumetric heat source model and developing a Physics-Informed Neural Network (PINN) framework. By explicitly incorporating the heat conduction partial differential equations and boundary conditions into the neural network loss function, the model achieves high-accuracy temperature field prediction under limited data conditions. Through the optimization of network architecture and sampling strategy, combined with transfer learning to accelerate convergence, the model can reconstruct three-dimensional transient temperature distributions without relying on experimental data. This approach significantly improves the computational efficiency and physical consistency of LPBF thermal behavior simulations, laying a solid foundation for process optimization.

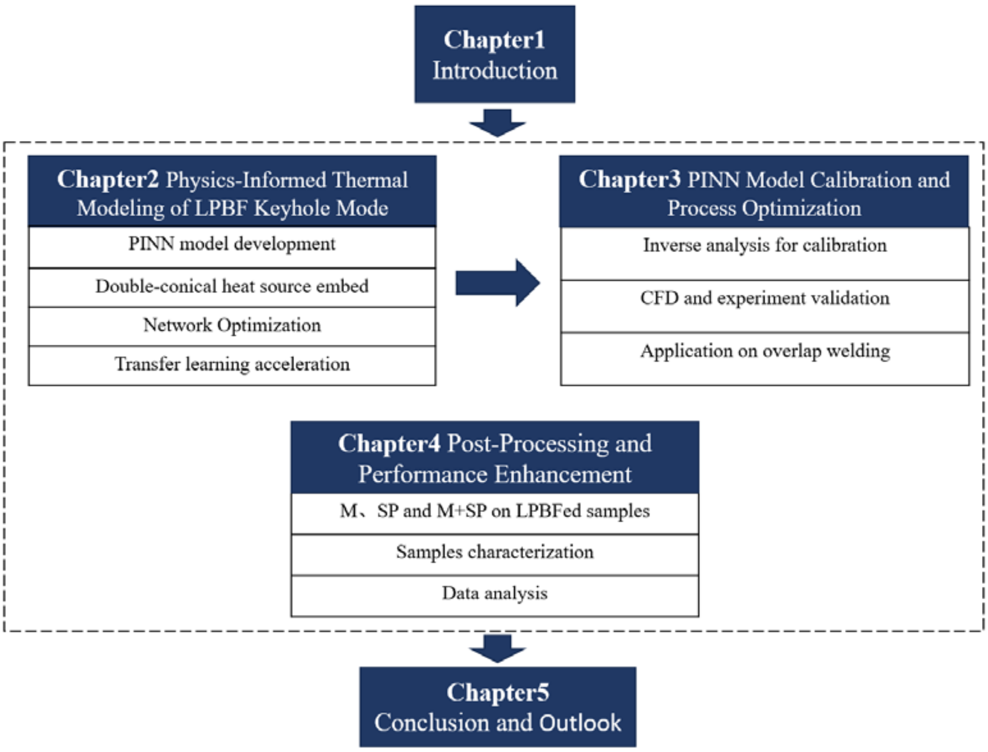

Fig. 17 Overall framework

Chapter 3: PINN Model Calibration and Application. Building upon the PINN framework developed in the previous chapter, this chapter further conducts model parameter calibration and inverse analysis. By minimizing the discrepancy between the PINN-predicted and experimentally measured results, an empirical mapping relationship between laser power, scanning speed, and the geometric parameters of the volumetric heat source is established, enabling the automatic calibration of the heat source model. After validation, the trained PINN is capable of predicting melt pool geometry and temperature distribution within milliseconds, with extremely low computational cost and no need for manual parameter tuning. Subsequently, a case study on the overlap welding of two 1.5 mm thick aluminum alloy plates is carried out. The PINN is employed to rapidly screen and optimize multiple combinations of laser parameters, and the accuracy of the predicted results is experimentally verified.

Chapter 4: Performance Enhancement and Structural Integrity Optimization. After achieving process modelling and optimization, this chapter further extends the research to the post-processing stage to improve the performance and integrity of LPBF-fabricated components. Focusing on the high-strength aluminum alloy Scalmalloy® (Al-Mg-Sc-Zr) produced by LPBF, a systematic investigation is conducted to evaluate the effects of different post-processing methods—machining (M), shot peening (SP), and combined machining plus shot peening (M+SP)—on the surface integrity and structural integrity of the components. Through comprehensive analyses of microstructure, hardness, tensile properties, fatigue life, and residual stress distribution, the relationships between post-processing parameters and material performance are revealed. This study provides theoretical and technical support for improving the service performance of LPBF-fabricated components.

Chapter 5: Conclusions and Outlook. This chapter summarizes the research content and key findings of the study, highlighting the main innovations achieved throughout the work. Furthermore, it presents perspectives on future research directions to advance the development of LPBF process modelling, intelligent control, and performance optimization.

Chapter 2 Physics-Informed Thermal Modelling of LPBF Keyhole Mode

2.1 Introduction

The Laser Powder Bed Fusion (LPBF) process is essentially a highly nonlinear and transient thermo–fluid–solid coupled system, in which multiple physical phenomena—such as energy absorption, phase transformation, melt pool convection, and vaporization—are intricately intertwined. The variation in melting modes directly influences the melt pool geometry, density, and microstructural properties, typically manifesting in three distinct regimes: conduction mode, transition mode, and keyhole mode. The transition among these modes is primarily governed by a combination of parameters, including laser power, scanning speed, and beam profile.

Among these modes, the keyhole mode—though prone to increased porosity—remains of great significance in the fabrication of thick-walled structures and large-scale components due to its higher energy coupling efficiency and deeper penetration capability. Its formation involves intense fluid disturbances and vaporization dynamics, which exert strong influences on heat transfer, pressure distribution, and melt pool stability. Consequently, accurate temperature field prediction and stability analysis under the keyhole mode are essential for understanding the underlying mechanisms of the LPBF process and achieving high-quality manufacturing.

However, traditional LPBF modelling approaches face multiple challenges. Numerical simulations (such as CFD, FEM, and VOF) can accurately capture the internal flow and phase transition behaviour within the melt pool, but they are computationally intensive and highly sensitive to parameters, making them unsuitable for real-time prediction and multi-parameter optimization. In contrast, purely data-driven machine learning models offer higher prediction efficiency but rely heavily on large, high-quality datasets and lack physical interpretability, making it difficult to maintain accuracy and stability across different materials, machines, and complex processing conditions.

To address the aforementioned challenges, this chapter focuses on the single-track melting process of LPBF under the keyhole mode and develops a Physics-Informed Neural Network (PINN)-based temperature field prediction model. By explicitly embedding the heat conduction equation and related physical constraints into the neural network loss function, the proposed approach enables high-accuracy reconstruction of the temperature distribution under limited data conditions. Compared with traditional methods, the PINN framework combines the advantages of data-driven learning and physical consistency, significantly enhancing the computational efficiency.

This chapter proposes a PINN model for the keyhole-mode LPBF process, which can predict the temperature field with significantly lower computational cost and faster speed compared to traditional numerical simulations. The model systematically optimizes the PINN architecture, activation functions, and collocation point sampling strategy. Network training requires no experimental data, relying solely on the governing partial differential equations and boundary conditions of the problem. For simplification, the powder layer on the single track surface is neglected, and only heat conduction is considered, while all multiphysics effects are ignored. To enable the model to automatically adapt to different LPBF melt mode, the heat source shape and size are defined by five parameters. Finally, a transfer learning strategy is employed to accelerate convergence and ensure efficient model training.

2.2 Thermal Conduction Mechanism and Modelling Fundamentals of the LPBF Process

2.2.1 Melting Modes and Thermal Behavior Characteristics of LPBF

The fundamental process dynamics of LPBF are highly complex and not yet fully understood. A key factor in describing these dynamics is the thermal behavior, which involves multiple physical mechanisms, including heat absorption, steep thermal gradients, localized melting and solidification of powder particles, phase transformations, and Marangoni convection[107]. These coupled phenomena are highly sensitive to process parameters such as laser power, scanning speed, and beam profile [108]. When the energy density exceeds a critical threshold, defects such as keyhole formation may occur [109][110][111]. Conversely, when the energy density falls below a certain limit, issues such as porosity, low-density regions, and insufficient interlayer bonding are likely to arise.

As shown in Fig. 18, the LPBF process can be divided into different regimes—namely the conduction, keyhole, and transition modes—depending on laser power, scanning speed, and other processing parameters. In the conduction mode, the laser power is relatively low and the scanning speed is relatively high. The laser energy is primarily conducted into the material, resulting in localized heating. This regime is characterized by a shallow melt pool and limited material vaporization, and it is typically employed for fine features, surface finishing, and low-energy input conditions. In the keyhole mode, the laser power is significantly higher and the scanning speed is usually lower. The intense laser energy forms a deep and narrow “keyhole” in the material, with the keyhole walls undergoing melting and vaporization. This mode features a deeper melt pool and higher vaporization rate, often used for producing larger and stronger components, though it can also lead to increased residual stress and porosity. The transition mode lies between the conduction and keyhole regimes, representing a combination of the two. In this intermediate region, laser parameters must be carefully adjusted to balance the advantages of both conduction and keyhole modes. The transition mode is typically adopted when a trade-off between fine detail and build speed is desired to optimize the overall component quality[112].

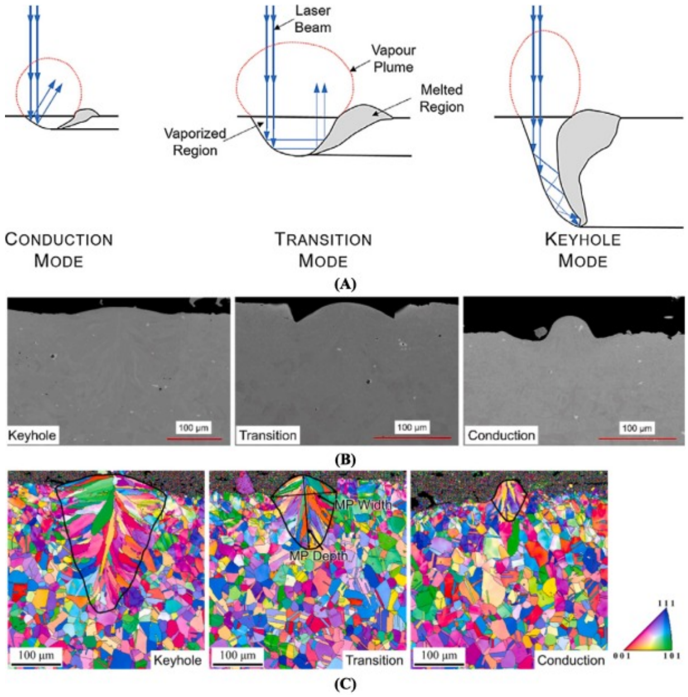

Fig. 18 The laser powder bed fusion different modes including keyhole, transitions, and conduction modes; A) Schematic, B) SEM, C) Inverse Pole [112].

It is noteworthy that during the LPBF process, the keyhole mode, characterized by higher energy density and vaporization rates, typically produces a deeper melt pool. This mode involves intense fluid disturbances and vapor-driven dynamics, resulting in highly nonlinear and unstable process behavior, which makes related machine learning–based modelling studies relatively scarce. Nevertheless, owing to its high energy coupling efficiency, concentrated thermal input, and greater penetration depth, the keyhole mode remains widely employed in the fabrication of larger and higher-strength components. Based on this, the present study focuses on the laser melting process under the keyhole mode and develops a Physics-Informed Neural Network (PINN)-based temperature field prediction model. This framework aims to achieve a balance between computational efficiency and physical accuracy while providing deep insights into the thermal conduction characteristics and melt pool evolution mechanisms of keyhole-mode LPBF, thereby offering theoretical support for process optimization and future real-time control.

2.2.2 Mathematical modelling of temperature fields in melting and solidification processes

In the context of melted and resolidified regions, the transient temperature fields can be mathematically described using the heat conduction equation - Fourier-Kirchhoff's partial differential equation in the form[113]

$$\rho c_p \frac{DT}{Dt} = \left[\frac{\partial}{\partial x}\left(\lambda_x \frac{\partial T}{\partial x}\right) + \frac{\partial}{\partial y}\left(\lambda_y \frac{\partial T}{\partial y}\right) + \frac{\partial}{\partial z}\left(\lambda_z \frac{\partial T}{\partial z}\right)\right] + q_v \;\; [\mathrm{W{\cdot}m^{-3}}] \tag{1}$$

This equation incorporates a term DT/Dt which denotes substantial derivative of temperature T [$°C$, K] with time t [s], material properties: density (ρ [kg. m^3]), specific heat (c [J. kg^{-1}. K^{-1}]), thermal conductivity tensor (λ [W. m^{-1}.K^{-1}]), and volumetric density of internal heat sources (q_v [W.m^{-3}]). This term, representing the heat generated in the unit material volume per unit time, can be used for modelling of a heat source in melting and solidification processes.

To solve the heat conduction equation (1) using the theory of partial differential equations, it is necessary to establish uniqueness conditions, which means that several crucial inputs must be provided:

Geometric Parameters - define the shape and dimensions of the body in which the temperature field is calculated. They are necessary to establish the spatial characteristics of the melting and solidification structures.

Material Properties - thermo-physical properties of material(s): density (ρ), specific heat (c), thermal conductivity (λ), and other relevant material characteristics. This refers to the material properties of all the base material(s) and possibly the filler material used in melting and solidification. When entering material properties for melting and solidification processes, it is necessary to take into account their dependence on temperature.

Initial Conditions - describe the initial temperature distribution at the beginning of a process in time t = 0 second, i.e. at the beginning of the melting and solidification process. They serve as the starting point for the mathematical analysis and influence how temperature evolves over time.

Boundary Conditions - describe the thermal behaviour at the boundaries or interfaces of a body (system) and specify how heat is exchanged with the surrounding environment. In melting and solidification processes, they specify the thermal interactions at the interfaces of the melting and solidification structures and their surroundings. They play a crucial role in determining how heat flows in and out of the melting and solidification region, affecting the melting and solidification process and the resulting temperature fields.

Mathematically, various kind of boundary conditions (BC) can be defined. The boundary condition of the 1st kind (Dirichlet BC) is given by the body surface temperature. The boundary condition of the 2nd kind (Neumann BC) specifies the conductive heat flux on outer body surface. This condition can be also used to define a surface heat source in melting and solidification processes. The boundary condition of the 3rd type (Fourier BC) represents the equality between conductive and convective heat flux on the outer body surface. This condition is determined by the ambient temperature and the heat transfer coefficient.

Generally, the boundary conditions can vary with temperature or over time. Combined boundary conditions frequently arise, particularly when heat exchange between a system and its surroundings is facilitated through both convection and radiation. This is also the case for components cooling in melting and solidification processes. The total (combined) heat transfer coefficient, denoted as h_C, is calculated as the sum of the convective heat transfer coefficient (h_K) and the reduced (or equivalent) radiation heat transfer coefficient (h_R)

$$h = h_C + h_R = h_C + \frac{\varepsilon\sigma_0\left(T_w^4 - T_f^4\right)}{T_w - T_f} \quad \left[\mathrm{W{\cdot}m^{-2}}\right] \tag{2}$$

where ε [-] is the emissivity and σ_0 [W. m^{-2}.K^{-4}] is the Stefan-Boltzmann constant, T_w and T_f are the surface and fluid (ambient) temperatures, respectively. The values of the convective heat transfer coefficient can be calculated using appropriate correlations for natural or forced convection.

The approach to defining loads in melting and solidification processes is based on the selection and specification of a suitable heat source model describing the heat input to the melting and solidification process. It is necessary to note that the choice of the heat source model depends on the specific melting and solidification process, materials, and melting and solidification parameters being used. This procedure is one of the most difficult parts in developing a simulation model of the melting and solidification processes. On the other hand, the accuracy of the applied heat source model is crucial for reliable simulations and predictions of the temperature and thermal behaviour of structures during melting and solidification processes.

2.2.3 Heat source models in modelling of laser processes

The history of heat source models in numerical simulations is closely connected to the development of numerical methods and computational tools for solving complex thermal and fluid dynamics problems. A brief overview of the development of heat source models in numerical simulations of laser processes involves a simple point heat source model, some surface heat source models and mainly different types of volumetric heat source models.

(1) Surface heat source models

In the case of surface models of the heat source, it is assumed that they act on a defined part of the surface area of the constructions. They are incorporated into the simulation model using the boundary condition of the second kind, i.e. through heat flux density q [W. m^{-2}]. In general, surface heat source models are not suitable for numerical simulation of high-energy laser processes, and especially not for laser process in the keyhole mode.

(2) Volumetric heat source models

Volumetric heat source models are best suited to describe the nature of a moving laser energy source and to accurately capture the development of the melt pool, including the complex multi-physical phenomena occurring during a melting and solidification process. The term q [W. m^{-3}] in Eq. 1 is used to define the volumetric density of internal heat sources. The following section provides a brief characterization of the most frequently used models of volumetric heat sources, ranging from the simplest to the most complex.

The Gaussian ellipsoidal volumetric heat source (Fig. 19) with Gaussian volumetric heat distribution is defined by three geometrical parameters - the ellipsoid half-axes a, b and c. The volumetric density of internal heat sources is described by a function [114][115]

$$q_v(x,y,z) = \Phi \cdot \frac{6\sqrt{3}}{abc\pi^{3/2}} \cdot e^{-\frac{3x^2}{a^2}} \cdot e^{-\frac{3y^2}{b^2}} \cdot e^{-\frac{3z^2}{c^2}} \qquad [\mathrm{W{\cdot}m^{-3}}] \tag{3}$$

where V = $abc\,\pi^{3/2}/(6\sqrt{3}\,)$ is the volume of one half of the ellipsoid and the distribution function takes the form

$$f(x,y,z) = e^{-\frac{3x^2}{a^2}} \cdot e^{-\frac{3y^2}{b^2}} \cdot e^{-\frac{3z^2}{c^2}} \qquad [-] \tag{4}$$

Application of the constant volumetric density of heat sources or Gaussian heat source to the volume with the shape of a truncated cone or pyramid represents the modifications of presented model more suitable for modelling of laser or electron beam melting and solidification processes.

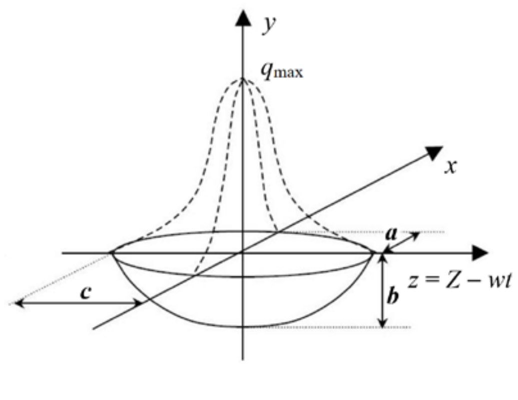

Fig. 19 Gaussian ellipsoidal volumetric heat source with Gaussian heat distribution for modelling of volumetric internal heat sources to the volume of half-ellipsoid[116].

The Goldak model or so called double ellipsoid heat source (Fig. 20) describes the distribution of volumetric density of heat sources to a volume with the form of a double ellipsoid[117]. The double ellipsoid is characterized by six parameters: the half axes b and c represent the width and depth of the heat source, half axes c1 and c2 in the frontal and rear quadrants define its length, and parameters f1 and f2 designate the portion of the heat generated in the frontal and rear parts of the double ellipsoid.

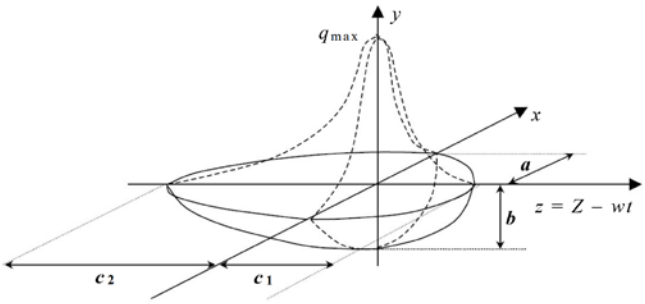

Fig. 20 Goldak model for modelling of volumetric internal heat sources to the volume of double ellipsoid.

Volumetric density of heat sources in front and rear quadrants can be expressed as[117]

$$q_{v1}(x,y,z,t) = \frac{6\sqrt{3}f_1\Phi}{abc_1\pi^{3/2}} e^{-\frac{3x^2}{a^2}} e^{-\frac{3y^2}{b^2}} e^{-\frac{3(z+wt)^2}{c_1^2}} \qquad [\mathrm{W \cdot m^{-3}}] \tag{5}$$

$$q_{v2}(x,y,z,t) = \frac{6\sqrt{3}f_2\Phi}{abc_2\pi^{3/2}} e^{-\frac{3x^2}{a^2}} e^{-\frac{3y^2}{b^2}} e^{-\frac{3(z+wt)^2}{c_1^2}} \qquad [\mathrm{W \cdot m^{-3}}] \tag{6}$$

$$f_1 = \frac{2c_1}{c_1 + c_2}, \qquad f_2 = \frac{2c_2}{c_1 + c_2}, \qquad f_1 + f_2 = 2 \qquad [-] \tag{7}$$

Figure 6 illustrates the definition of the heat input into finite element model using different parameters of the Goldak model.

The Goldak model can be used for numerical simulation of laser processes, but it is more suitable simulations of arc welding processes. Generally, it is currently considered to be the most accurate but also the most demanding method for defining heat input to the weld in arc welding processes [118][119].

It should be noted that the dimensions of the heat source are generally not known, and there is no direct link between laser process parameters and the dimensions of the heat source[117]. In most cases, the dimensions of the heat source are initially estimated for the simulation of a specific laser process and are subsequently modified and adjusted based on experimental results[119][120][121][122][123]. A portion of the heat supplied to both the front and back ellipsoids is determined by constants, f1 and f2. These constants influence the energy distribution into the material, compensating for factors such as the inclination of the welding torch. A heat distribution ratio of 60:40 in favour of the front ellipsoid is mostly used[124][125].

hybrid volumetric heat sources are composed of two or more different heat sources to better describe the complex physics behind different types of laser processes and to adjust the parameters of the resulting model so that the obtained results correspond to the real measured shape of the melt pool or melt pool macrographs.

In numerical simulation of laser processes, the double-conical volumetric heat source model (Fig.14) is the most frequently employed hybrid heat source model. The distribution of internal heat sources in the case of the double-conical volumetric heat source model is described by the following equations[126].

$$q_{v1}(x,y,z) = \frac{9\eta P e^3}{\pi(e^3-1)(z_i - z_b)\left(r_i^2 + r_i r_b + r_i^2\right)} \exp\left(-\frac{3[(x-vt)^2 + y^2]}{r_1^2}\right) \qquad (8)$$

$$q_{v2}(x,y,z) = \frac{9\eta P e^3}{\pi(e^3-1)(z_t - z_i)\left(r_t^2 + r_t r_i + r_i^2\right)} \exp\left(-\frac{3[(x-vt)^2 + y^2]}{r_2^2}\right) \qquad (9)$$

The corresponding radial profiles r_1 and r_2, which vary linearly along the height of each cone, are defined as:

$$r_1 = r_i - (r_i - r_b)\frac{z_i - z}{z_i - z_b} \qquad (10)$$

$$r_2 = r_t - (r_t - r_i)\frac{z_t - z}{z_t - z_i} \qquad (11)$$

The parameters used have a similar meaning to those in the simple conical model and can be identified from Fig. 21a. Fig. 21b illustrates some simple modifications of double-conical heat source with reverse and direct cone configurations.

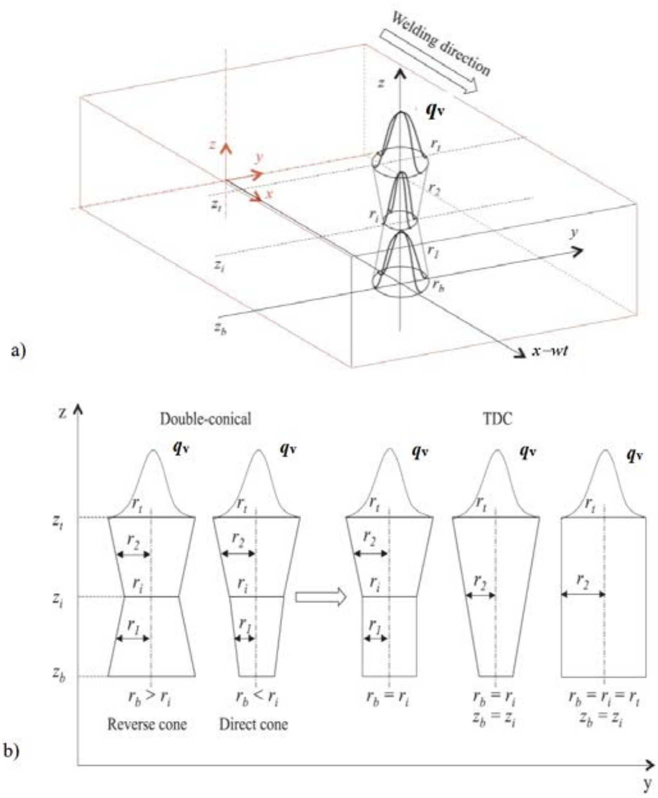

Fig. 21. Double-conical volumetric heat source model a) a scheme of the model with reverse cone configuration and b) simple modifications of double-conical heat source with reverse and direct cone configurations[127].

Compared with traditional Gaussian or double-ellipsoidal heat source models, the double-conical heat source model demonstrates higher accuracy and stronger physical consistency in capturing the energy deposition characteristics within the deep penetration zone under keyhole-mode LPBF. Notably, this model can also be extended to describe the conduction mode of laser processing while maintaining controllable geometric parameters—such as the heights and radius ratios of the upper and lower cones—showcasing excellent process adaptability and cross-mode scalability. Owing to its superior physical adaptability, geometric tunability, and application versatility, the double-conical heat source model is adopted in this study as the physical constraint foundation for PINN training, enabling high-accuracy modelling and prediction of the temperature field distribution during the laser melting process.

2.2.4 Physical-Informed Learning

Physics–informed learning can serve a variety of purposes, with the flexibility to adapt the same method to different use cases by making minor adjustments to the list of trainable variables and the terms comprising the loss function. For instance, these methods can be applied to solve PDEs (forward solutions), estimate parameters, address inverse problems, fit experimental measurements, or enhance the resolution in case of noisy data. In this discussion, we will begin by examining the simplest case (solving PDEs) and then extend the approach to other applications. To illustrate this general framework, we consider a simple PDE as an example.

FEM approximation of a PDE. Let $\Omega \subset \mathbb{R}^d$, with d = 2, 3, be an open bounded domain, with Lipschitz boundary. Given f: $\Omega \to \mathbb{R}$ and $g: \partial\Omega \to \mathbb{R}$ regular enough and a real coefficient $\gamma > 0$, we look for the solution u : $\Omega \to \mathbb{R}$ of the second–order elliptic equation with Neumann boundary conditions

$$\begin{cases} -\Delta u + \gamma u = f & \text{in } \Omega \\ \nabla u \cdot \boldsymbol{n} = g & \text{on } \partial\Omega \end{cases} \tag{12}$$

After introducing the Sobolev space $H^1(\Omega) = \{v : \Omega \to \mathbb{R} s.t. \int_\Omega v^2 + |\nabla v|2 < +\infty\}$, its weak form reads

$$\text{find } u \in V: \int_\Omega (\nabla u \cdot \nabla v + \gamma uv)\, d\Omega = \int_\Omega f\, v\, d\Omega + \int_{\partial\Omega} g\, v\, d\partial\Omega \quad \forall v \in V \tag{13}$$

or, equivalently,

$$\text{find } u \in V:\ a(u, v) = F(v) \qquad \forall v \in V, \tag{14}$$

where $a: V \times V \to \mathbb{R}$ defined by $a(u, v) = \int_\Omega (\nabla u \cdot \nabla v + \gamma uv) \mathrm{d}\Omega$ is a coercive, symmetric, and continuous bilinear form, and $F: V \to \mathbb{R}$ defined by $F(v) = \int_\Omega f v \mathrm{d}\Omega + \int_{\partial\Omega} gv\, d\partial\Omega$ is a linear and continuous functional. If $f \in L^2(\Omega)$ and $g \in L^2(\partial\Omega)$, this problem admits a unique solution[128].

Classical methods to discretize problem (14) are the Galerkin methods[128], for which, after introducing a discretization parameter $h > 0$ and the finite–dimensional space $V_h \subset V$, with $N_h = dim(V_h)$, we look for $u_h \in V_h$ such that:

$$a(u_h, v_h) = F(v_h) \quad \forall v_h \in V_h. \tag{15}$$

The Galerkin solution uh is an approximation of u.

The space V_h is the test space (i.e. the space to which the test functions v_h belong) and the trial space (i.e. the space to which the solution u_h belongs) at the same time. After choosing a basis of functions $\{\varphi_j(\mathbf{x})\}_{j=1}^{Nh}$ in V_h, the approximate solution uh can be written as $u_h(\mathbf{x}) = \sum_{j=1}^{Nh} u_j\, \varphi_j\, (\mathbf{x})$ and (35) becomes

$$\text{find } u_1, \dots, u_{N_h}: \sum_{j=1}^{N_h} u_j \; a(\varphi_j, \varphi_i) = F(\varphi_i) \qquad \forall j = 1, \dots, N_h. \tag{16}$$

Thus, by setting $A_{ij} = a(\varphi_j, \varphi_i)$, $b_i = F(\varphi_i)$, we have $A = [a_{ij}] \in R^{N_h \times N_h}$, $u = [u_j] \in \mathbb{R}^{N_h \times 1}$, and $b = [b_i] \in \mathbb{R}^{N_h \times 1}$ and the algebraic formulation of (82) reads $Au = \boldsymbol{b}$. The unknowns u_j are named degrees of freedom, while the array b is the right–hand side.

Finite Elements are a special case of Galerkin methods. Given the parameter $h > 0$, a mesh (A mesh is a conforming partition of Ω in triangles/quadrilaterals when $d = 2$, or in tetrahedra/hexahedra when $d = 3$, all with diameter less than h (the *mesh–size*), see Fig. 22, left.) $\mathcal{T}_{\hbar}$ on Ω is built. When simplexes are chosen and V_h is defined by

$$V_h = \{v_h \in C^0(\overline{\Omega}) \; s.t. \; v|T_k \in \mathbb{P}_1 \; \forall T_k \in \mathcal{T}_{\hbar}\} \tag{17}$$

we are implementing linear $\mathbb{P}_1$−FEM, and the basis functions φ_j, are hat functions like that drawn in the central picture of Fig. 22. The functions of V_h are linear combinations of hat functions, the one in the right picture of Fig. 22 is an example.

Towards NNs. We notice that the trial space V_h of Galerkin methods and the space V_{NN} of feedforward neural networks (FFNN) with a fixed architecture play a similar role: V_h is the space in which we look for the FEM solution, V_{NN} is the space in which we look for the solution provided by FFNNs. Moreover, we can think that the trainable parameters **w** which characterize a FFNN are analogous to the unknown degrees of freedom $\boldsymbol{u}$ that identify the FEM solution (see Table 1)

Thus, we could think of using the space V_{NN} as the trial solution space for PDEs. This could be explained as follows. First of all, FFNNs are very efficient in approximating functions. Second, one of the most expensive parts of a Finite Elements code is the construction of the mesh, while FFNNs are mesh–free. Nevertheless, although the PDE is linear, FFNNs are not linear models and this brings complications: V_{NN} is not a linear space and it is not a good candidate to be the test space for a Galerkin formulation.

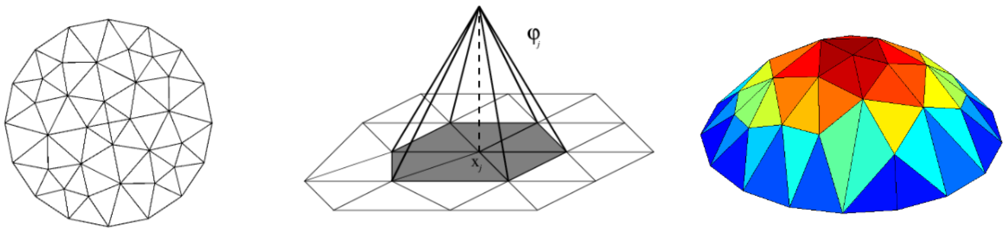

Fig. 22.A computational mesh made of triangles (left), a $\mathbb{P}_1$–FEM hat function (centre), a function of V_h (right)

space	solution	input	unknown parameters
V_h	$u(\mathbf{x}) = \sum_{j=1}^{N_h} u_j \varphi_j(\mathbf{x})$	$\mathbf{x}$	$\mathbf{u} = [u_1, \ldots, u_{N_h}]^t \in \mathbb{R}^{N_h}$
V_{NN}	$u_{NN}(\mathbf{x}; \mathbf{w})$	$\mathbf{x}$	$\mathbf{w} \in \mathbb{R}^N$

Table 1 Analogy between FEM and FFNNs

Recently, many approaches have been proposed that follow alternative paradigms to the Galerkin one, we cite the three most widespread ones. The first one consists of working on the strong form of the PDE and leads to Physics–Informed Neural Networks (PINNs)[129][130][131][132]. However, when the coefficients of the PDE are discontinuous and/or pointwise loads are given, solutions in a strong sense of PDE do not always exist. A possible alternative consists of considering the weak form of the PDE and applying a Petrov–Galerkin approach (with different trial and test spaces) leading to Variational PINNs (VPINNs)[33][34]. A third alternative makes use of the energy form of the PDE and provides the Deep Ritz method[35]. We refer to [132] for an overview of further extensions of PINNs.

2.2.4.1 Physics–Informed Neural Networks (PINNs)

PINNs allow us to reconstruct physical fields modelled by PDEs, by integrating the information from the PDE (learning biases) into the loss function. In principle, many types of PDEs can be approximated by PINNs: integer–order PDEs, integro–differential equations, fractional PDEs, and stochastic PDEs. PINNs can be used as direct solvers of PDEs, especially to address the case when we miss data (e.g., boundary or initial conditions, forcing terms, operator coefficients) which would be essential to approximate the problem in a classical sense. In addition, they can be even used to solve inverse problems.

PINNs as PDE solvers. We start by examining the case where PINNs are used to solve a PDE. Let us consider, as an example, the PDE (12) in strong form, PINNs are implemented by following these steps [132]:

1. define the residuals of the differential equation (12)-1 and of the boundary condition (12)-2:

$$\begin{aligned} Res^{PDE}\,[u(\boldsymbol{x})] &= -\Delta u(\boldsymbol{x}) + \gamma u(\boldsymbol{x}) - f(\boldsymbol{x}) \quad && \boldsymbol{x} \in \Omega \\ Res^{BC}[u(x)] &= \nabla u(x) \cdot n - g(x) && x \in \partial\Omega, \end{aligned} \tag{18}$$

2. choose a set of collocation points $\mathbf{x}_i^{PDE} \in \Omega$ (the blue ones in the left picture of Fig. 23 and another set of points $\mathbf{x}_i^{BC} \in \partial\Omega$ (the red ones), set $\{x_i\} = \{\mathbf{x}_i^{PDE}\} \cup \{\mathbf{x}_i^{BC}\}$, and provide the value ui of the solution at the collocation node $\boldsymbol{x}_i$ for any $i = 1, \ldots, N$, computed, for instance, by FEM.

3. design the FFNN like, e.g., in the right picture of Fig. 23,

4. train the NN: given the pairs $(\boldsymbol{x}_i, u_i)$ for $i = 1, \ldots, N$, look for the minimizer

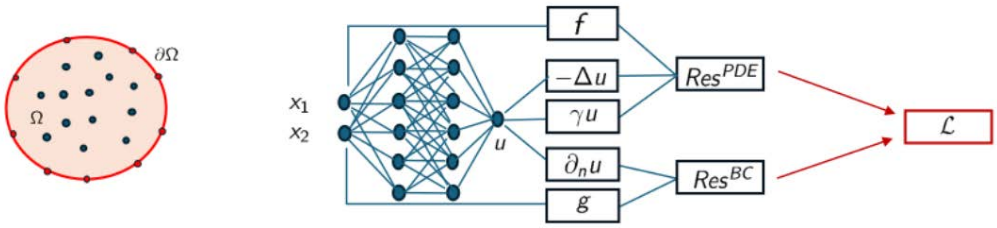

Fig. 23 The collocation nodes (left) and the PINN (right). We follow the branch Res^{PDE} if the input xi belongs to the interior of the domain and the branch Res^{BC} if xi is on the boundary

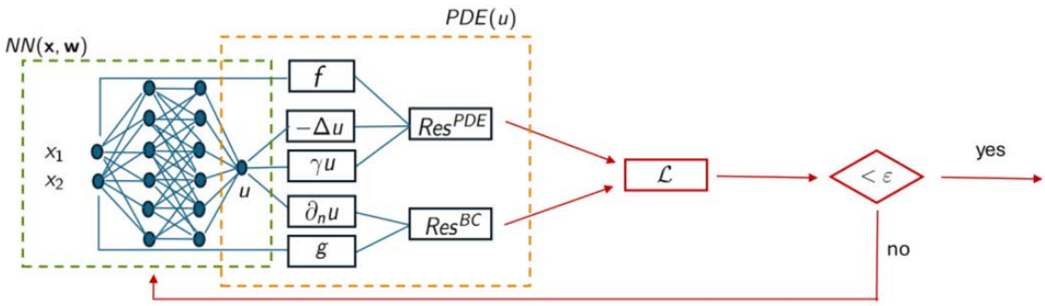

Fig. 24 The minimization process in PINNs

where the loss function is

$$\mathcal{L}(\mathbf{w}) = \mathcal{L}_{PDE}(\mathbf{w}) + \alpha_{BC} \cdot \mathcal{L}_{BC}(\mathbf{w}) \tag{19}$$

With

$$\mathcal{L}_{PDE}(\boldsymbol{w}) = \frac{1}{2N_{PDE}} \sum_{i=1}^{N_{PDE}} \left(Res^{PDE}\left[u_{NN}\left(\boldsymbol{x}_i^{\boldsymbol{PDE}}; \boldsymbol{w}\right)\right]\right)^2 \tag{20}$$

$$\mathcal{L}_{BC}(\boldsymbol{w}) = \frac{1}{2N_{BC}} \sum_{i=1}^{N_{BC}} \left(Res^{BC} \left[u_{NN} \left(\boldsymbol{x}_{\boldsymbol{i}}^{\boldsymbol{BC}}; \boldsymbol{w} \right) \right] \right)^2 \tag{21}$$

And $\alpha_{BC} \in \mathbb{R}$ is a suitable hyper–parameter.

5. take $u_{NN}(x; w^*)$ as the PINN solution.

In Fig. 24, the iterative process to minimize the loss function is drawn.

Provided that the activation function is regular (notice that, if $\sigma \in \mathcal{C}^{\infty}(\mathbb{R})$, then $u_{NN} \in \mathcal{C}^{\infty}$ on the input space $\mathcal{X} \in \mathbb{R}$), partial derivatives in the residuals are evaluated through automatic differentiation. Then, the loss function can be minimized via gradient–based methods.

The summations in (20) and (21) can be interpreted as approximations of integrals, i.e.

$$\underbrace{\frac{1}{N} \sum_{i=1}^{N} (Res[u_{NN}(\boldsymbol{x}_{\boldsymbol{i}}; \boldsymbol{w})])^2}_{I_N} \simeq \underbrace{\int_{\Omega} (Res[u_{NN}(\boldsymbol{x}; \boldsymbol{w})])^2 d\Omega.}_{I_{ex}} \tag{22}$$

If the nodes are randomly chosen, this corresponds to using the Monte Carlo quadrature rule, which provides an error $|I_{ex} - I_N| \approx N^{-1/2}$. Alternatively, if we choose the nodes more carefully and replace the arithmetic average with a weighted sum $I_{ex} \approx I_{N,\omega} = \sum_{i=1}^{N} \omega_i (Res[u_{NN}(x_i; w)])^2$ [133] , we might obtain higher accuracy $\left|I_{ex} - I_{N,\omega}\right| \leq CN^{-s}$ with $s \geq 1$ depending on the regularity of both data and solution and possibly on the space dimension.

One of the main strengths of PINNs is their mesh–free nature. This makes them particularly appealing because they bypass the often lengthy and tedious process of mesh generation. Indeed, PINNs can be effectively applied to irregular and complex domains [134][135]. Additionally, the availability of many open–source machine learning platforms, which are highly optimized for modern hardware, has made the implementation of PINNs very straightforward. Full utilization of the computational power offered by GPUs allows for realising very efficient PINN architectures. Automatic differentiation makes PINNs easily applicable to non–linear PDEs. More precisely, while solving a non–linear PDE with FEM requires modifying heavily the code designed for linear problems (we have to compute the residual of the PDE and apply Newton–like methods), PINNs are straightforward to implement and only those lines of the code performing the calculation of the residual have to be changed.

On the other hand, computing the optimal parameters $\mathbf{w}*$ involves solving an optimization problem, making the computational cost of PINNs typically higher than that of FEMs, even for linear PDEs. Thus, traditional numerical methods usually outperform PINNs in solving well–

posed forward problems. However, in cases involving PDEs in high–dimensional spaces, where mesh construction becomes challenging and is affected by the curse of dimensionality, PINNs offer a compelling alternative. This is due to the neural networks' ability to efficiently approximate functions in high–dimensional spaces.

A critical aspect of PINNs is that, when the solution of the PDE contains high–frequencies or multiscale features, PINNs using fully connected architectures struggle to converge during the training[136]. This is a consequence of the so–called spectral bias, a phenomenon where neural networks tend to represent low–frequency components more effectively than high–frequency ones[136] [248]. This limitation poses challenges in accurately solving problems with solutions characterized by high–frequency components, such as wave–like behaviours or sharp discontinuities. To address this issue, several solutions have been proposed in the literature. These include using periodic activation functions, such as Fourier Features [137], which enhance the network's ability to capture high frequencies, and adaptive or weighted loss functions [138], which balance the representation across different spectral scales. These approaches have shown promise in mitigating the effects of spectral bias, thereby improving the capability of PINNs to solve complex problems.

Since PINNs represent a method that has spread to the scientific community relatively recently, its theoretical understanding is less mature than for other methods, although much progress has been made recently. Some aspects remain to be clarified, and in practical contexts very often empirical tests are needed to find the best configuration. In the following section, we discuss some of the theoretical results that pose a mathematically sound basis for using PINNs.

A posteriori error bound. Approximation properties of PINNs have been studied in[139][140][141][142]. We report here the results proved in [140][142] about the generalization error for feed–forward PINNs.

Let us consider a regular domain $\Omega \in \mathbb{R}$, a Banach space V (for second–order elliptic PDEs, a typical choice is $H^2(\Omega)$), a boundary operator$\mathcal{B}: V \rightarrow L^2(\partial\Omega)$, $f \in L^2(\Omega)$, $g \in L^2(\partial\Omega)$, and the problem of finding $u \in V$ solution of

$$\begin{cases} \mathcal{D}(u) = f & \text{in } \Omega \\ \mathcal{B}(u) = g & \text{on } \partial\Omega \end{cases} \tag{23}$$

Let us assume that (88) admits a unique solution. We define the loss function

$$\mathcal{L}(\mathbf{w}) = \mathcal{L}_{PDE}(\mathbf{w}) + \alpha_{BC} \cdot \mathcal{L}_{BC}(\mathbf{w}) \tag{24}$$

where $\alpha_{BC} \in \mathbb{R}$ is a suitable weight, while LP DE and LBC are defined by

$$\mathcal{L}_{PDE}(\boldsymbol{w}) = \frac{1}{2}\sum_{i=1}^{N_{PDE}} \omega_i^{PDE} \left|\mathcal{D}\left(u_{NN}(\boldsymbol{x_i^{PDE}}; \boldsymbol{w})\right) - f(\boldsymbol{x_i^{PDE}})\right|^2 \tag{25}$$

$$\mathcal{L}_{BC}(\boldsymbol{w}) = \frac{1}{2}\sum_{i=1}^{N_{BC}} \omega_i^{BC} \left|\mathcal{B}\left(u_{NN}(\boldsymbol{x_i^{BC}}; \boldsymbol{w})\right) - g(\boldsymbol{x_i^{BC}})\right|^2 \tag{26}$$

with ω_i^{PDE} and ω_i^{BC} suitable quadrature weights. In the case of the Monte Carlo formula, we have $\omega_i^{PDE} = 1/N_{PDE}$, $\omega_i^{BC} = 1/N_{BC}$. We assume that, when increasing the number of collocation nodes, we keep constant the ratio between the number of nodes in the interior and on the boundary, so that we can define a single parameter N such that $N_{PDE} \approx N$ and $N_{BC} \approx N$.

Then, we train the network by looking for $\mathbf{w}*$ solution of

$$w^* = \arg\min_{w\in\mathbb{R}^M} \mathcal{L}(w),$$

and define $u^* = u_{NN}(; w^*)$ as the PINN solution. The following theorem is from [140][142]:

Theorem 1. *Provided that the following stability assumption*

$$\|v_1 - v_2\| \le C_{PDE}(\|v_1\|_V, \|v_2\|_V) \cdot \begin{bmatrix} \|\mathcal{D}(v_1) - \mathcal{D}(v_2)\|^2_{L^2(\Omega)} \\ +\alpha_{BC}\|\mathcal{B}(v_1) - \mathcal{B}(v_2)\|^2_{L^2(\Omega)} \end{bmatrix}^{1/2}$$

holds for any v_1, v_2 belonging to a closed subspace of V, then there exist two positive constants c_1 and c_2 such that

$$\|u^* - u\|_V \le c_1\mathcal{L}(\boldsymbol{w}^*)^{1/2} + c_2 N^{-s/2}, \tag{27}$$

where s is the accuracy order of the quadrature formula.

The term $\|u^* - u\|_V$ represents the generalization error, $\mathcal{L}(\boldsymbol{w}^*)^{1/2}$ is the training error, while $c_2N^{-s/2}$ bounds the quadrature error. The constant c1 depends on the exact solution, the NN solution and the PINN architecture (i.e., the number of layers, neurons and training collocation points), while c2 depends on the exact solution and the quadrature formula. The error estimate (27) establishes that minimizing the residual of the PDE (including the residual of boundary conditions) leads to the control of the generalization error, provided that a sufficient number of collocation nodes is employed. We refer to [140][142] for a more in–depth analysis of this topic.

PINNs for inverse problems. As anticipated, the scope of PINNs is not limited to the solution of PDEs. They can be effectively employed in a variety of scenarios, including the solution of inverse problems. In the following, we illustrate how PINNs can be used to address the identification of parameters of a PDE, starting from some suitable measures on the solution.

Let us consider the problem (78), we know the functions f and g and want to estimate the parameter $\gamma \in \mathbb{R}$ starting from N_{obs} observations $u_i^{\text{obs}} = u(\boldsymbol{x}_i^{obs})$, with $i = 1, \dots, N_{\text{obs}}$. This is an instance of inverse problem and, in particular, a parameter identification problem.

$$\begin{aligned} &\min_{\gamma>0,\, u_h \in V_h} \sum_{i=1}^{N_{\text{obs}}} \left|u_i^{\text{obs}} - u_h(\boldsymbol{x}_i^{obs})\right|^2 \\ &s.t.\ \int_\Omega \nabla u_h \cdot \nabla v_h + \int_\Omega \gamma u_h v_h = \int_\Omega f\, v_h + \int_{\partial\Omega} g\, v_h \quad \forall v_h \in V_h, \end{aligned} \tag{28}$$

for a convenient finite dimensional subspace V_h of the Sobolev space $H^1(\Omega)$. Then, we could invoke standard algorithms for constrained optimization (like, e.g., those based on the "trust region" or the "interior point" methods [143] or resort to the optimal control theory[144] and solve the related optimality system. In the latter case, if we adopted an iterative solver to solve the optimality system, at each iteration we should solve two FEM problems: one primal (i.e. problem (27)2) and one adjoint of (27)2, see[144][145].

Instead, the PINN approach consists of defining the loss function

$$\mathcal{L}(\boldsymbol{w}, \gamma) = \mathcal{L}_{obs}(\boldsymbol{w}) + \alpha_{PDE}\mathcal{L}_{PDE}(\boldsymbol{w}, \gamma) + \alpha_{BC}\mathcal{L}_{BC}(\boldsymbol{w}) \tag{29}$$

With

$$\mathcal{L}_{obs}(\boldsymbol{w}) = \frac{1}{N_{\text{obs}}} \sum_{i=1}^{N_{obs}} \left|u_i^{\text{obs}} - u_{NN}(\boldsymbol{x}_i^{obs}; \mathbf{w})\right|^2$$

$$\mathcal{L}_{PDE}(\boldsymbol{w}, \gamma) = \frac{1}{2} \sum_{i=1}^{N_{PDE}} \omega_i^{PDE} \left|\mathcal{D}\left(u_{NN}\left(\boldsymbol{x}_i^{PDE}; \boldsymbol{w}\right); \gamma\right) - f\left(\boldsymbol{x}_i^{PDE}\right)\right|^2$$

and $\mathcal{L}_{BC}(\boldsymbol{w})$ as in (26), and computing

$$w^*, \gamma^* = \underset{\boldsymbol{w} \in \mathbb{R}^M,\, \gamma \in \mathbb{R}^+}{\operatorname{argmin}} \mathcal{L}(w, \gamma)$$

The advantages of PINNs compared with the classical approach are that only a minimal modification with respect to the direct problem is required (we have added a new parameter to the array $\mathbf{w}$ of the NN parameters and the term $\mathcal{L}_{obs}$ to the loss function.). Moreover, PINNs also work in case of defective data, for instance, when some of the boundary conditions are missing. The flexibility of PINNs in seamlessly addressing different types of problems is a key feature that makes them particularly appealing in the context of inverse problems.

In general terms, the problem of parameter estimation with PINNs can be framed as follows:

$$\boldsymbol{w}^*, \gamma^* = \underset{\boldsymbol{w}\in\mathbb{R}^M, \gamma\in\mathbb{R}^P}{\operatorname{argmin}} \left[\frac{1}{N_{\text{obs}}} \sum_{i=1}^{N_{\text{obs}}} \left| u_i^{\text{obs}} - u_{NN}(\boldsymbol{x}_i^{obs}; \mathbf{w}) \right|^2 + \mathcal{L}_{phys}(u_{NN}(\cdot; \boldsymbol{w}), \gamma) \right] \tag{30}$$

where the physics–based regularization term is defined as

$$\begin{aligned} \mathcal{L}_{phys}(u, \gamma) = \frac{\alpha_{PDE}}{2N_{PDE}} \sum_{i=1}^{N_{PDE}} \left(Res^{PDE}\left[u\left(\boldsymbol{x}_i^{PDE} \right); \gamma \right] \right)^2 \\ + \frac{\alpha_{BC}}{2N_{BC}} \sum_{i=1}^{N_{BC}} \left(\text{Res}^{BC}\left[u\left(\boldsymbol{x}_i^{BC} \right); \gamma \right] \right)^2 \end{aligned} \tag{31}$$

Multifidelity PINNs. Inverse problems are often ill–posed due to data scarcity. Sometimes a surplus of boundary conditions is given on a small subset Γ of the boundary $\partial\Omega$, while no information is available on $\partial\Omega \backslash \Gamma$. Other times, boundary data are completely missing, while only measurements inside the domain are available. Consequently, multiple local minima and challenging optimization landscapes occur. In these circumstances, despite the physics–informed regularization, achieving convergence and stability remains difficult. To address this issue, a multi–fidelity approach can be introduced[145], leveraging a combination of low– and high–fidelity models. The purpose is to enhance convergence of the optimization process and improve robustness with respect to noise. Two different datasets are typically used. The first one $(\boldsymbol{x}_i^{obs,} u_i^{obs})$ with $i = 1, \dots, N_{\text{obs}}$, feeds the high–fidelity model. The second one, $(\boldsymbol{x}_i^{low,} u_i^{low})$, for $i = 1, \dots, N_{\text{low}}$, feeds the low–fidelity model and is typically characterized by a larger number of data but lower fidelity, such as those collected from numerous low–quality sensors.

Typically, the low–fidelity model $u_L(\boldsymbol{x}; \boldsymbol{w}_L)$ is a standard FFNN. The high–fidelity model u_H can be expressed generally as:

$$u_H(\boldsymbol{x}; \boldsymbol{w}) = \mathcal{L}_{\mathcal{H}}(\boldsymbol{x}, u_L(\boldsymbol{x}; \boldsymbol{w}_L); \boldsymbol{w}_H) + \mathcal{N}\mathcal{N}_{\mathcal{H}}(\boldsymbol{x}, u_L(\boldsymbol{x}; \boldsymbol{w}_L); \boldsymbol{w}_H) \tag{32}$$

where $\mathcal{L}_{\mathcal{H}}$ is a linear transformation of u_L, and $\mathcal{N}\mathcal{N}_{\mathcal{H}}$ is a neural network correcting the low–order model u_L. The rationale for this linear/non–linear splitting is that, if the low–fidelity model is well–designed, one would expect a strong linear correlation between uH and uL; by explicitly incorporating a linear correlation term, the learning process is guided to more effectively capture this type of relationship. Here, $\boldsymbol{w} = [\boldsymbol{w}_L, \boldsymbol{w}_H]$ encapsulates the parameters of both low– and high–fidelity models.

The optimization problem in the multi–fidelity setting becomes:

$$w^*, \gamma^* = \underset{\boldsymbol{w}\in\mathbb{R}^M, \gamma\in\mathbb{R}^P}{\operatorname{argmin}} \left[\frac{1}{N_{\text{obs}}} \sum_{i=1}^{N_{\text{obs}}} \left| u_i^{\text{obs}} - u_H(\boldsymbol{x}_i^{obs}; \mathbf{w}) \right|^2 + \mathcal{L}_{phys}(u_H(\cdot; \boldsymbol{w}), \gamma) \right.$$
$$\left. + \frac{\alpha_{\text{low}}}{N_{\text{low}}} \sum_{i=1}^{N_{\text{low}}} \left| u_i^{\text{low}} - u_L(\boldsymbol{x}_i^{low}; \mathbf{w}_{\boldsymbol{L}}) \right|^2 \right]$$

where u_H is given by(32). Here, the low–fidelity term $\frac{\alpha_{\text{low}}}{N_{\text{low}}} \sum_{i=1}^{N_{\text{low}}} \left| u_i^{\text{low}} - u_L \right|^2$ incorporates additional information into the optimization, improving the model's ability to generalize even with sparse highfidelity data.

A more advanced multi–fidelity approach [146] involves leveraging a surrogate model trained on data generated through a numerical solver. This allows us to capture parametric dependencies in the solution. The corresponding optimization problem for training uL is:

$$w_L^* = \underset{\boldsymbol{w}_{\boldsymbol{L}}\in\mathbb{R}^{M_L}}{\operatorname{argmin}} \left[\frac{1}{N_{low}} \sum_{i=1}^{N_{low}} \left| u_i^{low} - u_L\left(\boldsymbol{x}_{\boldsymbol{i}}^{low}, \gamma_i^{low}; \boldsymbol{w}_L\right) \right|^2 + R(\boldsymbol{w}_L) \right],$$

where $R(\boldsymbol{w}_L)$ is a regularization term that may include physics–based constraints. Once trained, the parametrized low–fidelity model uL is fixed (i.e., its parameters are kept equal to $\boldsymbol{w}_{\boldsymbol{L}}^*$) and used as a prior for the high–fidelity model:

$$u_H(x, \gamma; w_H) = \mathcal{L}_H(x, u_L(x, \gamma; w_L^*); w_H) + \mathcal{N}\mathcal{N}_H(x, u_L(x, \gamma; w_L^*); w_H),$$

where one often sets LH (x, uL; wH) ≡ uL to enforce the low-fidelity model as a prior. We remark that, unlike in (32), the multi–fidelity expression accounts for the parametric dependence of the solution, that is the NN explicitly depends on the parameters γ.

The final optimization for the inverse problem becomes:

$$\boldsymbol{w}_{\boldsymbol{H}}^*, \gamma^* = \underset{\boldsymbol{w}_{\boldsymbol{H}}\in\mathbb{R}^{M_H}, \gamma\in\mathbb{R}^P}{\operatorname{argmin}} \left[\frac{1}{N_{obs}} \sum_{i=1}^{N_{obs}} \left| u_i^{obs} - u_H\left(\boldsymbol{x}_i^{obs}, \gamma; \boldsymbol{w}_H\right) \right|^2 \right. \tag{33}$$
$$\left. + \mathcal{L}_{phys}(u_H(\cdot, \gamma; \boldsymbol{w}_H), \gamma) \right].$$

This approach leverages the strengths of both low– and high–fidelity models, balancing computational efficiency with accuracy. It is particularly advantageous in settings where parametric variations significantly influence the solution.

PINNs for data fitting. Very frequently, observations are affected by noise, so we might be interested in estimating the denoised solution of a PDE, starting from noising data. This represents another type of problem that can be effectively addressed by PINNs. Let us consider the example of estimating the blood velocity u in a vessel. Let $\boldsymbol{\Omega} \in \mathbb{R}^3$ be the computational domain (modelled by a curved cylinder), with Γ_{wall}, Γ_{in} and Γ_{out} representing impermeable, inflow, and outflow boundaries, respectively. For any time $t \in (0, T\ )$ of the simulation, the velocity $\boldsymbol{u} = \boldsymbol{u}(x, t)$ satisfies the Navier–Stokes equation

$$\begin{cases} L_M(\boldsymbol{u}, p) \coloneqq \rho \dfrac{\partial \boldsymbol{u}}{\partial t} - \mu \Delta \boldsymbol{u} + \rho(\boldsymbol{u} \cdot \nabla)\boldsymbol{u} + \nabla p = 0 & in\ \Omega \\ L_D(\boldsymbol{u}) \coloneqq \nabla \cdot \boldsymbol{u} = 0 & in\ \Omega \\ \boldsymbol{u} = 0 & on \Gamma_{wall} \end{cases} \tag{34}$$

and we dispose of the noisy observation $\boldsymbol{u}_i^{obs} \simeq \boldsymbol{u}(\boldsymbol{x}_{\boldsymbol{i}}^{obs}, t_i^{obs})$ for $i = 1, \dots, N_{\text{obs}}$, with $\boldsymbol{x}_{\boldsymbol{i}}^{obs} \in \Omega$ and $\boldsymbol{x}_{\boldsymbol{i}}^{obs} \in (0, T\ )$. We are interested in estimating the velocity of the blood at certain points of the inflow and outflow boundaries and at given times, by using a PINN.

We might design a single NN that, given in input the independent variables $\mathbf{x} \in \mathbb{R}^3$ and $t \in \mathbb{R}$, provides both the velocity u and the pressure p as outputs; otherwise, we might use two different NNs, one providing the velocity and the other the pressure. In both cases, we denote by $\boldsymbol{u_{NN}}(\boldsymbol{x}, t; \boldsymbol{w})$ and $p_{NN}(\boldsymbol{x}, t; \boldsymbol{w})$ the solution computed by the PINN, and denote by $\mathcal{J}_M$ and $\mathcal{J}_D$ two (not necessarily disjoint) subsets of the indices set $\mathcal{J}_{obs} = \{1, \dots, N_{obs}\}$. Then we define the losses

$$\mathcal{L}_{obs}(w) = \frac{1}{N_{obs}} \sum_{i \in \mathcal{J}_{obs}} \left\| \boldsymbol{u}_i^{obs} - \boldsymbol{u}_{NN}(\boldsymbol{x}_i^{obs}, t_i^{obs}; \boldsymbol{w}) \right\|^2,$$

$$\mathcal{L}_{\mathcal{M}}(w) = \frac{1}{|\mathcal{J}_{\mathcal{M}}|} \sum_{i \in \mathcal{J}_{\mathcal{M}}} \left\| L_M \left(\boldsymbol{u}_{NN}(\boldsymbol{x}_i^M, t_i^M; \boldsymbol{w}), p_{NN}(\boldsymbol{x}_i^M, t_i^M; \boldsymbol{w}) \right) \right\|^2,$$

$$\mathcal{L}_{\mathcal{D}}(w) = \frac{1}{|\mathcal{J}_{\mathcal{D}}|} \sum_{i \in \mathcal{J}_{\mathcal{D}}} \left(L_D \left(\boldsymbol{u}_{NN}(x_i^D, t_i^D; w) \right) \right)^2,$$

and look for

$$w^* = \underset{\boldsymbol{w} \in \mathbb{R}^M}{\operatorname{argmin}} [\mathcal{L}_{obs}(\boldsymbol{w}) + \alpha_M \mathcal{L}_{\mathcal{M}}(\boldsymbol{w}) + \alpha_D \mathcal{L}_{\mathcal{D}}(\boldsymbol{w})],$$

With α_M and α_D suitable weights. The term $\mathcal{L}_{obs}$ of the loss function incorporates data, while $\mathcal{L}_{\mathcal{M}}$ and $\mathcal{L}_{\mathcal{D}}$ encode the learning biases. One way to interpret this approach is to view it as a fitting problem, where the terms incorporating physics act as regularization terms, favouring solutions that adhere to known physical principles.

with αM and αD suitable weights. The term Lobs of the loss function incorporates data, while LM and LD encode the learning biases. One way to interpret this approach is to view it as a fitting problem, where the terms incorporating physics act as regularization terms, favouring solutions that adhere to known physical principles.

We observe that also in this case the formulation of the problem is very similar to that of the direct one.

Thanks to their flexibility, PINNs can be applied even when boundary conditions or initial conditions are missing or not completely known. PINNs can be effective for ill–posed problems and in the small data regime (indeed when data are scarce, learning biases supersede missing measurements).

Enforcement of Dirichlet boundary conditions. We now discuss how to enforce Dirichlet boundary conditions in the PINN framework. The approaches discussed here can be applied to the different types of problems we have discussed so far, including the resolution of PDE, inverse problems and data fitting. Let us consider the second–order elliptic equation (12) but with Dirichlet boundary conditions instead of the Neumann ones:

$$\begin{cases} -\Delta u + \gamma u = f, & in\ \Omega \\ u = g & \text{on } \partial\Omega \end{cases}$$

We may work following different approaches. The first way consists of defining the residual corresponding to the boundary condition as

$$Res^{BC}[u(x)] = u(x) - g(x), \qquad x \in \partial\Omega.$$

and using this one instead of (18)-2 inside the definition of (21)[147].

This approach could be interpreted as analogous of the penalty method of Babuˇska [14] in the Galerkin framework, for which we look for $u \in\ V = H^1(\Omega)$ such that

$$\int_\Omega (\nabla u \cdot \nabla v + \gamma uv - fv) + \alpha_{BC} \int_{\partial\Omega} (u - g)v = 0, \quad \forall v \in V.$$

where $\alpha_{BC} > 0$ is a suitable penalization parameter.

A second way [148]consists of defining the solution as

$$u_{NN}(x; w) = G(x) + A(x)\tilde{u}_{NN}(x; w).$$

where $G(\boldsymbol{x})$ is a lifting of $g(\boldsymbol{x})$ to Ω, i.e. a function $G\colon \overline{\Omega} \to \mathbb{R}$ such that $G|_{\partial\Omega}$ = g and contains no adjustable parameters; A(x) is a function named mask defined on $\overline{\Omega}$ such that $A|_{\partial\Omega} = 0$ (for instance, if $\Omega = (0,1)^2$, we could take $A(x) = x_1x_2(1 - x_1)(1 - x_2)$); while $\tilde{u}_{NN}(\boldsymbol{x};\boldsymbol{w})$ is a single–output FFNN with parameters w and input x.

The optimal values of the parameters are computed by minimizing the loss function

$$\mathcal{L}(w) = \mathcal{L}_{\mathcal{PDE}}(w) = \frac{1}{2N_{PDE}} \sum_{i=1}^{N_{PDE}} \left(Res^{PDE}\left(u_{NN}(x_i^{PDE}; w)\right)\right)^2.$$

Other strategies to impose Dirichlet conditions rely on formulating the problem as a constrained optimization problem via the augmented Lagrangian method[149].

2.3 PINN Framework Construction for LPBF Thermal Process

2.3.1 Definition of Spatial–Temporal Computational Domain

This section provides a detailed description of the physical model of the LPBF process used as input for the PINN (Input Fig. 25. The computational domain spans 4 mm in the scanning direction (x), 2 mm in width (y), and 3 mm in depth (z), as shown in fig. 3. These dimensions were chosen to reflect the experimental configuration and to minimize boundary effects that could distort the thermal field. In particular, the domain length ensures that a representative bead-on-plate of approximately 2 mm can be formed while leaving sufficient space ahead of and behind the heat source to allow for realistic cooling and heating gradients. The width and the depth were selected based on characteristics of the laser system and configuration used for subsequent tuning and validation steps. To allow for thermal preconditioning of the material, the temporal domain begins at t = -0.1 s, with the laser initially inactive, and ends when the laser completes the 2 mm process segment. The total simulation time is therefore determined by the laser scanning speed and the target laser path length. To simplify the complex multi-physics phenomena involved in keyhole LPBF while preserving the dominant thermal mechanisms, the following assumptions were made:

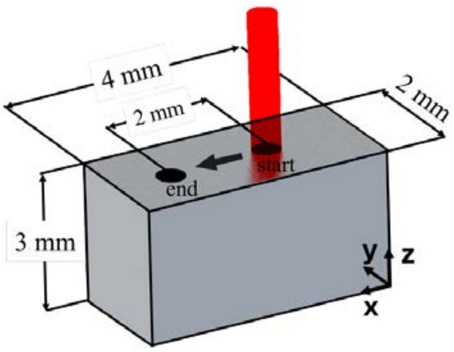

Fig. 25 Domain considered

- The powder layer on the single track surface is neglected
- The material is treated as a continuous solid medium
- The material is considered isotropic and homogeneous, with temperature-dependent thermophysical properties
- Fluid flow, recoil pressure and convection are neglected
- The laser beam is modeled as an equivalent volumetric heat source

The temperature distribution (T) is given by a transient Fourier equation

$$\rho(T)\tilde{C}_p(T)\frac{\partial T(\boldsymbol{x},t)}{\partial t} - \nabla \cdot \left(\tilde{k}(T)\nabla T\right) - q_v(\boldsymbol{x},t) = 0 \quad (35)$$

Where x represents the space coordinates x, y, and z, t represents time, $\rho(T)$ ([kg·m−3]), $\tilde{C}_p(T)$ ([J·Kg−1·K−1]), and $\tilde{k}(T)$ ([W·m−1·K−1]) represent respectively the temperature-dependent density, apparent heat capacity, and effective thermal conductivity of the material. The latter two quantities extend the material's intrinsic heat capacity and thermal conductivity to account for the different behavior in the melting phase, which is not explicitly modeled. qv represents the volumetric heat input from the moving laser beam. To capture the characteristic morphology of keyhole-mode, a double-conical volumetric heat source—originally derived from the three-dimensional conical model by Wu[154] and later refined by Farhang[155]—was adopted in this study. The source is shown in Fig. 26 and is composed of two separate volumetric contribution:

- q_{v1} (see eq.(8)) describes the lower conical region, ranging from the bottom of the keyhole at zb to the intermediate interface at zi in a distance equal to Hu
- q_{v2} (see eq.(9)) defines the upper conical region, extending from zi up to the top surface at zt in a distance equal to Hl

The corresponding radial profiles r1 and r2, which vary linearly along the height of each cone, are defined in eq.(10)(11)

This double-conical formulation can also be readily adapted to conduction-mode by reducing the cone depths and adjusting the upper and lower radii accordingly, thereby providing a unified and scalable volumetric heat source representation across different LPBF melting regimes.

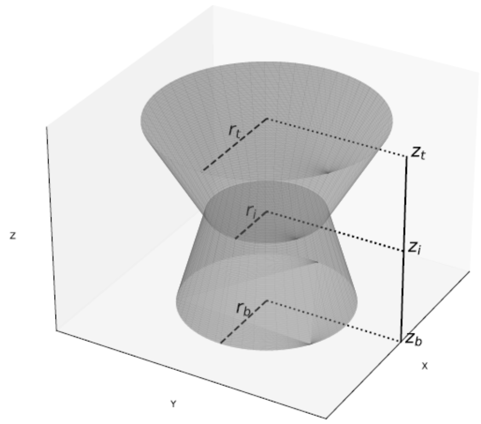

Fig. 26: Double conical heat source with the six parameters showed

In order to solve equation (35) appropriate boundary and initial conditions were set as detailed below:

- Initial temperature was set equal to room temperature (25 ⁰C) in all the domain:

$$T(x,t,z,0) = T_0(x,y,z) = 298\,K \tag{36}$$

- A Dirichlet with fixed temperature at the bottom:

$$T(\boldsymbol{x},t) = 293\,K, \quad x \in \partial \tag{37}$$

- An adiabatic Neumann condition at the external boundaries:

$$\left.\frac{\partial T}{\partial \hat{n}}\right|_{\partial\Omega} = 0 \tag{38}$$

- A Robin condition to account for heat loss for external convection and radiation at top

$$\tilde{k}\nabla T - h(T - T_0) - \epsilon\sigma(T^4 - T_0^4) = 0 \tag{39}$$

with h convective coefficient, equal to 20 $\mathrm{W \cdot m^{-2}K^{-1}}$, ϵ material emissivity, equal to 0.9 while σ is the Stefan–Boltzmann constant (5.67×10^{-8} $\mathrm{W \cdot m^{-2}K^{-4}}$,). Since for the keyhole model the material undergoes extremely high temperature gradients reaching temperature exceeding the evaporation point it was necessary to define the material's properties accordingly: Constant properties given by literature were used only when the temperature was below the melting temperature (Tm), while for melting, vaporization and over vaporization temperature the properties were The temperature-dependent trends of the material properties adopted in the model are reported in detail in Fig. 27.

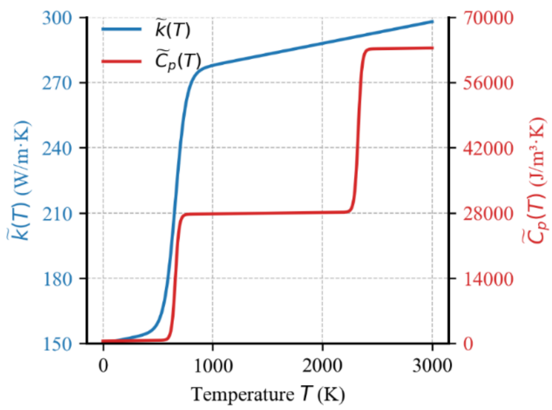

Fig. 27 Temperature-dependent apparent specific heat capacity and effective thermal conductivity of the aluminum alloy in PINN.

2.3.2 PINN Network and Loss Function Design

This section presents the structures and implementation of the proposed Physics-Informed Neural Network developed to solve the thermal field during keyhole LPBF. The framework combines a feedforward neural network architecture with the information given by the governing physical laws The neural network is trained to satisfy both the energy conservation equation (eq.(35)) and the initial/boundary conditions (section 2.3.1) described in section 2.3. without any experimental data. Fig. 28 shows the scheme of the proposed PINN model.

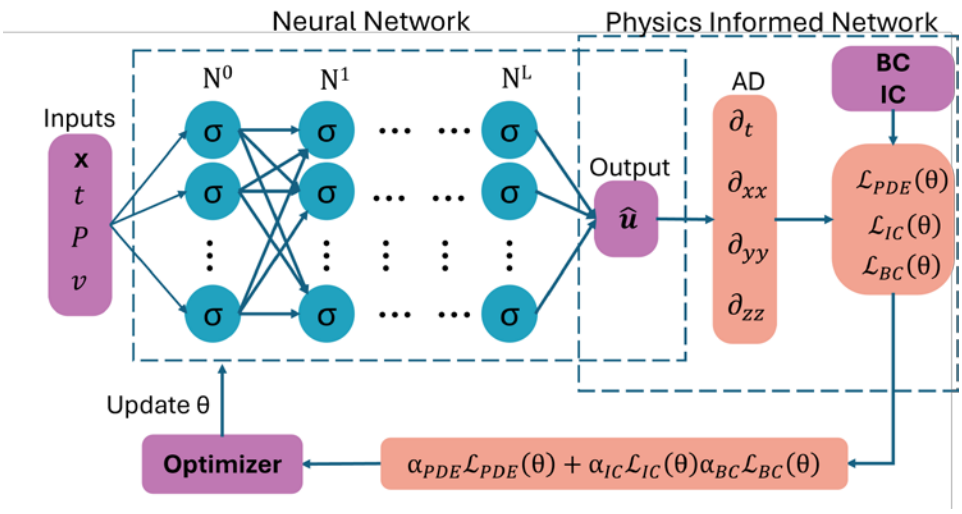

Fig. 28 Scheme of a generic PINN model

To approximate the solution of partial differential equations governing physical processes, Physics-Informed Neural Networks employ standard feedforward neural networks as surrogate function approximators. The network is trained not only to fit data, but also to satisfy the underlying physical laws expressed as differential equations, initial, and boundary conditions. Following the elaboration proposed by Lu et al.[156] we can define a fully-connected feedforward neural network with L-layers, denoted as $\mathcal{N}^L(x)$: $\mathbb{R}^{d_{in}} \rightarrow \mathbb{R}^{d_{out}}$, where d_{in} and d_{out} are the input and output dimensions, respectively. The network consists of an input layer, multiple hidden layers with $N_l$neurons each and nonlinear active functions, and an output layer. The network can be mathematically expressed as follows:

Input layer: $\mathcal{N}^0(x) = x \in \mathbb{R}^{d_{in}}$

Hidden layers:$\mathcal{N}^\ell(x) = \sigma\left(W^l\mathcal{N}^{\ell-1}(x) + b^l\right) \in \mathbb{R}^{N_l}$ for $1 \le l \le L-1$

Output layer: $\mathcal{N}^\mathcal{L}(x) = W^L\mathcal{N}^{\mathcal{L}-1}(x) + b^L \in \mathbb{R}^{d_{out}}$

with σ nonlinear activation function, $W^l \in \mathbb{R}^{N_l x N_{l-1}}$ weight matrix and $\boldsymbol{b}^l \in \mathbb{R}^{N_l}$ the bias vector, trainable parameters indicate with $\theta.$ Given a generic PDE with a different operator $\mathcal{N}[;\, \lambda]$ parameterized by λ:

$$\frac{\partial u}{\partial t} + \mathcal{N}[u(t,x);\lambda] = 0, \quad x \in \Omega \subset R^d, \quad t \in [0,T] \tag{40}$$

with such initial and boundary conditions:

$$u(0,x) = u_0(x), \quad x \in \Omega \tag{41}$$

$$\mathcal{B}[u] = 0, \quad x \in \partial\Omega, \quad t \in [0,T] \tag{42}$$

PINN will approximate the solution $\boldsymbol{u(t,x)}$ with $\hat{\boldsymbol{u}}(\boldsymbol{t},\boldsymbol{x},\theta)$ by minimizing the loss function:

$$\mathcal{L}_{TOT}(\theta) = \alpha_{PDE} \cdot \mathcal{L}_{PDE}(\theta) + \alpha_{IC} \cdot \mathcal{L}_{IC}(\theta) + \alpha_{BC} \cdot \mathcal{L}_{BC}(\theta) \tag{43}$$

In the proposed model, each term of the loss function is evaluated over a specific set of training points selected within the computational domain. In particular, the PDE loss term $\mathcal{L}_{PDE}$ (eq.(44)) is computed over a batch of collocation points, which are sampled within the space-time domain and used to enforce the governing differential equation. The boundary condition loss term L_{BC} (eq.(45)) is computed over a set of boundary points located on the spatial boundaries of the domain, while the initial condition term L_{IC} (eq.(46)) is evaluated on a set of initial points corresponding to the initial time. For each of these three components, the median squared error is used as a measure of discrepancy between the model's output and the expected physical behaviour.

$$\mathcal{L}_{PDE}(\theta) = \frac{1}{N_{coll}} \sum_{i=1}^{N_{coll}} || \frac{\partial \hat{u}(t_{coll}^i, x_{coll}^i; \theta)}{\partial t} + \mathcal{N}[\hat{u}(t_{coll}^i, \boldsymbol{x}_{coll}^i; \theta); \lambda] ||_2^2 \quad (44)$$

$$\mathcal{L}_{IC}(\theta) = \frac{1}{N_{ic}} \sum_{i=1}^{N_{ic}} ||\hat{u}(0, x_{ic}^i; \theta)||_2^2 \quad (45)$$

$$\mathcal{L}_{BC}(\theta) = \frac{1}{N_{bc}} \sum_{i=1}^{N_{bc}} ||\mathcal{B}[\hat{u}(t_{bc}^i, x_{bc}^i; \theta)]||_2^2 \quad (46)$$

Each term of the loss function is associated with a different weight indicated in eq. (13) with α_{PDE}, α_{BC} and α_{IC}. These parameters were selected equal to 5·103 for α_{BC} and α_{IC} and 100 for α_{PDE} to account for the different magnitude order of the three losses terms. A systematic hyperparameter tuning was conducted to identify the most effective network configuration, focusing on four key aspects: number of hidden layers (N^L), number of neurons per layer (N_l), the activation function (σ), and the sampling strategy used to generate collocation points. After the tuning, the model was trained taking as inputs the 13 parameters specified in Table 2 and, using the Limited-memory Broyden–Fletcher–Goldfarb–Shanno (L-BFGS) algorithm, the loss function was minimized.

Table 2 Model inputs grouped by category and corresponding output.

Inputs														Output
Time	Space			Material		Laser		Heat Source Geometry						Temperature
t	x	y	z	$\tilde{k}$	$\tilde{c}$	P	v	r_t	r_i	r_b	H_u	H_i		T

2.4 Hyperparameters tuning and model training

Table Table 3 summarizes the hyperparameters tested. Each one was evaluated based on its ability to minimize the PDE residual and maintain stable convergence across training.

Table 3 Hyper parameters tested

Hidden layers	Neurons	Activation function	Collocation points sampling
4,**8**	16,**32**,64	ReLU, Tanh, **Sin**, Swish	Grid, Random, Sobol, **Moving**

The four activation functions tested can be seen in Fig. 29, along with the first and second derivatives.

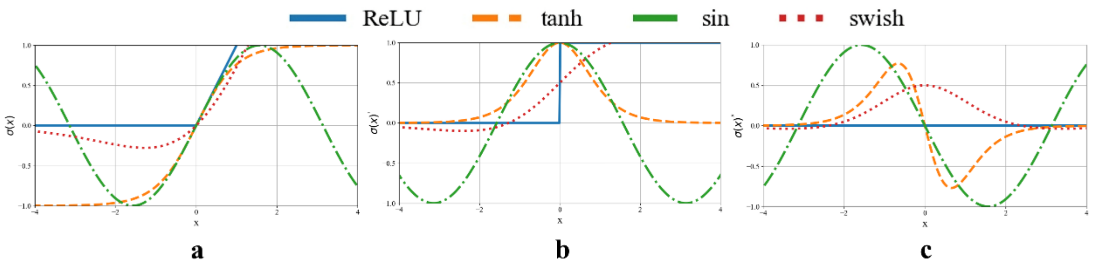

Fig. 29 Activation functions (a) tested with the first (b) and second (c) derivatives

The four functions were tested keeping the other parameters the same over 25000 cumulative iterations. The ReLU (rectified linear unit) is defined as the non-negative part of its argument and is a very popular function in machine learning models due to its simplicity and fast implementation. However, the training of the proposed PINN model with ReLU function, lead to severe numerical instabilities and PDE residual losses rapidly diverges (see Fig. 30a) after around 700 iterations. This is due to the lack of continuous second derivatives (being zero almost everywhere as shown in Fig. 29c), not suitable for such applications. On the contrary, the Swish activation function provided a significant improvement in training stability compared to ReLU, avoiding exploding losses, even if the instability remained as can be seen by the spikes of the graph. However, this improvement came at the cost of increased training time, due to the more complex structure of the activation function. Furthermore, swish resulted in a slower loss reduction (see Fig. 30b) com- pared to traditional activation functions used for PINNs. Tanh showed a smoother and fast training (see Fig. 30c) but slower than the sin activation function (Fig. 30d) that was ultimately adopted in the final model

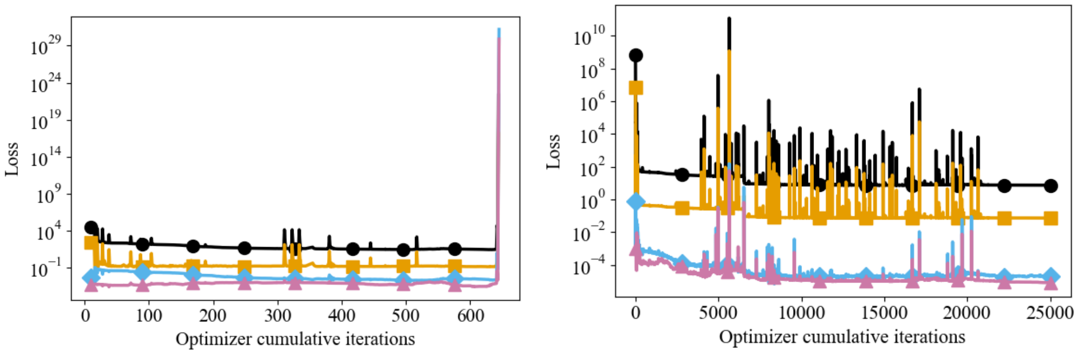

(a)ReLu(x) (b)Swish(x)

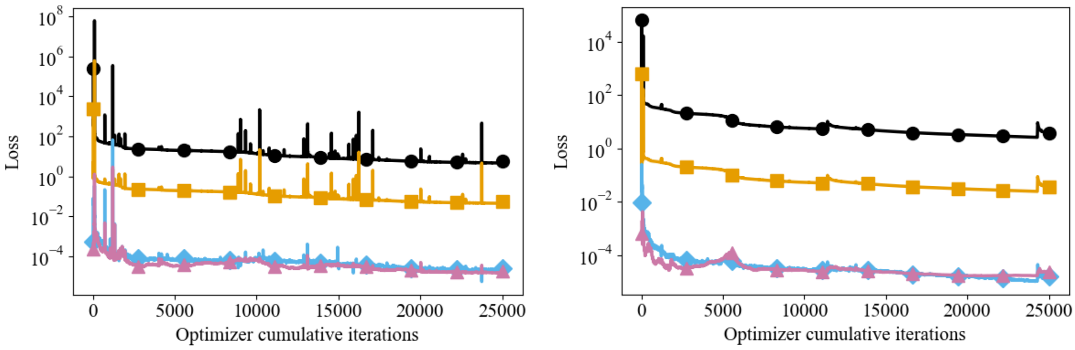

(c)Tanh(x) (b)Sin(x)

Fig. 30 Comparison of different activation functions performances, with black circles L_{TOT}, yellow squares L_{PDE}, blue rhombuses L_{BC} and magenta triangle L_{IC}

Regarding the network's architecture, configurations with only 4 layers demonstrated poor generalization capabilities, regardless the number of neurons used. Therefore, a deeper architecture with 8 hidden layers was selected as the most viable option. On the other hand, increasing the number of neurons per layer to 64 significantly increased the training time without notable improvements in accuracy. The added complexity not only slowed convergence but also made the model more prone to unstable optimization, likely due to over-parameterization. A configuration with 32 neurons per layer was found to provide a good balance, allowing for efficient training while maintaining stability and accuracy. Finally, the comparison between four different collocation point sampling (left side in Fig. 31) strategies was carried out. The right column of Fig. 31 displays the kernel density estimation (KDE) of the PDE residuals after 10,000 training iterations, projected onto a central cross-section of the domain during the laser-material interaction. The white contour highlights the region containing the 50% most significant PDE loss contributions. Across all methods, this region is located near the top surface of the domain (z close to 0), where thermal gradients are strongest. In contrast, at deeper locations (low z values), the residuals are consistently smaller, indicating minimal temporal or spatial variation in temperature. Moreover, the moving strategy resulted in more stable and predictable convergence profiles, as no sharp peaks were observed in the loss trend (Fig. 32) even if the overall trend is slower compared to the other strategies. This can be also attribute to the higher number of points being located to the higher gradient zone, so with higher PDE loss but at the same time higher importance

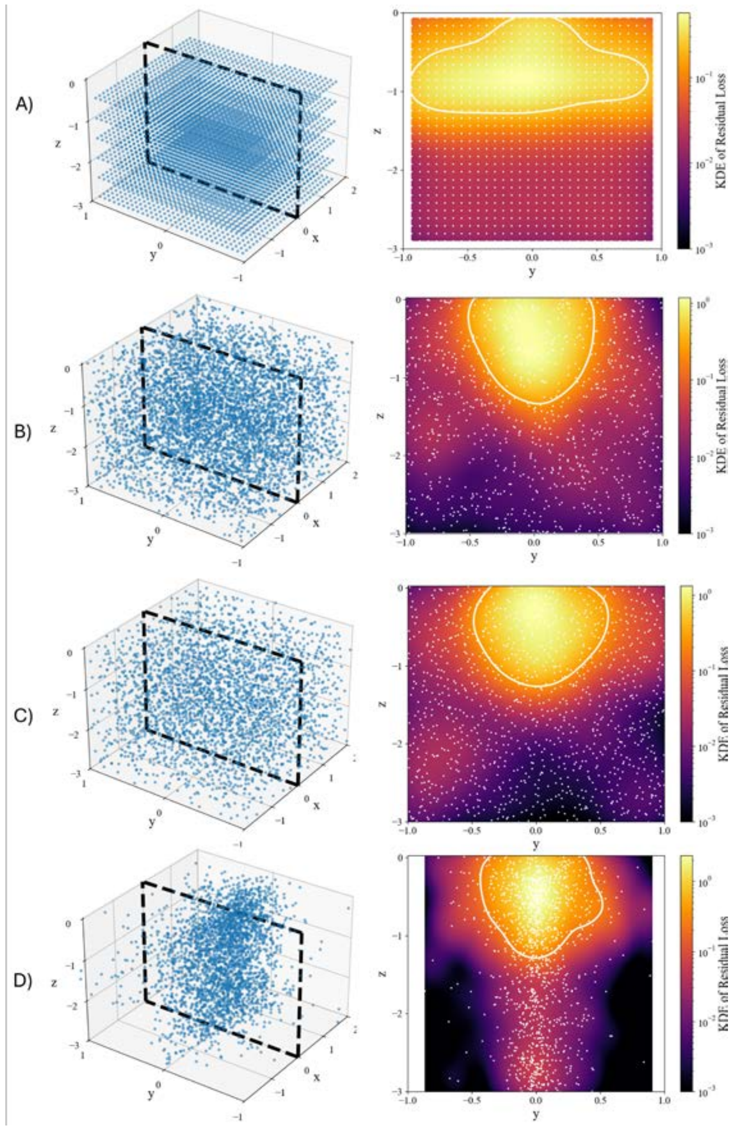

Fig. 31 Sampling strategies comparison for collocation points. Left: 3D spatial distribution of collo- cation points A) Grid, B) Random, C) Sobol, D) Moving. Right: kernel density estimation (KDE) of the PDE residuals after 10k iterations; the white contour encloses the region contributing 50% of the total residual loss.

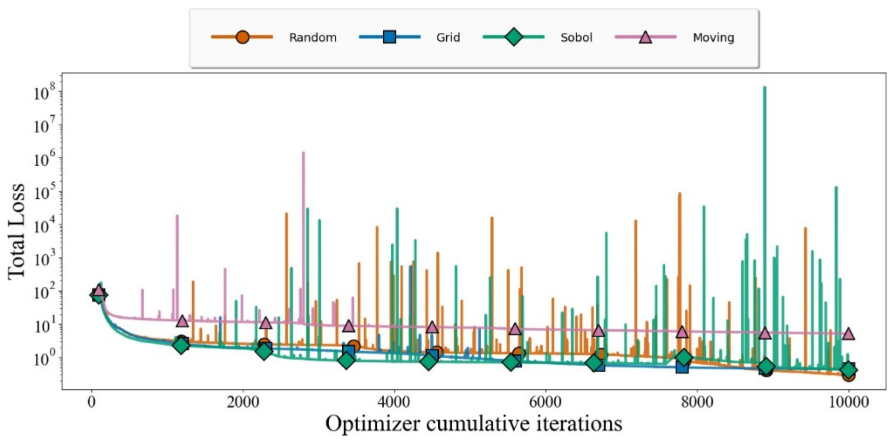

Fig. 32 Comparison of total loss trends for the different sampler strategies

In the end the moving sampling strategy was chosen. The final PINN model was trained to reach a PDE loss lower than 10^{-5} a boundary and initial loss lower than 10^{-6} with a final total loss of 10^{-5}. The training was performed using a GPU RTX 4090 with dedicated 24 Gb and the total time was hours.

2.5 Chapter Summary

This chapter focuses on the thermal mechanisms and numerical modelling challenges of the keyhole-mode Laser Powder Bed Fusion (LPBF) process and establishes a Physics-Informed Neural Network (PINN) framework for rapid temperature field prediction. The main contents and contributions are summarized as follows:

1. Problem Definition and Motivation

Three LPBF melting modes—conduction, transition, and keyhole—were reviewed to clarify their influence on melt pool geometry and part density. Although the keyhole mode tends to increase porosity, it remains valuable for thick-wall and large-scale fabrication due to its high energy coupling efficiency and deep penetration capability. Conventional high-fidelity numerical models (CFD/FEM/VOF) are computationally expensive, while purely data-driven models lack physical consistency and generalization ability. Therefore, a physics-constrained yet computationally efficient modelling approach is required。

2. Mathematical Modelling Foundation

The temperature field governing equation was derived from the Fourier–Kirchhoff heat conduction equation. The computational domain, temperature-dependent material properties, and initial/boundary conditions were systematically defined. Convective and radiative heat transfer at boundaries were linearized into an equivalent heat transfer coefficient, providing a computable physical constraint for the PINN.

3. Heat Source Model Selection and Validation

After comparing surface and volumetric heat source models, a Double-Conical volumetric heat source was selected to represent energy absorption in keyhole mode. This model features clear physical interpretability and tunable geometry, capable of describing asymmetric deep-melt energy deposition while being extendable to conduction-mode melting, thus ensuring scalability for cross-mode modelling and process optimization.

4. Computational Domain and Boundary Conditions

A 3D computational domain consistent with experimental dimensions was defined (scan length

4 mm, width 2 mm, depth 3 mm), with a temporal domain from $t=-0.1s$ (preheating) to the completion of a 2 mm track. Boundary conditions included fixed temperature at the bottom, adiabatic sides, and Robin-type top boundaries (convection + radiation), ensuring physical reproducibility and boundary consistency.

5. PINN Framework and Implementation

Assuming pure heat conduction (neglecting powder effects but retaining temperature-dependent properties and surface convection/radiation), The loss function consists of PDE residuals and initial/boundary terms, enabling unsupervised training without experimental data. Systematic hyperparameter optimization was performed to enhance stability and accuracy:

• Network architecture: 8 layers with 32 neurons per laye;

• Activation function: sinusoidal functions outperformed ReLU/Swish/Tanh,faster convergence;

• Sampling strategy: a moving collocation method improved residual distribution and convergence in high-gradient regions;

• Optimization algorithm: L-BFGS minimized physical residuals to the preset tolerance.

6. Advantages and Applicability

The proposed PINN + Double-Conical heat source framework efficiently solved the keyhole-mode temperature field under limited or no data supervision, achieving a computational cost far lower than CFD while maintaining strong physical consistency and interpretability. The geometric flexibility of the heat source model also enables scalability across process parameters and melting modes, providing a potential foundation for real-time monitoring and closed-loop control.

Chapter 3: PINN Model Calibration and Application

3.1 Introduction

In the previous chapter, a Physics-Informed Neural Network (PINN) model based on a double-conical volumetric heat source was successfully trained, enabling physics-constrained modelling of the laser melting process under keyhole mode conditions. However, the trained model could not yet be directly applied for temperature field prediction or process optimization, as parameter calibration and experimental validation were still required.

To enable the model to automatically adapt to different laser process conditions, the geometry and dimensions of the heat source were defined by five key parameters, which were assumed to have identifiable functional relationships with the laser process parameters (power and scanning speed). This relationship was established through inverse analysis, in which the unknown parameters were identified by minimizing the discrepancy between model predictions and experimental measurements, thereby achieving volumetric heat source model calibration. During the calibration stage, multiple sets of experiments were analyzed to construct the mapping relationships between laser power, scanning speed, and the geometric parameters of the heat source. After calibration and validation, the PINN model could accurately predict melt pool temperature distribution and geometric dimensions within milliseconds, relying solely on process parameter inputs, with extremely low computational cost and without manual tuning.

Based on this, to calibrate the model, a preliminary setup was built without using powder, in order to evaluate the keyhole during a bead-on-plate interaction similar to welding. With the same setup, a PINN-driven process optimization and validation study was carried out. By evaluating multiple power–speed combinations, the PINN rapidly identified the optimal parameters that yielded the target melting depth, which were subsequently validated through experiments, significantly reducing the time and cost required for process optimization.

3.2 Experiment setup

To obtain melt pool dimension (MPD) and microstructural data for the calibration of the thermo-microstructural model, single-track laser melting scans were performed on aluminum sheets plates under various combinations of laser power and scanning speed, without applying a powder layer. Although laser scanning on powder layers better represents the actual PBF-LB manufacturing process, it introduces more complex and challenging conditions for model calibration. The stochastic nature of the powder layer adds “noise” to the measurement of melt pool dimensions and microstructural features. In contrast, laser melting on an substrate provides cleaner and more controlled data, which facilitates model calibration, although the effects of the powder layer should be considered in future studies. A nLight Alta Yb:Fiber CW multi-mode laser source with a wavelength of 1070 nm, a maximum output power of 3 kW and a delivery fiber core diameter of 50 μm was employed as reference and subsequent testing of the PINN model. The beam was focused and displaced by means of a galvo scanner (Scanlab Hurry SCAN 30) equipped by a Wave- length F-Theta fused silica lens with a focal length of 160 mm that allowed a theoretical spot equal to 65 μm. The laser characteristics are summarized in table 1. The laser beam directly irradiated the process area, with the focus positioned on the sample surface at the center of the joint. A dedicated clamping system was designed and installed beneath the scanning optics do ensure proper sample positioning and minimize the gap the sheets (see Fig. 33)

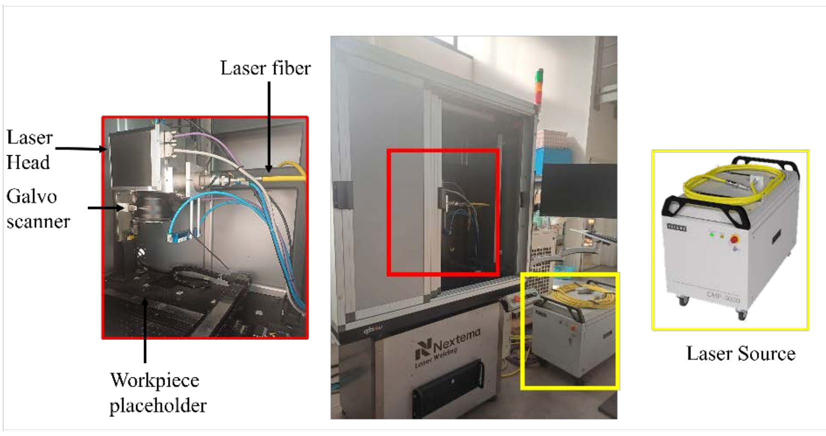

Fig. 33 Experimental Setup

Table 4 Experimental equipment

Maximum Power [W]	1400
Collimation length [mm]	120
Focal length [mm]	160
Fiber core diameter [μm]	50
Beam divergence [mm·mrad]	2
Focalized spot diameter [μm]	65
Wavelength [nm]	1064

After bead-on-plate experiment, cross-section of the samples was prepared using electrical discharge machining (EDM) and then mounted in phenol formaldehyde resin. The samples were ground with silicon carbide abrasive papers (80 to 2500 grit), polished with a 1 μm alumina suspension, and finally etched with Keller's reagent (a mixture of nitric acid, hydrochloric acid, and hydrofluoric acid) to reveal the melt pool geometry. Geometric measurements were carried out using a Zeiss Observer A1M optical microscope considering three different cross section for each tested to obtain average melt pool depth and width.

3.3 Method of Inverse analysis

This section presents the inverse analysis procedure used to calibrate the volumetric heat source model based on laser power and scanning speed, enabling accurate prediction of melt pool geometry under keyhole-mode. To reach accurate prediction of the melt pool geometry, i.e. the melt pool Depth (MD) and melt pool width (MW) under keyhole mode , it is essential to establish the correlation between the input process parameters and the geometric parameters of the double-conical heat source model within the PINN framework. The correlation was carried out in two subsequent stages:

- Pearson sensitivity analysis to identify the geometric parameters of the double-conical heat source model that exhibit strong correlations with the melt pool dimensions.
- Inverse analysis of the heat source model using the PINN and experimental results

3.3.1 Pearson sensitivity analysis

To extract the dimension of the melt pool from the temperature field predicted by the PINN and to fully exploit its potential in inverse analysis, a differentiable formula is employed as follows:

$$MD(x)_{max} = \int_{z_{min}}^{z_{max}} \sigma(T_\theta(x,0,z) - T_m)dz$$

$$MW(x)_{max} = \int_{y_{min}}^{y_{max}} \sigma(T_\theta(x,y,z_{max}) - T_m)dy$$

where σ is smooth approximation function, such as the sigmoid or tanh, which ensures that the geometric evaluation formula remain continuous and differentiable throughout the optimization process. T_m represent the material melting temperature, and T_θ corresponds to the temperature field predicted by the PINN. The condition y=0 indicates the vertical plane along the laser scanning direction width where MD is measured, while z_{max} denotes the top surface of the computational domain where MW is measured. Once the spatial distributions of MD and MW along the laser scanning direction are obtained, the maximum value obtained is the global maximum MD and MW.

To identify which volumetric heat source parameters most significantly influence the resulting melt pool morphology in PINN, a Pearson correlation analysis was conducted. This method quantifies the linear relationship between each heat source parameter (Rt, Ri, Rb, Hu, Hl)— and the melt pool dimensions: MD and MW. The Pearson correlation coefficient (PCC) r is defined as: PINN

$$r = \frac{\sum (X_i - \bar{X})(Y_i - \bar{Y})}{\sqrt{\sum (X_i - \bar{X})^2 \sum (Y_i - \bar{Y})^2}}$$

where X_i and Y_i denote individual samples of heat source parameters and melt pool dimensions (MD or MW), and $\bar{X}$, $\bar{Y}$ represent their respective mean values. This statistical measure provides a normalized index of linear correlation ranging from –1 to +1, where values close to +1 indicate strong positive correlation, values near –1 indicate strong negative correlation, and values around 0 suggest little to no linear relationship. Positive and negative values represent the direction of correlation, while the absolute magnitude of the PCC reflects the strength of the dependency.

Based on this analysis, the Key Volumetric Heat Source Parameter Governing Depth (KVPD) is defined as the parameter that is most strongly correlated with MD, and the Key Volumetric Heat Source Parameter Governing Width (KVPW) is defined as the parameter most strongly correlated with MW. These two variables are then employed in the subsequent inverse analysis. The remaining VP will be simplified in the reverse analysis.

3.3.2 Assumptions for inverse analysis

Table 5 Process parameters for calibration of PINN

Parameter set	P W	V ms^{-1}
#1	750	0.3
#2	1000	0.1
#3	1400	0.2
#4	1250	0.2
#5	1000	0.3

Subsequently, experiments are conducted as outlined in Table.4 to provide the experimental data required for inverse analysis for calibration. These five parameter sets were chosen based on preliminary exploratory experiments to cover a representative range of the feasible process window where stable and measurable MD and MW could be obtained. These tests yielded measurements of MD and MW under five distinct sets of laser processing parameters. By fitting the experimental results, empirical relationships are established to describe the dependence of the MD and MW on laser power P and scanning speed V, expressed as:

$$MW_{exp} = f_1(P, V)$$

$$MD_{exp} = f_2(P, V)$$

In conjunction with the previously identified key volumetric heat source parameters—KVPD and KVPW—obtained via Pearson correlation analysis, a functional mapping that relate these critical geometric parameters to the process inputs can be proposed:

$$KVPW = g_1(P, V)$$

$$KVPD = g_2(P, V)$$

These empirical relationships between key volumetric heat source parameters and process parameters are subsequently fitted following the inverse analysis.

3.3.3 Inverse analysis for calibration

For each parameter set in table 4, an inverse analysis is performed using the trained PINN model, with 200 independent optimization trials starting from random initial values. The optimization process is carried out using the L-BFGS optimizer by minimizing the following loss function:

$$L_{MD} = ||MD(T_\theta) - MD_{exp}|| + L_{pr}$$

$$L_{MW} = ||MW(T_\theta) - MW_{exp}|| + L_{pr}$$

The first term forces the computed MPD to be close to the experimental value, while the second term L_{pr} forces the optimized model parameters to stay within the training parameter range of PINN and be physically realistic. The inverse analysis flow chart is shown in the Fig. 34.

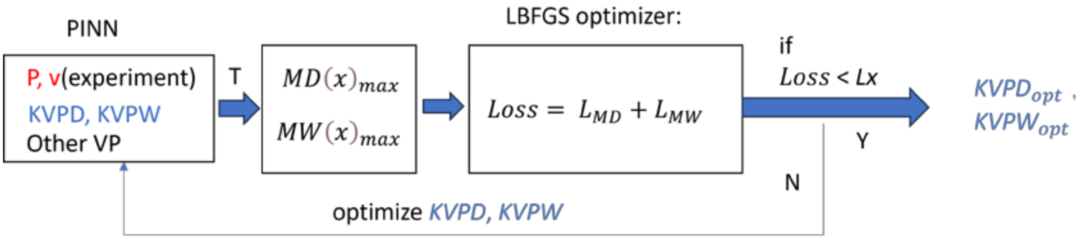

Fig. 34 inverse analysis flow chart

Table 6 Key volumetric heat source parameters optimization

Parameter set	P W	V ms^{-1}	$KVPD_{opt}$	$KVPW_{opt}$	*Remaining VP*
#1	750	0.3	$KVPD1$	$KVPW1$	-

#2	1000	0.1	$KVPD2$	$KVPW2$	-
#3	1400	0.2	$KVPD3$	$KVPW3$	-
#4	1250	0.2	$KVPD4$	$KVPW4$	-
#5	1000	0.3	$KVPD5$	$KVPW5$	-

After each inverse analysis, a set of optimized KVPW and KVPD corresponding to a given experimental process condition (P, V) is obtained. In total, inverse analysis were conducted for five different process settings (as detailed inTable 6). Based on the five sets of optimized parameters and the assumptions in Section 2.5.2, empirical mappings of the form: $KVPW(P,V)$ and $KVPD(P,V)$ are constructed through fitting.

With these relationships established the input space of the PINN model is fully defined as: spatial and temporal parameters (x, y, z, t), process parameters (P, V), and the key heat source geometry parameters $KVPW(P,V)$ and $KVPD(P,V)$, and the remaining volumetric heat source parameters.

3.4 Result of Inverse analysis

3.4.1 Pearson sensitivity analysis

The results of the Pearson sensitivity analysis, presented in Fig. 35, show that the lower cone height (Hl) and the total cone height (Hu + Hl) exhibit the strongest correlation with the melt pool depth. In contrast, the top diameter R_t has a dominant influence on the melt pool width. Notably, an increase in H_u produces a similar effect on melt pool depth as a decrease in H_l. As a result, Hl is defined KVPD is and Rt is defined ad KVPW.

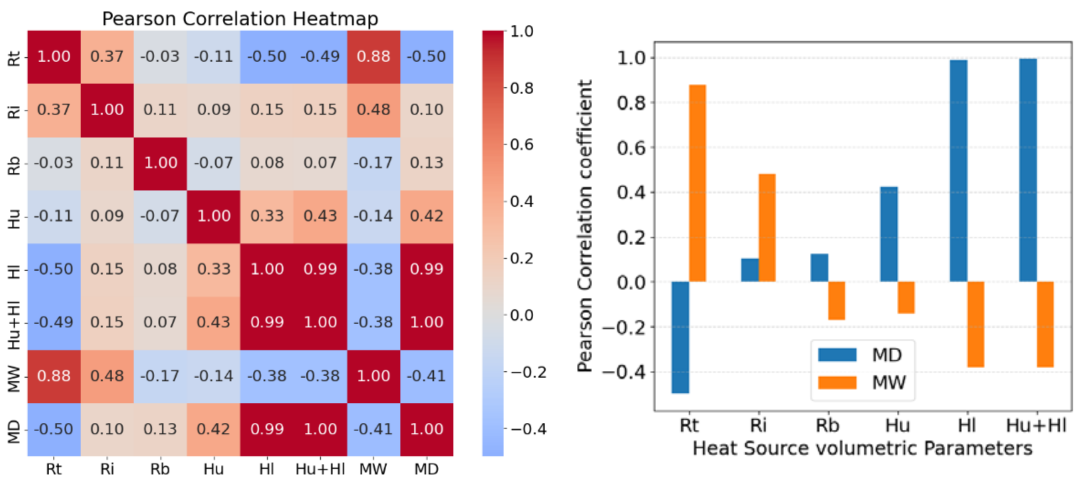

Fig. 35Pearson Correlation Analysis Between heat source volumetric parameters and MW and MD.

Based on these findings, the inverse analysis has been simplified by fixing the middle diameter R_i, the bottom diameter R_b, and upper cone height H_u, thereby reducing the complexity of the optimization problem. Specifically, Ri was set to 0.8Rt, Rb was fixed at 0.1 mm and Hu was fixed at 0.25mm.

3.4.2 Assumptions for inverse analysis

The result of experiments for calibration is shown in the Fig. 36

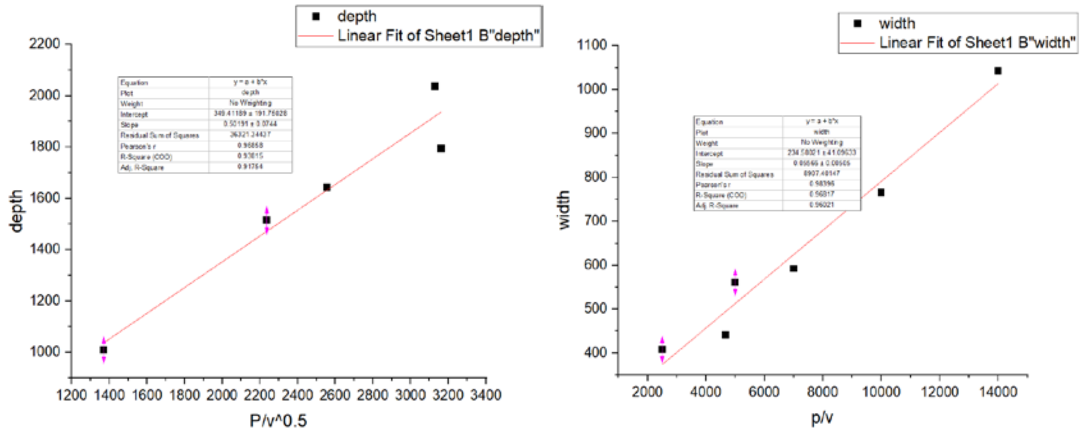

Fig. 36 Experimental results for calibration

Combined with the findings from the Pearson correlation analysis, which indicate that the molten pool width in the PINN model is highly correlated with the heat source top radius R_t, and the molten pool depth is highly correlated with the lower cone height H_l, we have reason to assume that $R_t$is linearly related to P/V, and H_l is linearly related to the scanning speed V. Based on these, the following two assumptions are proposed:

$$R_t(P,v) = m_1 \cdot \frac{P}{V} + n_1 (m_1, n_1 > 0)$$

$$H_l(P,v) = m_2 \cdot \frac{P}{\sqrt{V}} + n_2 (m_1, n_1 > 0)$$

3.4.3 Inverse analysis for calibration and validation

After each inverse analysis, the optimal heat source geometric parameters Rt_{opt} and Hl_{opt}, corresponding to the given process parameters P, V, are determined. Based on the optimized parameters obtained and according to the assumptions, R_t(P, V) and H_l(P, V) are fitted. This parameter set has the minimum loss in 240 optimization trials. The total time for the complete analysis of the all parameter sets are about 27 hours on an NVIDIA GeForce RTX 4090 GPU. The calibrated double-conical heat source parameters were obtained through inverse analysis, as shown in the Table 7.

Table 7 Calibrated geometric parameters for five evaluated process conditions. The top diameter Rt and lower cone height H_l vary with the laser power P and scan speed v according to: Rt=0.01928(P/V) + 128.08; Hl=0.505*(P/V^0.5) + 38.73.*

Parameter set	*P* W	*V* ms^{-1}	*Rt*	*Ri*	*Rb*	*Hu*	*Hl*
#1	750	0.3	176	141	0.1	0.25	730
#2	1000	0.1	321	257	0.1	0.25	1636
#3	1400	0.2	263	210	0.1	0.25	1620
#4	1250	0.2	249	199	0.1	0.25	1450
#5	1000	0.3	192	154	0.1	0.25	961

The calibrated parameter sets obtained through inverse analysis are input into the PINN model, which predicts the melt depth and melt width. The results of the calculations are presented in the Fig. 37. The mean relative error for the width prediction is 3.39%, with a standard deviation of 1.98%. For the depth prediction, the mean error is 4.47%, with a standard deviation of 0.65%. These error metrics indicate that the calibrated PINN model demonstrates strong performance in predicting both melt width and depth, with error values falling within an acceptable range.

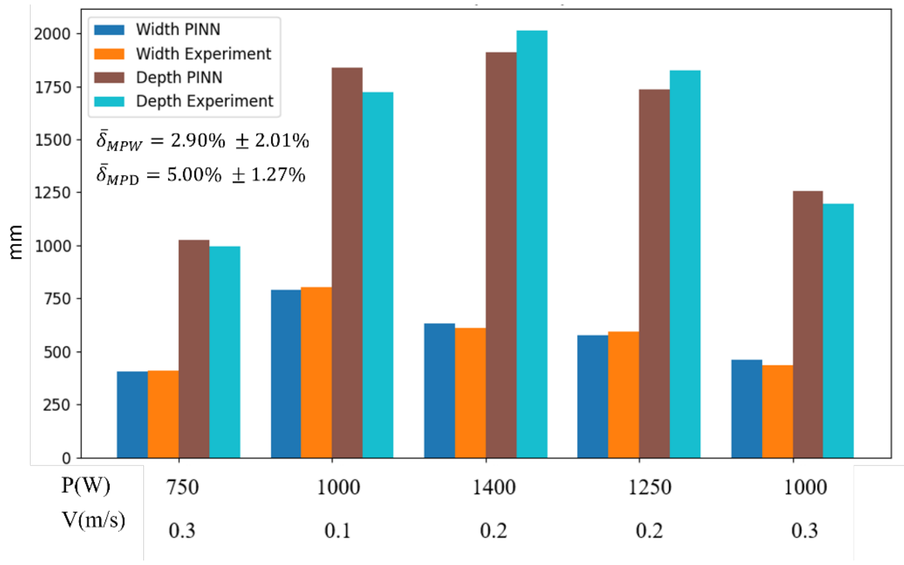

Fig. 37 Comparison between the melt pool dimensions predicted by the calibrated PINN model and the experimental measurements.

These findings confirm the reliability of the calibrated model and underscore the effectiveness of the PINNs model for integration into inverse analyses for rapid calibration of the thermal model across multiple PBF-LB process conditions within 30 h, whereas relying on traditional techniques such as FE analysis might take weeks or even months.

Consequently, a PINN-based model capable of predicting the temperature field and molten pool geometry solely as a function of the process parameters is established.

3.5 CFD Comparison

This section outlines the numerical framework employed as a benchmark for validating the PINN-based results. The commercial multiphysics software FLOW-3D WELD (Version 2025R1) was used to simulate the laser welding process. The software is based on the Volume of Fluid (VoF) method, treating the metal as an incompressible fluid with temperature-dependent properties. A scalar field, called volume fraction F, is computed, equal to the ratio of the volume occupied by the fluid to the total volume of the grid cell. The interface between the liquid metal and the surrounding air is accurately captured where $0 < F < 1$, allowing the dynamics of the keyhole and the weld bead dimensions to be resolved. The main models used in the simulations are: viscous flow, heat transfer and energy conservation, phase change with evaporation and solidification, volumetric thermal expansion, surface tension with Marangoni force, multiple laser reflections with Fresnel absorption, and gravity. Material properties and numerical parameters were selected in accordance with the validated setup used in a previous study [157]. By exploiting the symmetry of the laser weld bead with respect to the y-axis, only half of the full 3D domain shown in Fig. 25 was modeled in the software to reduce computational cost. The domain was discretized using two non-uniform nested structured Cartesian meshes. A refined mesh with 10 μm cell size was applied in the laser interaction zone to capture fine-scale phenomena, while a coarser thermal diffusion mesh with 40 μm cell size covered the remaining volume with a total number of cells of about 4 million. A fixed pressure boundary condition is imposed on the top surface while the others, except for the symmetric boundary, are defined as walls. The computational domain is shown in Fig. 38.

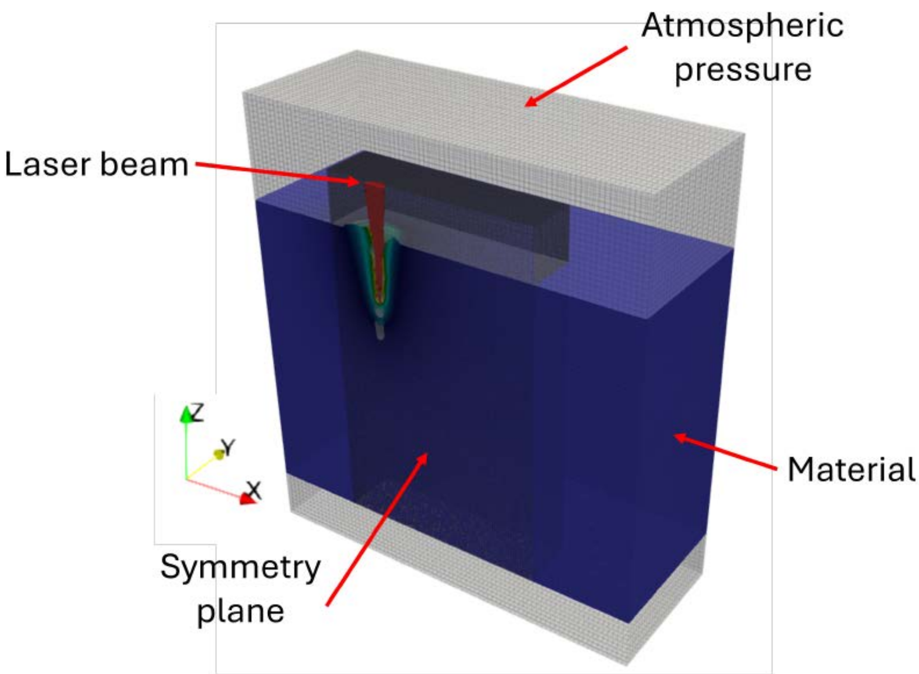

Fig. 38 Computational domain of the high-fidelity CFD simulations

The comparison between the simulated and bead-on-plate experimental is shown in Fig. 39a. The numerical model demonstrates good agreement with the experimental result, accurately predicting both the width and the depth of the melt pool. Since the simulation employs several models, starting with the fluid flow, it is also able to limitedly predict the superficial humping found in the process, not possible using the PINN model. Accordingly the FEM model was used to validate the tuned neural network using the temperature data from three virtual probes as illustrated in Fig. 39b. Specifically probes A and C were positioned near the locations corresponding to the maximum depth and width of the melt pool, respectively, while probe B was places 1 mm below the surface, within the melt pool. The comparison between the temperature measured by the CFD model and the calibrated PINN shows excellent agreement. Since the simulation does not explicitly model the vaporized material, no temperature data is collected when the middle probe (B) is located inside the keyhole region. face, within the melt pool.

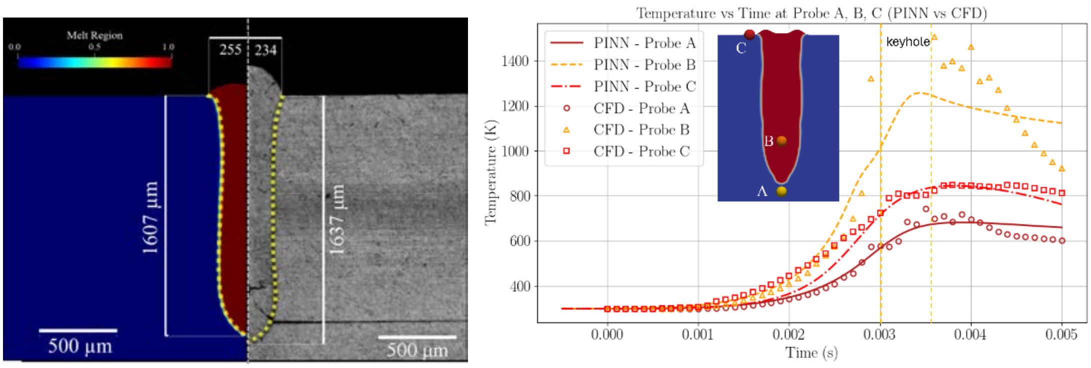

(a) (b)

Fig. 39 Simulations results used for PINN calibration. (a) Comparison between the FEM simulation and the experimental cross section. (b) Temperature trends of three probes for FEM and calibrated PINN

3.6 Case study

The predictive capability of the PINN model, previously validated with FEM simulations, demonstrated good agreement in both temperature field and molten pool dimensions. The PINN when ultimately applied to the case study. The 30 laser power-speed combinations of table 5 were used as model's inputs obtaining almost instantly both the penetration and melt pool width, which are plotted Fig. 40.

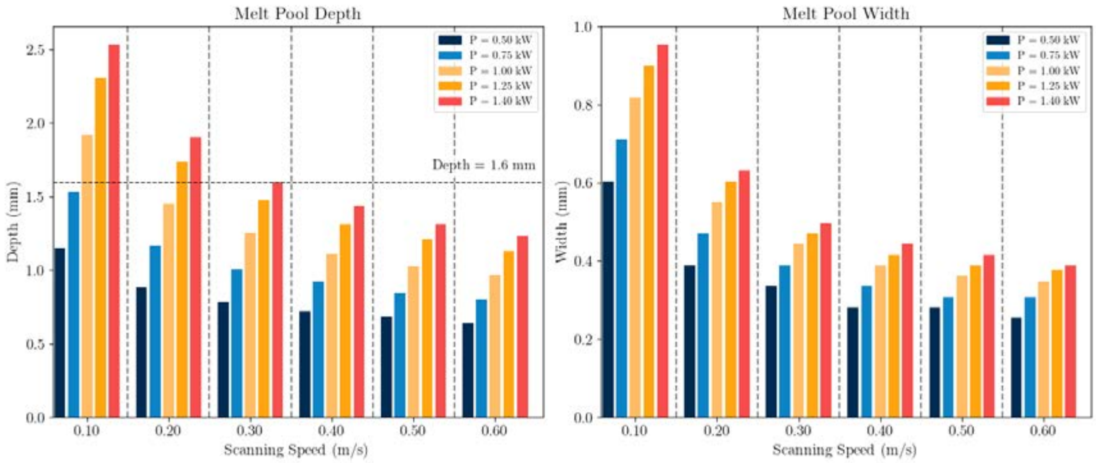

Fig. 40 Melt pool depth and width predictions for 30 candidate process cases obtained using the proposed PINN model.

Within the scanning speed range of 0.4–0.6 $m \cdot s^{-1}$, the predicted melt pool depths were below the required 1.6 mm threshold, thus failing to meet the need. At a scanning speed of 0.1 $m \cdot s^{-1}$, laser powers of 1 kW and above meet the molten pool depth requirement. At0.2 $m \cdot s^{-1}$, only 1.25 kW and 1.4 kW satisfy the requirement. At 0.3 $m \cdot s^{-1}$, the requirement is met solely at 1.4 kW. Based on this validation, three out of six parameter sets predicted by the PINN model to meet the target criteria were selected for trials:

• 1000 W 0.1 m·s−1

• 1400 W 0.1 m·s−1

• 1400 W 0.2 m·s−1

The resulting melt pool morphologies were compared with the corresponding PINN predictions, as illustrated in Fig. 41, and the relative errors in molten pool width and depth were also provided.

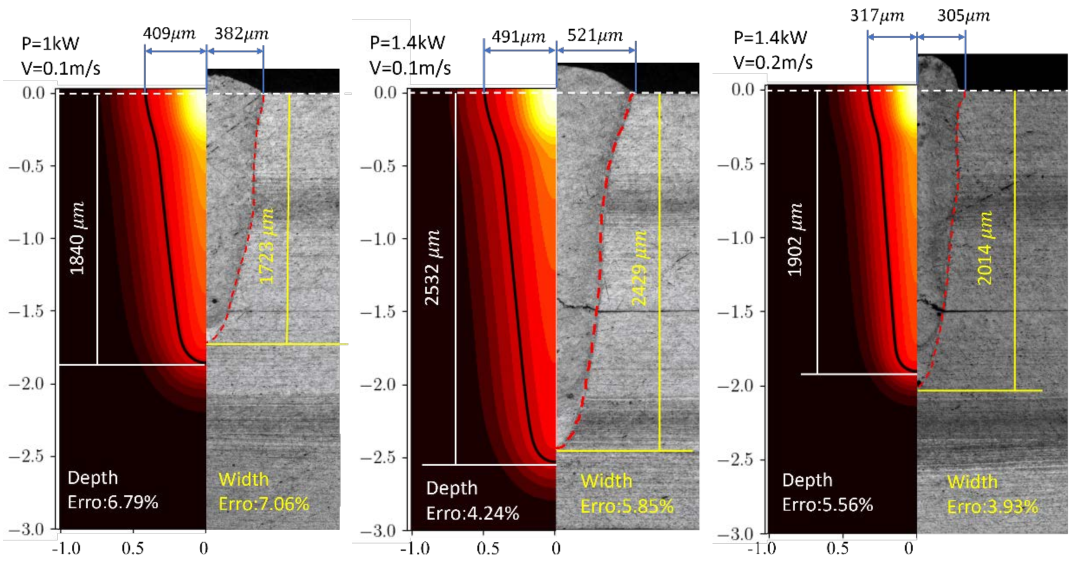

Fig. 41 Comparison between predicted melt pool size from PINN and experimental

The comparison between the PINN-predicted results and the experimental measurements demonstrates that the process parameter combinations selected in this constraint screening procedure for power-speed combination procedure successfully meet the predefined requirements, achieving molten pool depths greater than 1.6 mm, with prediction errors remaining within an acceptable range.

3.7 Chapter Summary

In this chapter, a comprehensive inverse analysis framework was developed to calibrate and validate the Physics-Informed Neural Network (PINN) model introduced in Chapter 2, thereby enabling its practical application to keyhole-mode LPBF processes. To achieve accurate temperature field prediction and melt pool geometry reconstruction, the double-conical volumetric heat source parameters were quantitatively correlated with laser power and scanning speed through a two-step strategy combining Pearson sensitivity analysis and inverse calibration.

Experimental bead-on-plate tests on aluminum alloy were performed to generate reference data for model calibration. The sensitivity analysis identified the lower cone height ($\boldsymbol{H_l}$) and top radius ($\boldsymbol{R_t}$) as the dominant parameters controlling melt pool depth and width, respectively. These key parameters were then expressed as empirical functions of process variables $P$and V, derived from inverse optimization using the L-BFGS algorithm. The calibrated PINN achieved millisecond-level prediction of melt pool geometry with mean relative errors below 5%, significantly outperforming traditional FEM-based calibration in computational efficiency.

Subsequent validation against experimental measurements confirmed the strong consistency of the calibrated model in both temperature evolution and molten pool morphology. Finally, the calibrated PINN was applied to a case study of overlap welding between two 1.5 mm aluminum plates, where it rapidly identified optimal power–speed combinations for achieving full penetration and stable melt pool. The results demonstrated the feasibility of PINN-based inverse analysis for fast, physics-consistent process optimization, establishing a solid foundation for real-time prediction and control in LPBF manufacturing.

Chapter 4: Post-Processing and Performance Enhancement

4.1Introduction

Following the process modelling and prediction work established in the previous chapter, this chapter focuses on the post-processing stage of Laser Powder Bed Fusion (LPBF) fabricated aluminium components. While process-level optimization ensures control over melt pool geometry and thermal history, the resulting microstructure and mechanical properties of the built parts are further governed by post-processing treatments that directly affect their surface integrity and structural integrity.

In LPBF-produced alloys such as Scalmalloy® (Al-Mg-Sc-Zr), the as-built condition typically exhibits process-induced defects including porosity, surface roughness, and residual tensile stresses, which can significantly reduce fatigue resistance and dimensional stability. To address these limitations, post-processing methods—such as machining, heat treatment, and surface severe plastic deformation (S2PD) techniques—are commonly employed to refine surface morphology, tailor residual stress distribution, and enhance the overall mechanical performance. Among these, shot peening (SP) and combined machining plus shot peening (M+SP) have shown promising potential in inducing beneficial compressive residual stresses without altering part geometry.

Therefore, this chapter systematically investigates the influence of different post-processing routes—machining (M), shot peening (SP), and machining followed by shot peening (M+SP)—on the surface and structural integrity of LPBF-fabricated Scalmalloy® components. Comprehensive analyses of microstructure, hardness, tensile strength, fatigue performance, and residual stress distribution are carried out to establish quantitative correlations between post-processing conditions and performance enhancement. The outcomes of this study provide an essential foundation for the multi-stage optimization framework of this thesis, bridging process-level thermal modelling with post-processing–driven property improvement.

4.2 Materials and Methods

4.2.1 Sample production and post processes

The Scalmalloy® powder used in this study is provided by Carpenter Additive®. The chemical composition of the Scalmalloy® powder, according to the supplier, is shown in Table 8. The nominal particle size is 20-63 µm. The MAM technology used in this studio is LPBF and the printing machine is a MYSINT100 (Sisma S.pa., Piovene Rocchette, Vicenza, Italy) equipped with a 200W Yb-fibre laser and a spot diameter of 50 µm.

Table 8. Chemical composition of Scalmalloy® powder.

Element		Mg	Sc	Mn	Zr	Fe	Si	Zn	Ti	Cu
Wt%	(min)	4.20	0.60	0.30	0.20	0	0	0	0	0
	(max)	5.10	0.88	0.80	0.50	0.40	0.40	0.25	0.15	0.10

All the samples were printed using the same LPBF process parameters. The print strategy and main process parameters was chosen based on the results of a preliminary experimental campaign carried out for density optimisation with final results of 99.6% and are summarised in Table 9.

Table 9. LPBF process parameters.

Laser power [W]	Scanning speed [mm/s]	Hatch distance [mm]	Layer thickness [mm]
170	600	0.17	0.02

A chessboard scanning strategy was used as shown in the Fig. 42, dividing each layer into 3x3 mm^2 square blocks. Blocks labelled with red were melted first, followed by those labelled green. Each adjacent formed layer was rotated 90° respect to the previous layer. Nitrogen (N_2) was used to fulfil the printing chamber with a residual oxygen content < 0.2% and the print was carried out without pre-heating of the platform.

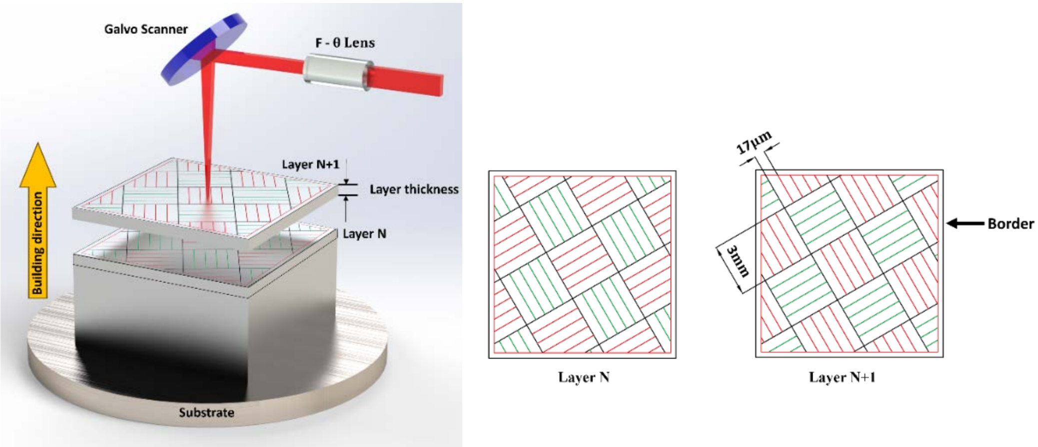

Fig. 42 Schematic of process in LPBF and scanning strategy.

Samples with three different geometries were manufactured with the dimensions shown in Fig. 43: a) 20 mm x 20 mm x 2 mm parallelepiped samples for the validation of the obtained density and surface integrity investigations (surface morphology, microstructure analysis, hardness tests and residual stress measurements); b) tensile samples (as defined by EN ISO 6892-1[158]) with a thickness 2 mm, and a 26 mm gauge length and c) rotating bending fatigue samples (as defined by EN ISO 1143:2010(E)[159][159]) with cylindrical section 6 mm in diameter and a 20 mm gauge length. Of each geometry, 27, 6 and 52 samples were printed, respectively.

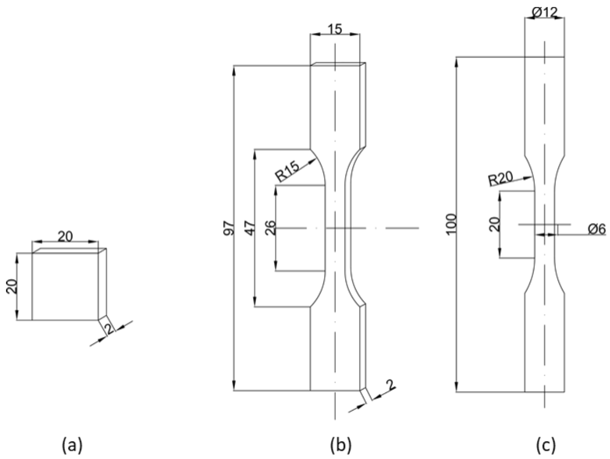

Fig. 43 Geometries of the samples: (a) parallelepiped sample, (b) tensile sample and (c) fatigue sample

After LPBF, the Scalmalloy® specimens were all heat-treated (HT), with the exception of 3 parallelepiped samples for residual stress analysis and 3 samples for tensile tests that were kept in as-built conditions for HT effects validation. The heat treatment was selected, according to the literature, between stress relief treatments[160] and can be summarised as follows: heating up to 325℃, maintaining for 4 hours and slow cooling inside the furnace. Their study demonstrated that a heat treatment at 325 °C for 4 hours, followed by slow furnace cooling, effectively relieves residual stresses while promoting the precipitation of $Al_3(Sc, Zr)$ particles, which contribute to microstructural stability and improved mechanical performance [161]. After HT the samples were divided into groups for subsequent post-processing. Parallelepiped samples were used for shot-peening (SP) optimisation as described in Fig. 44. SP was carried out using ceramic microbeads compliant with Industry Standards (NF L 06-824 and DS SP BE 01 Specifications) 1.2 mm in diameter. The grit flow was kept normal to the surface and the airstream pressure was varied from 2 to 6 bar at two different distances between the nozzle and the sample surface (15 mm, 150 mm) and two interaction times (20 s, 120 s). The selection of SP process parameters was out by surface integrity investigations (described in Section 4.2.2) and microhardness tests (Section 4.2.3.1). Tensile samples were then divided into 2 groups (HT and SP) and 3 of them were peened with the optimised process parameters. Finally, fatigue samples were separated into 3 groups (Fig. 44) with the following post-processes: HT + SP, HT + machining (M) and HT + M + SP. All the samples were post-processed after HT. The machining effect was considered by turning the fatigue samples with a 0.2 mm allowance.

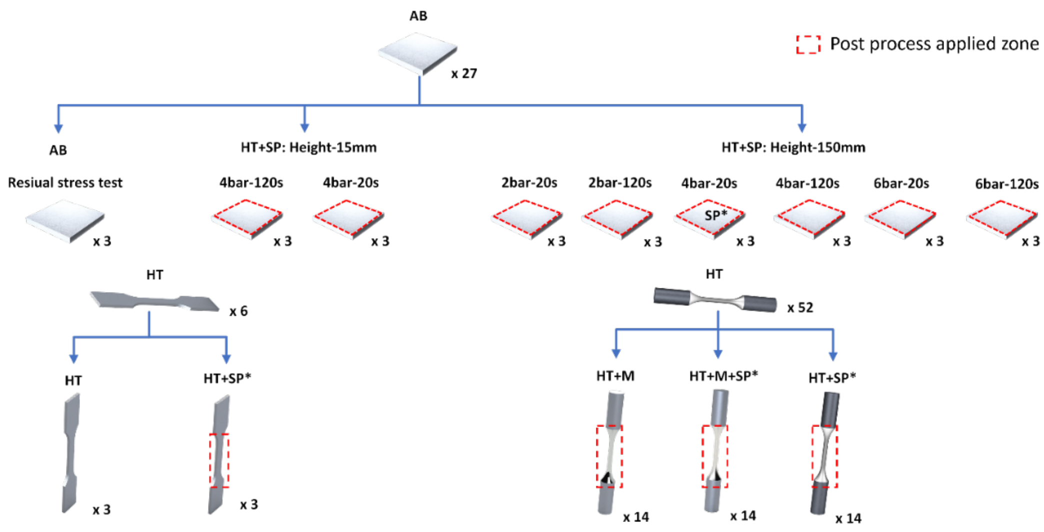

Fig. 44 Test flowchart.

4.2.2 Surface Integrity investigations

4.2.2.1 Surface morphology

Surface morphology images of the parallelepiped samples were obtained on a Keyence VHX-7000 digital microscope (Keyence Corporation, Osaka, Japan) at 100x magnification and using the “full coaxial” light source option for more accurate height measurement. Surface roughness parameters Sa and Sz were also derived from the same analysis using the associated software. 3 measurements in different positions were taken for each test condition on the parallelepiped samples and averaged for data comparison.

4.2.2.2 Superficial and sub-superficial analysis

The analyses of superficial integrity after SP were be assessed by cross-section observations of the parallelepiped samples. The samples were prepared by SiC paper up to a grit size of 2000 and polished by diamond suspension up to 1 μm, following the standard metallographic procedures. Etching solution with Keller’s reagent was used to reveal the differences in microstructure. The analyses included optical (OM, Nikon Optiphot-100), scanning electron microscopy (SEM, Zeiss EVO 50) and energy-dispersive X-ray spectroscopy (EDS Oxford Instruments acts-x) with electron backscatter diffraction.

4.2.2.3 Surface residual stress test

The surface residual stresses of the parallelepiped samples were measured using the MTS3000 RESTAN system by SINT Technology, following the semi-destructive approach of the hole-drilling method. In this technique, residual stresses were measured by incrementally drilling small diameter holes in the sample surface. A rosette-type B strain gauge was used, positioned precisely at the geometric center of the measurement surface. The drilled hole diameter was 1.8

mm while the diameter of the strain gauge circle (D) was 5.1mm. According to ASTM E837-20 standards [48], these parallelepiped samples are classified as "intermediate" workpieces, as their thickness (2mm) falls within 0.25D – 0.6D (1.3 – 3 mm). Moreover, "non-uniform" measurements of near-surface residual stresses were chosen, which means the residual stresses in the workpiece vary in the depth direction. For each test condition, the measurement was repeated on three different samples to ensure reproducibility.

As drilling progressed, each grid of the rosette recorded strains that correspond to the relaxation of residual stresses around the hole. Once drilling was complete, the actual diameter of the hole was measured to verify accuracy. Finally, the residual stresses were calculated from the recorded strain data using the most appropriate method for the analysis.

4.2.3 Structural Integrity analysis

4.2.3.1 Microhardness test

The microhardness of parallelepiped samples was performed from the surface to the 0.5 mm below the surface according to the EN ISO 6507 by using Vickers hardness tester (Leitz). The test set was as follows: the first 9 points were spaced at 50 microns, with depths ranging from 25 microns to 425 microns, and the last four points were spaced at 100 microns, with depths ranging from 525 microns to 925 microns. The Vickers hardness was calculated by measuring the indentation of the diamond on the sample surface. The results are reported in Vickers hardness (HV0.1) values. The mean values were calculated from three measurements per sample and at least three samples per condition.

4.2.3.2 Tensile tests

Quasi-static tensile tests were performed according to BS EN ISO 6892 on hydraulic testing machine (Italsigma, Forli, Italy) equipped with a 20 kN load cell. For tensile tests, the cross-head separation rate was kept constant at 0.17 mm/min, and the strain was measured by an extensometer with a gauge length equal to 20 mm. Only HT and SP samples were tested, while the M condition was not considered in this study, as previous findings indicated that machining has a slight impact on tensile properties[162].

4.2.3.3 Fatigue tests and fractographic analysis

Fatigue tests were carried out with the aim of determining the S-N curves in the finite life domain and the fatigue limit for infinite life (runout set at $2 \cdot 10^6$ cycles). Tests were run using a rotating bending machine (Italsigma, Forlì, Italy) at a loading frequency of 50 Hz and a load ratio of $R=-1$. The finite life domain was determined by three repetitions of the test at two different stress levels, which were provided in Table 10. Data for fatigue limit identification were processed by an abbreviated staircase method (ASM) enabling the estimation of fatigue limit with trials involving a reduced set of specimens proposed by Dixon and Massey[163]. The fatigue limits confidence bands at the 56% confidence level were determined based on the failure-not-failure sequences, involving 6 to 8 nominal samples. Fractographic analysis was carried out on the fracture surface of fatigue samples by SEM.

Table 10 Stress level for finite life

	SP	M	SP+M
σ1 [MPa]	150	150	160
σ2 [MPa]	138	138	150

4.3 Results and discussions

4.3.1 Scalmalloy properties

The mechanical characteristics of Scalmalloy HT samples were established for reference prior to the experimental campaign that was described. The results of tests for tensile strength, residual stress, and microhardness are presented here. Vickers microhardness measurements along the sample thickness reveal homogeneous properties with a mean value equal to 203.8 HV and a standard deviation of 2.4. This low variability is also confirmed by residual stress analysis. Fig. 45 shows the residual stress distribution of samples in-depth direction in AB and HT conditions. In AB samples, tensile residual stress is measured on the surface and compressive stress underneath 0.4 mm, as expected. In contrast, the heat-treated samples show a nearly uniform, near-zero value with very low variability, so the effectiveness of the heat treatment was confirmed.

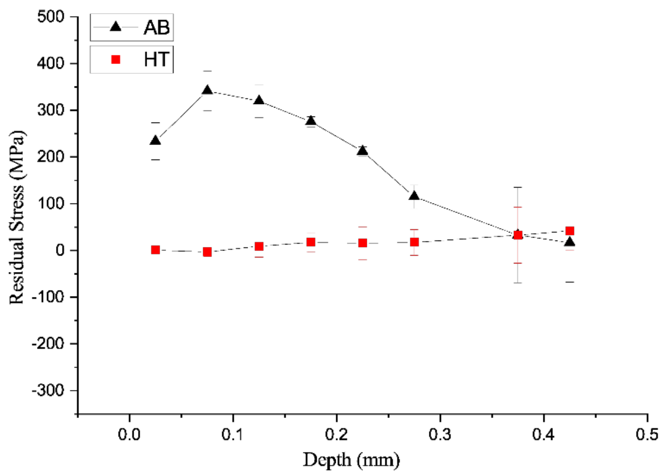

Fig. 45 Residual stress measurement in As-built (AB) and heat-treated (HT) conditions. Error bars represent the standard deviation (SD)

Finally, tensile tests were performed and a representative engineering stress-strain curve is presented in Fig. 46. The HT samples achieve a mean UTS of 465 MPa, a yield strength (YS) of 437 MPa, and an elongation (E) of 12.2%.

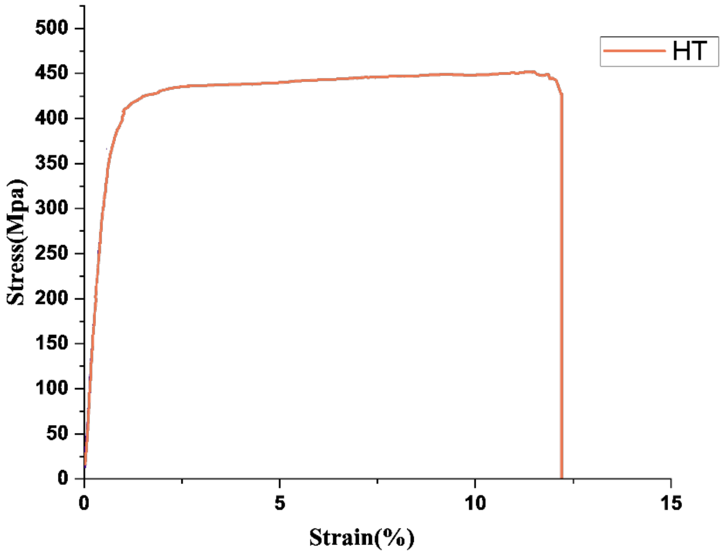

Fig. 46 Tensile test result.

4.3.2 SP optimization

4.3.2.1 Surface morphology and roughness

Parallelepiped samples were used to optimized the SP parameters. When the peening distance was set to 150 mm, the entire surface was treated, whereas at a distance of 15 mm, only a circular region with a diameter of 1 mm located at the geometric centre of the square surface was peened.

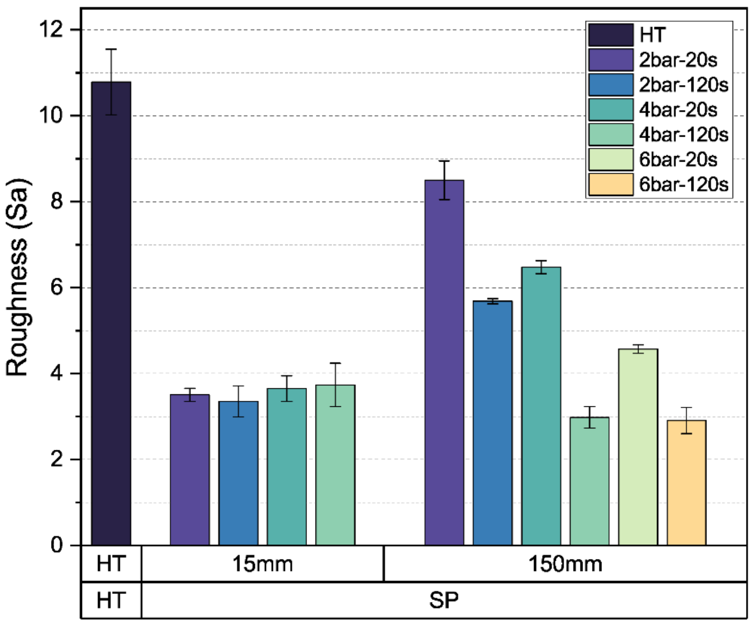

Fig. 47 Effect of peening distance and pressure on surface roughness (Sa) of Scalmalloy parallelepiped samples. Error bars represent SD

As shown in Fig. 47,, setting the peening distance to 15 mm results in a significant reduction in surface roughness without a significant effect of exposure time and pressure in the range between 2 and 4 bar. Specifically, Sa values decrease to 3.4 μm and 3.7 μm at 2 and 4 bar, respectively, with negligible differences between 20 and 120 seconds of exposure. This corresponds to a 65% reduction compared to the reference condition (HT), which initially exhibits a mean Sa of 10.8 μm. The improvement is primarily due to the high density of microbead impacts per unit area at short distances, which enhances surface plastic deformation and rapidly removes loosely adhered powder particles. As a result, surface smoothing is rapidly achieved, and further extending the exposure time has a negligible effect on roughness reduction. However, increasing the pressure further to 6 bar at this short distance leads to surface degradation, likely due to excessive plastic deformation and crater formation, so roughness measurements were not performed.

At a longer peening distance of 150 mm, surface roughness becomes more sensitive to both pressure and exposure time. In particular, Sa values decrease from 8.5 μm to 4.6 μm (~ -50%) as pressure increases from 2 to 6 bar at short exposure time (20 s). As the exposure time increases from 20 to 120 seconds, the surface roughness decreases from 5.7 μm to 3 μm (~ -47%) at a pressure of 4 bar. Beyond this point, further increasing the pressure from 4 bar to 6 bar has no significant effect on the roughness. These results indicate that, at longer peening distances (150 mm), the shot stream covers the entire surface uniformly, but the number of impacts per unit area is lower compared to short distances. As a result, within a short exposure time (20 s), surface defects such as adhered powder particles may not be completely eliminated. In this context, increasing the exposure time up to 120 s enhances the cumulative impact effect, allowing more effective defect removal and improved surface smoothing. Similarly, higher peening pressure increases the impact energy, which promotes plastic deformation and facilitates the removal of surface irregularities, leading to a further reduction in surface roughness.

Interestingly, when comparing long- and short-distance SP at equal pressure (4 bar) and exposure time (120 s), long-distance peening results in smoother surfaces (Sa = 3.0 μm at 150 mm vs. 3.7 μm at 15 mm). This is attributed to the more uniform energy distribution at longer distances, which reduces the risk of forming spherical craters that otherwise slightly increase roughness in short-distance treatments.

Fig. 48 shows the surface morphology images from different SP conditions in comparison to the reference component (HT). In HT conditions (Fig. 48a), unmelted and partially melted powder particles are firmly adhered to the solidified surface and distributed non-uniformly. After SP (Fig. 48b–d), the surfaces appear macroscopically smoother. Particularly in conditions (c) and (d), all powder residues are effectively removed. However, as the pressure increases and distance decreases (Fig. 7d), ball-shaped grooves appear, confirming the onset of localized over-peening effects.

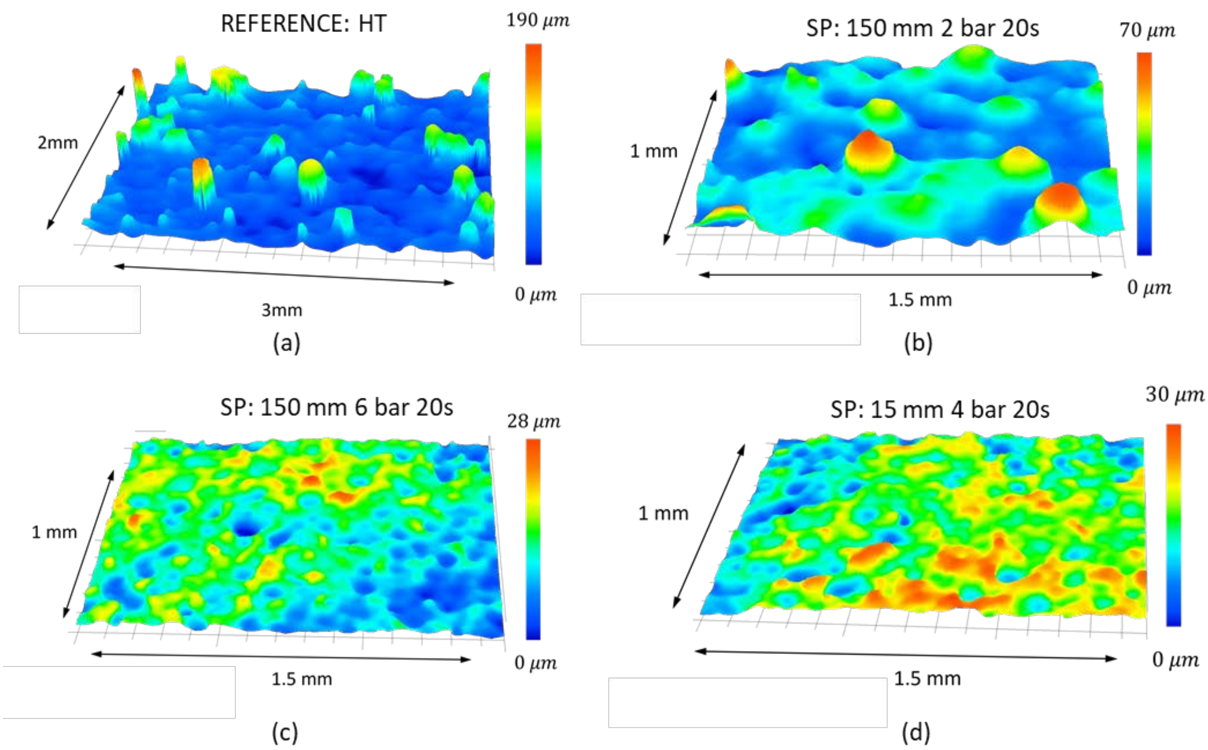

Fig. 48 Confocal microscope images of the shot peening surface under different conditions: (a) reference condition, (b) SP performed at 150 mm with 2 bar and 20s, (c) SP performed at 150 mm with 6 bar and 20s and (d) SP performed at 15 mm with 4 bar and 20s

4.3.2.2 Microhardness tests

The Vickers microhardness profiles from the surface up to 450 μm in depth under different SP conditions are shown in Fig. 49. These results confirm some of the assumptions discussed in the previous section, particularly regarding the effects of peening distance and pressure on surface modification. At a peening distance of 15 mm, a significant hardness increase with respect to the HT reference is observed in the near-surface region, extending up to a depth of approximately 130 μm. Along this depth, the hardness is highest near the surface and progressively decreases with depth. The maximum hardness measured at the 15 mm condition is 277 HV, under the 4 bar, 120 s condition, representing a 37.8% increase over the HT value. Beyond a depth of ~220 μm, the hardness stabilizes at around 210 HV, which is still ~5% higher than the unpeened condition.

At the longer peening distance of 150 mm, the same trend of increasing hardness with pressure and exposure time was observed, and the highest hardness measured was registered after 120 s at 6 bar, which was ~248 HV, corresponding to a 23.5% increase over the HT condition. Notably, this is significantly lower than the maximum achieved at 15 mm, confirming the effect of a lower energy density in the shot stream at longer distances. This observation is consistent with the lower number of impacts per unit area, as previously discussed. Moreover, the reduced impact severity at 150 mm is also reflected in the overall hardness profiles, which become closer to the reference values at depths of 130 μm.

In all cases, the increased surface hardness observed after SP can be primarily attributed to microstructural changes induced by severe plastic deformation. The surface region of the Al alloy develops a gradient structure characterized by high dislocation density, stacking faults, and the formation of low-angle grain boundaries[164][165].

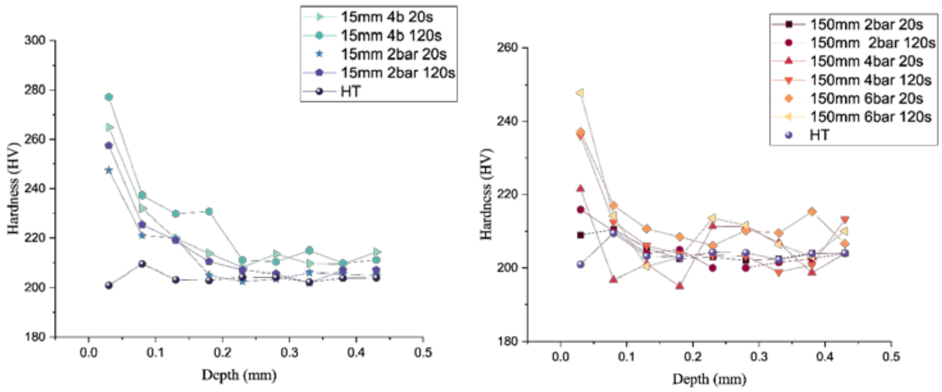

Fig. 49 Hardness distribution to a depth of 450 microns

4.3.2.3 Residual Stress

To quantify the effect of peening on sub-surface residual stresses, some of the previously tested conditions were selected for hole drilling tests. The results are shown in Fig. 50 and Table 4 and compared to the reference condition after HT.

Using a peening distance of 150 mm that guarantees the treatment all over the surface, the residual stress just below the surface varies in a range of - 60 – -273 MPa. In detail, the combination of lower interaction time (20 s) and lower pressure (4 bar) corresponds to a slight effect with respect to the starting condition (from 0 to -60 MPa). From this result, an increase of interaction time from 20 s to 120 s leads to a relevant improvement of the peening effect and the minimum residual stress registered below the surface is 137 MPa. An increase of peening pressure from 4 bar to 6 bar results in a further reduction in the residual stress close to the surface (-273 MPa). However, the thickness over which this strong reduction was observed was limited, as the stresses rapidly increased to 0 MPa after just 180 µm.

Table 11 summarises these results by comparing the maximum observed compressive residual stress CRS and the depth at which it was measured. After 120 s and 6 bar the maximum CRS reached –273MPa (59% of the UTS) at a depth of 25 µm, while at 4 bar, a maximum CRS of –182 MPa (39% of UTS) was reached at 75 µm with positive values measured up to 325 µm.

According to the literature[166], specimens subjected to higher-intensity shot peening undergo more severe surface deformation and generate a greater number of dislocations on the surface. Thus, the absorbed elastic-stored energy and plastic deformation energy lead to higher CRS, and the near-surface residual stress distribution observed in this study is consistent with this conclusion. Meanwhile, with increasing peening intensity, the specimen is expected to exhibit a deeper compressive residual stress distribution and a greater Influence Depth of CRS. However, under the peening condition of 150 mm and 120 s, when the peening pressure increased from 4 bar to 6 bar, the maximum residual stress appeared near the surface, and the affected depth of residual stress decreased from 325 µm to 125 µm. This phenomenon may be attributed to exogenous defects such as folded cracks induced by excessive pressure or the presence of endogenous defects (i.e voids clusters and linear cracks) which could lead to the release of accumulated energy, thereby affecting the overall distribution of residual stress[167].

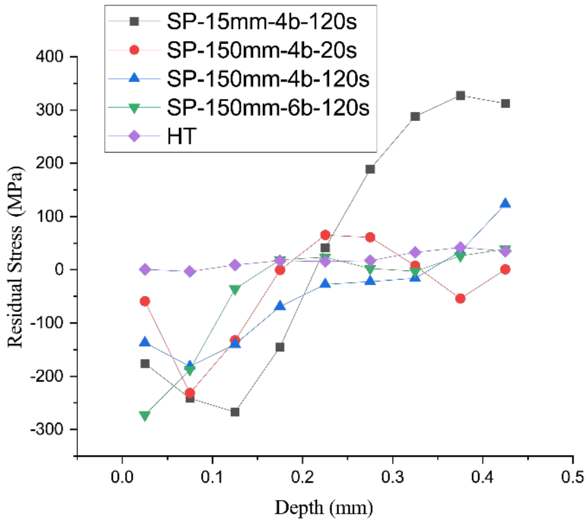

Fig. 50 Residual stress measurement comparison between different SP conditions.

Table 11 Residual stress distribution

SP treatment	Max CRS (MPa) / Percentage of the UTS [%]	Depth of max CRS [μm]	Influence Depth of CRS [μm]
15mm-4bar-120s	-267 $\pm$ 12/57	125 $\pm$ 9	175$\pm$ 9
150mm-4bar-20s	-231$\pm$ 9/50	75$\pm$ 3	175$\pm$ 5
150mm-4bar-120s	-182$\pm$ 8/39	75$\pm$ 6	325$\pm$ 14
150mm-6bar-120s	-273$\pm$ 11/59	25$\pm$ 2	125$\pm$ 6

4.3.2.4 Microstructure and defects

At a peening distance of 150 mm and a pressure of 4 bar for 20 seconds, the larger adhered powders are removed, but small dark voids, approximately 10 microns in size, appears on the shallow surface (Fig. 51a). Their sizes are consistently 10 microns. When the pressure is increased to 6 bar, these dark voids expand to over 20 microns, likely contributing to surface damage (Fig. 51b). Under the condition of a 15 mm peening height and pressure of 4 bar, the damage is even more pronounced, with distinct circular pits caused by the peening media clearly visible (Fig. 51c). Furthermore, the morphology reveals that one of the two scanned contour layers are removed, leading to an increase in surface roughness, consistent with the roughness measurements. Additionally, ceramic chips are observed embedded in the surface of the workpiece, appearing as the white spots in Fig. 51(c).

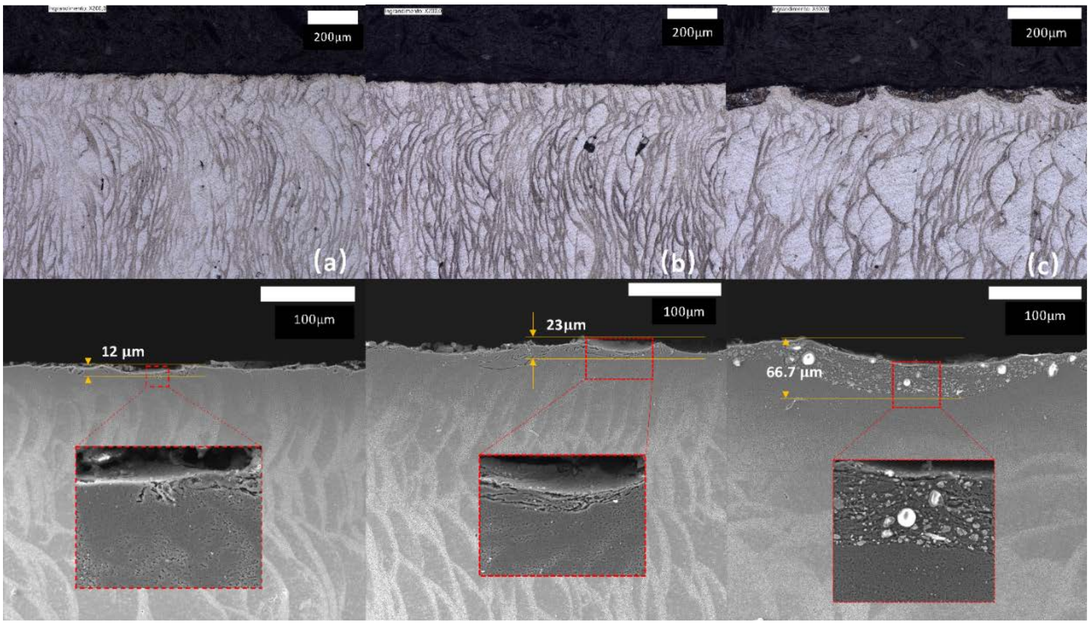

(a)150mm 4bar 20s *(b)150mm 6bar 20s* *(c)15mm 4abr 120s*

Fig. 51 SEM and Optical microscope images of the workpiece surface layer.

Combining the results of surface roughness and residual stress on parallelepiped samples, we selected a set of SP parameters that would result in sufficient residual stress while minimizing damage, which is 150mm height with 4bar pressure and 20s duration peening. With this SP parameter, printed samples exhibit a maximum CRS of 231Mpa (50% of UTS) and less surface damage depth. In this case, although the surface roughness is higher compared to the 150mm 4bar 120 s shot peening condition, surface morphology images indicate that major surface defects, such as adhered unmelted particles, are effectively removed. In addition, this condition avoids the additional surface damage typically associated with excessive peening pressure while still introducing sufficiently high compressive residual stress in the near-surface region.

4.3.3 Post-processes comparison

4.3.3.1 Surface integrity results

Fig. 52 presents SEM images of the surface morphology of fatigue specimens subjected to different post-processing conditions. In general, no remaining powder particles are visible following these surface post-treatments, confirming the effectiveness of both turning and shot peening in removing adhered unmelted particles from the LPBF surface. The turned surface appears smooth and exhibits a typical kinematic roughness pattern generated by the controlled tool path during machining. In contrast, surfaces subjected to shot peening—both directly (SP) and following machining (M+SP)—display clearly visible craters formed by the high-speed impact of ceramic microbeads that result in localized plastic deformation.

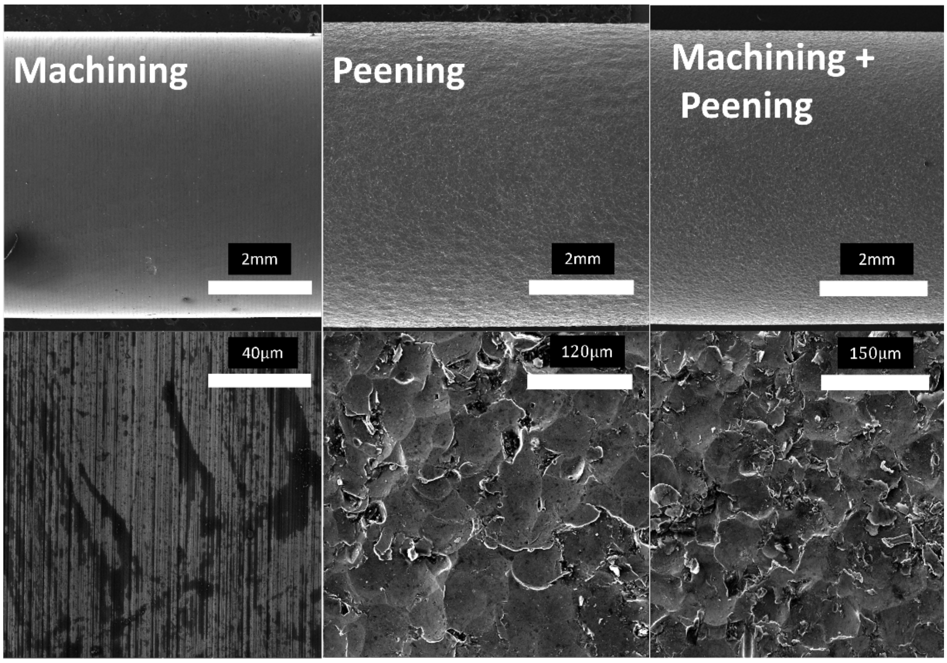

Fig. 52 SEM surface images of fatigue samples in different conditions Machined (M), Shot Peening (SP) and Machined + Shot peening (M+SP).

The roughness of fatigue samples after different post-processing methods is presented in Table 12. The average roughness values obtained after shot peening are consistent with those observed on planar specimens (), confirming the reproducibility of the process. As expected, turning leads to the most pronounced reduction in roughness due to the removal of the characteristic LPBF surface morphology, including partially fused particles, sharp asperities, and inter-layer valleys. The application of shot peening after machining (M+SP) results in a lower surface roughness compared to SP samples. As mentioned, the turning process removes the inherent irregularities of the LPBF surface, producing a smoother and more uniform substrate. As a result, in M+SP, the final roughness more directly reflects the intrinsic contribution of the shot peening process itself, isolating its effect from that of the LPBF-induced topography. Although the morphology remains similar in both SP and M+SP cases, the amplitude of the surface features—specifically the peak-to-valley height—is significantly reduced in the M+SP condition, leading to a lower average roughness (Ra). This is confirmed by the observation that the M+SP specimens, despite exhibiting a higher Ra than the M sample, show a comparable Rz value. This indicates that the maximum height between peaks and valleys is similar in both cases.

Table 12 Roughness of the fatigue samples after different post processes

Post process	Ra (μm)	Rz (μm)

M+SP	6.2	24.1
SP	9.1	45.4
M	3.9	20.2
HT (reference)	11.8	57.3

4.3.3.2 Structural Integrity results

Starting with previous results in terms of surface integrity properties and the effect of SP, the structural integrity of Scalmalloy components in different conditions was finally analysed as the main goal of this paper. The fatigue test results after the final selected conditions are illustrated in Fig. 53, which includes the S-N curves for specimens in the SP condition, the M condition, and the combined M+SP condition. The data points represent experimental results, while the lines indicate the S-N curves fitted to these results. The horizontal line represents the fatigue limit determined using the ASM method, which estimates the fatigue limit based on a limited number of trials.

The strength level of the samples with M+SP is 10 MPa higher than that in SP condition. Since the machining of the specimens took place after the heat treatments, it can be assumed that these specimens were stress-free before machining. Machining usually introduces low residual compressive stresses into the specimens, so it is possible to suppose that the fatigue limit increasing from SP to M+SP is due to the surface integrity of the samples. On the other hand, the fatigue limit of samples in the SP condition is 42 MPa higher than that in the M condition. As demonstrated before, the topography of the samples after peening is slightly damaged, so the beneficial contribution in fatigue limit is connected to the high compressive residual stress induced by this process.

Looking at the results as a whole, it is possible to summarize that the contribution of SP is the most relevant, despite the slight surface damage detected by the microstructural analyses. Machining on the other hand, contributes to a lesser extent. By analyzing roughness and residual stress data, these contributions can be partially quantified. The reduction in roughness, which goes from 9.1 to 6.2 (i.e., a difference of roughly 3 microns), is the only variable in the data obtained when comparing the SP and M+SP conditions. This decrease ensures an 8% improvement in fatigue performance. When the M and SP conditions are compared, the roughness difference of roughly 5 microns favours the M condition, but the fatigue life of the SP condition increases by 45%. Because roughness has a negative impact on the mechanical integrity results, this could indicate that the positive contribution of compressive stresses is higher than 45%. Based on the difference between SP and M+SP, it is possible to estimate the weight of this negative effect to be between 8 and 15%. This suggests that the contribution of residual stresses, independent of the effect of roughness, is worth roughly +55 to 60%.

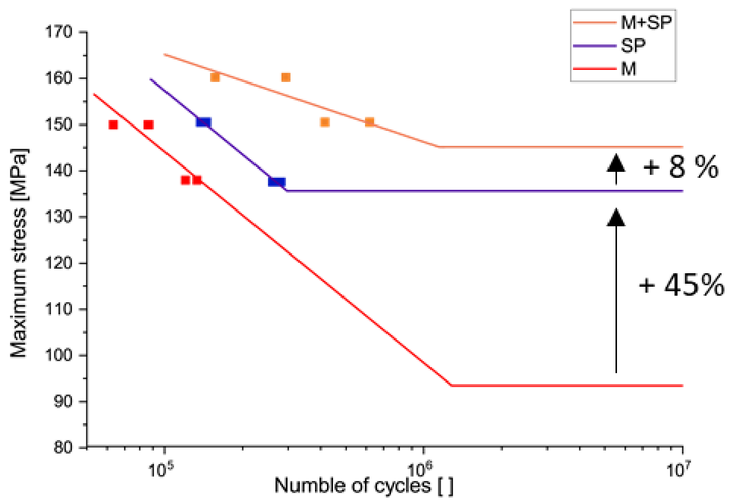

Fig. 53 Fatigue test result.

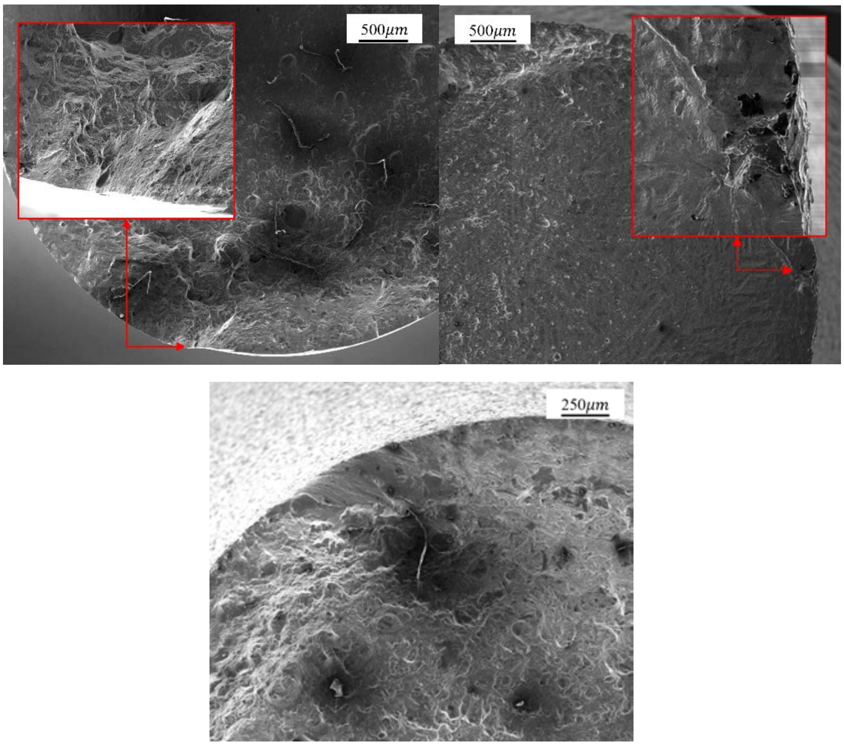

(a)M *(b)SP* *(c)M+SP*

Fig. 54 SEM fracture surfaces images of fatigue samples in different conditions Machined (M), Shot Peening (SP) and Machined + Shot peening (M+SP).

In the end, Fig. 54 illustrates the fracture surface of fatigue samples. In Fig. 54(a), the crack originates from a pore defect located near the surface. While in SP condition (b), the initial point is the porosity at superficial layer. In the M+SP condition, no obvious crack initiation points are observed, this may indicate the crack initiation from volumetric defects to surface initiation in the absence of a relatively large defect in the vicinity of the surface.

4.4 Chapter Summary

From the previous investigation, by comparing the effects of different post processes on the surface and strucural integrity of LPBF Scalmalloy® additive manufactured specimens, some conclusions can be drawn as follows:

- Shot peening can influence hardness up to a depth of 200 μm below the surface, with the maximum hardness observed at the surface of the samples. The overall hardness may also be affected by the specimen's thickness, especially when high-intensity shot peening is applied (15 mm height, 6 bar).
- The surface roughness initially decreases and then increases as the shot peening time increases. Once the shot peening duration is sufficiently long, the impact of peening pressure on roughness becomes less significant.
- Shot peening effectively removes most of the attached surface powders but can also create varying degrees of surface depressions. High-intensity shot peening (15mm, 6 bar) can cause surface damage and embed ceramic chips into the workpiece. However, the impact of these embedded particles on the component's properties has yet to be confirmed.
- Residual stress due to shot peening can reach to a depth of 300 μm below the surface. The impact depth varying based on the intensity of the shot peening. Low-intensity shot peening (150mm 4bar 20s) can bring favourable residual stress effect while causing less damage to the workpiece surface.
- After shot peening, due to the induced residual stress, fatigue strength increased in most cases. Fatigue strength of the 3 surface modifications followed this order: HT+M < HT+SP < HT+M+SP.
- The contribution of residual stresses to the improvement of fatigue life is the most relevant, which is independent of the effect of roughness, +55 to 60%.

Chapter 5 Conclusions and Outlook

5.1. Content and conclusions

This dissertation conducted a systematic study covering process modelling, model calibration and validation, and post-processing integrity optimization, aiming to address the challenges of high computational cost, limited physical interpretability, and insufficient real-time adaptability in Laser Powder Bed Fusion (LPBF).Through the consistent use of Physics-Informed Neural Networks (PINNs), the research established a progressive workflow from physics-constrained temperature field modelling to inverse parameter calibration and finally to post-processing performance evaluation, achieving both computational efficiency and physical consistency. In the final stage, the methodology was extended to the experimental evaluation of LPBF-fabricated Scalmalloy® components, where different post-processing routes—machining (M), shot peening (SP), and combined (M+SP)—were systematically compared to clarify their influence on surface integrity, residual stress, and mechanical performance, providing practical insights for performance enhancement and integrity optimization in LPBF alloys.

In Chapter 2, A Physics-Informed Neural Network (PINN) framework was developed to model transient heat transfer in the keyhole-mode LPBF process by embedding the Fourier–Kirchhoff heat conduction equation and boundary conditions into the network loss function. A double-conical volumetric heat source was introduced to capture the deep-penetration energy distribution with high physical fidelity and geometric flexibility. Through adopt systematic optimization of network architecture (8 layers, 32 neurons per layer), sin activation function, and moving-center collocation sampling, the PINN achieved stable convergence and physics-consistent temperature field reconstruction without requiring experimental data. Compared with CFD and FEM simulations, the proposed PINN framework demonstrated comparable accuracy with a computational efficiency several orders of magnitude higher, providing a robust and scalable foundation for real-time thermal prediction and process control in LPBF.

In Chapter 3, the trained PINN was calibrated and validated through inverse analysis. With inverse analysis, the study identified the key volumetric heat source parameters governing the melt pool geometry and established empirical mappings between these parameters and laser process conditions (power and scanning speed). After calibration, the model could instantly predict melt pool dimensions and temperature fields with mean relative errors below 5%. A case study on overlap welding of two 1.5 mm aluminum plates further demonstrated the capability of the calibrated PINN for rapid process optimization ($<$50ms), Accurately and quickly find the power-speed combination to achieve the target penetration depth, validated through experiments comparisons, the average error is within 7%.

In Chapter 4, Systematic post-processing experiments on LPBF-fabricated Scalmalloy® components revealed the effects of machining, shot peening, and their combination on surface integrity, residual stress, and fatigue behavior. Shot peening induced a hardness enhancement extending up to ~200 μm below the surface and compressive residual stresses reaching depths of ~300 μm, with low-intensity conditions (150 mm, 4 bar, 20 s) providing the most favorable balance between surface preservation and stress induction. While prolonged or high-intensity peening (15 mm, 6 bar) led to surface depressions and embedded particles, moderate treatments effectively refined the surface and improved structural stability. Fatigue performance improved consistently with the presence of compressive residual stress, following the trend HT + M < HT + SP < HT + M + SP, where combined machining and shot peening yielded up to a 55–60% increase in fatigue life. These findings highlight the dominant role of residual stress over surface roughness in governing fatigue behavior and provide a practical framework for optimizing post-processing parameters to enhance the mechanical integrity of LPBF Scalmalloy® components.

5.2. Contributions and Innovations

The main innovations of this work can be summarized as follows:

(1) An efficient Physics-Informed Neural Network (PINN) framework integrating physical constraints with deep learning was developed for transient heat transfer modelling in the keyhole-mode LPBF process. By explicitly embedding the Fourier–Kirchhoff heat conduction equation and boundary conditions into the network loss function, the model achieved high-accuracy temperature field reconstruction under unsupervised, data-free conditions. Meanwhile, a double-conical volumetric heat source model was introduced to capture the deep-melt energy distribution, featuring geometric tunability and cross-mode scalability. This framework demonstrates superior computational efficiency, physical consistency, and interpretability compared with traditional numerical methods, providing a novel physics-driven learning paradigm for rapid prediction and real-time control of the LPBF process.

(2) Inverse calibration and data-efficient process optimization: Through inverse analysis integrated with experimental validation, the study established explicit mappings between laser parameters and volumetric heat source geometry, enabling instant prediction of melt pool morphology with less than 5% error. The calibrated PINN demonstrated strong capability in optimizing process parameters for stable and fully penetrated welds, achieving rapidly prediction (<50 ms) under varying conditions. This demonstrates its potential for future application in LPBF real-time monitoring systems.

(3) The investigations of the post-processing behavior of LPBF-fabricated Scalmalloy® components: By systematically comparing machining (M), shot peening (SP), and combined

(M+SP) treatments, this study elucidated the coupling mechanisms among surface integrity, residual stress, and fatigue performance, thereby refining the understanding of Scalmalloy® strengthening behavior and providing practical guidance for future post-processing optimization and surface enhancement design.

5.3. Future Work

Building upon the results of this dissertation, several research directions can be pursued:

(1) Integration with real-time monitoring and closed-loop control

The next step is to couple the PINN-based thermal model with in-situ sensing data (e.g., infrared imaging, melt pool sensors) for adaptive parameter adjustment and real-time defect mitigation during LPBF fabrication.

(2) Extension to multi-physics and multi-scale coupling

Future models can incorporate additional physical phenomena such as melt flow, vapor recoil, and solidification kinetics to predict microstructural evolution and residual stresses within a unified PINN framework.

(3) Generalization across materials and process platforms

The calibrated model can be extended to other alloy systems (e.g., Ti6Al4V, Inconel 718) and manufacturing setups by retraining or transfer learning, improving its robustness and general applicability.

Acknowledgements

The completion of this dissertation would not have been possible without the guidance, assistance, and support of many professors, colleagues, friends, and family members. I would like to express my deepest gratitude to all those who have cared for and supported me throughout my academic journey and personal life.

First and foremost, I would like to express my sincere appreciation to Professor Alessandro Fortunato, my supervisor, for his dedicated guidance and unwavering support throughout my doctoral research. His profound knowledge, rigorous academic attitude, and scientific approach have greatly inspired me. His encouragement and recognition of my research ambitions have been a constant source of motivation.

My heartfelt thanks also go to my co-supervisor, Professor Erica Liverani, for her invaluable advice and encouragement in developing research ideas, structuring this dissertation, and engaging in academic discussions. From topic selection to methodological refinement and writing, her high academic standards and thoughtful guidance have continuously motivated me to improve my work.

I would like to express my sincere gratitude to the China Scholarship Council (CSC) for its financial support, which gave me the I have had the opportunity to go further and further on my professional path.

Special thanks are extended to the Laser Group and DIN Department for their invaluable technical support and experimental assistance. Their expertise provided a solid foundation for the completion of this work.

I am also deeply grateful to my colleagues and friends who have accompanied me throughout my Ph.D. journey. My thanks go to Prof. Alessandro Ascari for his cheerful laughter that has always brightened my days, Hambal for his guidance when I first arrived this group, Lorenzo for introducing me to Italian culture, Caterina and Michele for their careful assistance and encouragement, Samuele for his reliable collaboration, and Chiara for her generous help. Your companionship, discussions, and encouragement have brought warmth and motivation to the long and challenging path of research.

Finally, my deepest gratitude goes to my family. I thank my parents for their unconditional love and understanding, and Ding Xinran for her companionship during my three years in Italy, and Sun Lei for always believing in me and providing strength.

I dedicate this work to all those who have offered me guidance, inspiration, and support throughout this journey.

Reference

[1].Farshidianfar, Mohammad H., Amir Khajepour, and Adrian Gerlich. "Real-time control of microstructure in laser additive manufacturing." *The International Journal of Advanced Manufacturing Technology* 82.5 (2016): 1173-1186.

[2].Khodabakhshi, F., et al. "Effects of laser additive manufacturing on microstructure and crystallographic texture of austenitic and martensitic stainless steels." *Additive Manufacturing* 31 (2020): 100915.

[3].Wei, Chao, and Lin Li. "Recent progress and scientific challenges in multi-material additive manufacturing via laser-based powder bed fusion." *Virtual and Physical Prototyping* 16.3 (2021): 347-371.

[4].Li, Lin, W. U. H. Syed, and A. J. Pinkerton. "Rapid additive manufacturing of functionally graded structures using simultaneous wire and powder laser deposition." Virtual and Physical Prototyping 1.4 (2006): 217-225.

[5].Sobhanieh, Niloufar, Javad Akbari, and Mahmoud Moradi. "A new method for calculating laser intensity distribution on workpiece surface in laser-directed energy deposition process by considering powder stream distribution and laser attenuation." *The International Journal of Advanced Manufacturing Technology* 121.1 (2022): 337-348.

[6].Farshidianfar, M. H., et al. "Laser cladding in recent years." *Sci. Mech. Eng.* 30.2 (2021): 69-77.

[7].Huang, Zilin, et al. "Process improvement in laser hot wire cladding for martensitic stainless steel based on the Taguchi method." *Frontiers of Mechanical Engineering* 11.3 (2016): 242-249.

[8].Krishnan, Arun, and Fengzhou Fang. "Review on mechanism and process of surface polishing using lasers." *Frontiers of Mechanical Engineering* 14.3 (2019): 299-319.

[9].Dadbakhsh, Sasan, Liang Hao, and Choon Yen Kong. "Surface finish improvement of LMD samples using laser polishing." Virtual and Physical Prototyping 5.4 (2010): 215-221.

[10].Pawlowski, L. "Thick laser coatings: A review." *Journal of thermal spray technology* 8.2 (1999): 279-295.

[11].Patel, S., Sandip B. Patel, and Anup B. Patel. "A review on laser engraving process." *Int. J. Sci. Res. Dev* 3 (2015): 247-250.

[12].Muthukumaran, G., and P. Dinesh Babu. "Laser transformation hardening of various steel grades using different laser types." *Journal of the Brazilian Society of Mechanical Sciences and Engineering* 43.2 (2021): 103.

[13].Mishra, Yadvendra Kumar, et al. "Inclined laser drilling in glass fiber reinforced plastic using Nd: YAG laser." *Journal of the Brazilian Society of Mechanical Sciences and*

Engineering 44.2 (2022): 66.

[14].Manshoori Yeganeh, A., M. R. Movahhedy, and S. Khodaygan. "An efficient scanning algorithm for improving accuracy based on minimising part warping in selected laser sintering process." *Virtual and Physical Prototyping* 14.1 (2019): 59-78.

[15].Chen, Zhixiang, et al. "Laser vision sensing based on adaptive welding for aluminum alloy." *Frontiers of mechanical Engineering in China* 2.2 (2007): 218-223.

[16].Dumitrescu, Petre, et al. "High-power diode laser assisted hard turning of AISI D2 tool steel." *International Journal of Machine Tools and Manufacture* 46.15 (2006): 2009-2016.

[17].Kong, Xianjun, et al. "Numerical and experimental investigations on the laser assisted machining of the TC6 titanium alloy." *Journal of Manufacturing Processes* 96 (2023): 68-79.

[18].Pan, Z., Lu, YT., Lin, YF. et al. Analytical model for force prediction in laser-assisted milling of IN718. Int J Adv Manuf Technol 90, 2935–2942 (2017).

[19].Qi, J., K. L. Wang, and Y. M. Zhu. "A study on the laser marking process of stainless steel." *Journal of Materials Processing Technology* 139.1-3 (2003): 273-276.

[20].Nabavi, Seyedeh Fatemeh, and Hamid Dalir. "A comprehensive review of laser-assisted manufacturing processes for thermoset composites: Physical behavior, fundamental mechanisms of the process, and applications." *Journal of Manufacturing Processes* 148 (2025): 99-149.

[21].Nabavi, Seyedeh Fatemeh, and Hamid Dalir. "A review on laser-assisted manufacturing process of thermoset composites: A review of fundamentals, processes, scientific modelling, challenges and prospective." *Optics & Laser Technology* 181 (2025): 111713.

[22].Fiocchi, Jacopo, Ausonio Tuissi, and Carlo Alberto Biffi. "Heat treatment of aluminium alloys produced by laser powder bed fusion: A review." *Materials & Design* 204 (2021): 109651.

[23].Kusoglu, Ihsan Murat, Bilal Gökce, and Stephan Barcikowski. "Research trends in laser powder bed fusion of Al alloys within the last decade." *Additive Manufacturing* 36 (2020): 101489.

[24].Kotadia, Hiren R., et al. "A review of Laser Powder Bed Fusion Additive Manufacturing of aluminium alloys: Microstructure and properties." *Additive Manufacturing* 46 (2021): 102155.

[25].Panwisawas, Chinnapat, Yuanbo T. Tang, and Roger C. Reed. "Metal 3D printing as a disruptive technology for superalloys." *Nature communications* 11.1 (2020): 2327.

[26].Wang, Jincheng, et al. "Understanding melt pool characteristics in laser powder bed fusion: An overview of single-and multi-track melt pools for process optimization." *Advanced Powder Materials* 2.4 (2023): 100137.

[27].Wu, Liang, et al. "Hot work tool steel processed by laser powder bed fusion: a review on most relevant influencing factors." *Advanced Engineering Materials* 23.7 (2021): 2100049.

[28].Martin A A, Calta N P, Khairallah S A, Wang J, Depond P J, Fong A Y, et al. Dynamics of pore formation during laser powder bed fusion additive manufacturing. Nature communications, 2019, 10(1): 1987

[29].Grasso M, Colosimo B M. Process defects and in situ monitoring methods in metal powder bed fusion: a review. Measurement Science and Technology, 2017, 28(4): 044005

[30].Tusher, Md Mehide Hasan, and Ayhan Ince. "A systematic review on high cycle and very high cycle fatigue behavior of laser powder bed fused (L-PBF) Al-Si alloys." *Engineering Failure Analysis* 154 (2023): 107667.

[31].Kotadia, Hiren R., et al. "A review of Laser Powder Bed Fusion Additive Manufacturing of aluminium alloys: Microstructure and properties." *Additive Manufacturing* 46 (2021): 102155.

[32].Farshidianfar, Anooshiravan, Seyedeh Fatemeh Nabavi, and Mohammad Hossein Farshidianfar. The Laser Manufacturing Process: Fundamentals of Process and Applications. CRC Press, 2024.

[33].J.N. Domfang Ngnekou, Y. Nadot, G. Henaff, J. Nicolai, W.H. Kan, J.M. Cairney, and L. Ridosz, Int. J. Fatigue 119, 160 (2019).

[34].W. Schneller, M. Leitner, S. Springer, F. Gru¨n, and M. Taschauer, J. Manuf. Mater. Process. 3, 16 (2019).

[35].Maleki E, Bagherifard S, Sabouri F, Guagliano M. Effects of hybrid post-treatments on fatigue behaviour of notched LPBF AlSi10Mg: experimental and deep learning approaches. Procedia Struct Integr 2021;34:141–53.

[36].Maleki E, Bagherifard S, Bandini M, Guagliano M. Surface post-treatments for metal additive manufacturing: Progress, challenges, and opportunities. Addit Manuf 2021;37:101619.

[37].Nabavi, Seyedeh Fatemeh, Anooshiravan Farshidianfar, and Hamid Dalir. "Comprehensive review: Advancements in modelling geometrical and mechanical characteristics of laser powder bed fusion process." *Optics & Laser Technology* 180 (2025): 111480.

[38].Kim, Jaewoong, et al. "Calibration of laser penetration depth and absorptivity in finite element method based modelling of powder bed fusion melt pools." *Metals and Materials International* 26.6 (2020): 891-902.

[39].Chen, Qian, et al. "Elucidating the effect of preheating temperature on melt pool morphology variation in Inconel 718 laser powder bed fusion via simulation and experiment." *Additive Manufacturing* 37 (2021): 101642.

[40].Ninpetch, Patiparn, Prasert Chalermkarnnon, and Pruet Kowitwarangkul. "Multiphysics

simulation of thermal-fluid behavior in laser powder bed fusion of H13 steel: influence of layer thickness and energy input." *Metals and Materials International* 29.2 (2023): 536-551.

[41].Hu, Ruixiong, Stephen Rock, and Antoinette M. Maniatty. "Heat transfer finite element model for laser powder-bed fusion on consolidated simulation geometry." *Computational Mechanics* 71.4 (2023): 745-763.

[42].Zhang, Zhidong, et al. "3-Dimensional heat transfer modelling for laser powder-bed fusion additive manufacturing with volumetric heat sources based on varied thermal conductivity and absorptivity." *Optics & Laser Technology* 109 (2019): 297-312.

[43].Li, E. L., et al. "A three-phase model for simulation of heat transfer and melt pool behaviour in laser powder bed fusion process." *Powder technology* 381 (2021): 298-312.

[44].Noll, I., et al. "A micromechanically motivated multiscale approach for residual distortion in laser powder bed fusion processes." *Additive Manufacturing* 60 (2022): 103277.

[45].Mirkoohi, Elham, et al. "Analytical modelling of residual stress in laser powder bed fusion considering part's boundary condition." *Crystals* 10.4 (2020): 337.

[46].Wang, Wenjia, Hamid Garmestani, and Steven Y. Liang. "Prediction of molten pool size and vapor depression depth in keyhole melting mode of laser powder bed fusion." *The International Journal of Advanced Manufacturing Technology* 119.9 (2022): 6215-6223.

[47].Noll, Isabelle, Thorsten Bartel, and Andreas Menzel. "A thermodynamically consistent phase transformation model for multiphase alloys: application to Ti 6 Al 4 V in laser powder bed fusion processes." *Computational Mechanics* 74.6 (2024): 1319-1338.

[48].Huang, Wei, et al. "Analytical model of quantitative texture prediction considering heat transfer based on single-phase material in laser powder bed fusion." *Journal of Manufacturing and Materials Processing* 8.2 (2024): 70.

[49].Wang, Wenjia, Hamid Garmestani, and Steven Y. Liang. "Prediction of upper surface roughness in laser powder bed fusion." *Metals* 12.1 (2021): 11.

[50].Zöller, C., N. A. Adams, and S. Adami. "Numerical investigation of balling defects in laser-based powder bed fusion of metals with Inconel 718." *Additive Manufacturing* 73 (2023): 103658.

[51].Agrawal, Ankur K., Behzad Rankouhi, and Dan J. Thoma. "Predictive process mapping for laser powder bed fusion: A review of existing analytical solutions." *Current Opinion in Solid State and Materials Science* 26.6 (2022): 101024.

[52].Kaushik, Harish Chandra, Mahdi Habibnejad Korayem, and Amir Hadadzadeh. "Determination of α to β phase transformation kinetics in laser-powder bed fused Ti–6Al–2Sn–4Zr–2Mo-0.08 Si and Ti–6Al–4V alloys." *Materials Science and Engineering: A* 860 (2022): 144294.

[53].Kotsiantis, Sotiris B., Ioannis Zaharakis, and P. Pintelas. "Supervised machine learning: A review of classification techniques." *Emerging artificial intelligence applications in computer engineering* 160.1 (2007): 3-24.

[54].Alloghani, Mohamed, et al. "A systematic review on supervised and unsupervised machine learning algorithms for data science." *Supervised and unsupervised learning for data science* (2020): 3-21.

[55].Gu, Zhaochen, et al. "A universal predictor-based machine learning model for optimal process maps in laser powder bed fusion process." *Journal of Intelligent Manufacturing* 34.8 (2023): 3341-3363.

[56].Tapia, Gustavo, et al. "Gaussian process-based surrogate modelling framework for process planning in laser powder-bed fusion additive manufacturing of 316L stainless steel." *The International Journal of Advanced Manufacturing Technology* 94.9 (2018): 3591-3603.

[57].Paulson, Noah H., et al. "Correlations between thermal history and keyhole porosity in laser powder bed fusion." *Additive Manufacturing* 34 (2020): 101213.

[58].Luo, Y. W., et al. "Pore-affected fatigue life scattering and prediction of additively manufactured Inconel 718: An investigation based on miniature specimen testing and machine learning approach." *Materials Science and Engineering: A* 802 (2021): 140693.

[59].Muhammad, Waqas, et al. "A machine learning framework to predict local strain distribution and the evolution of plastic anisotropy & fracture in additively manufactured alloys." *International Journal of Plasticity* 136 (2021): 102867.

[60].Tapia, Gustavo, et al. "Gaussian process-based surrogate modelling framework for process planning in laser powder-bed fusion additive manufacturing of 316L stainless steel." *The International Journal of Advanced Manufacturing Technology* 94.9 (2018): 3591-3603.

[61].Zhu, Qiming, Zeliang Liu, and Jinhui Yan. "Machine learning for metal additive manufacturing: predicting temperature and melt pool fluid dynamics using physics-informed neural networks." *Computational Mechanics* 67.2 (2021): 619-635.

[62].Garg, A., Jasmine Siu Lee Lam, and M. M. Savalani. "A new computational intelligence approach in formulation of functional relationship of open porosity of the additive manufacturing process." *The International Journal of Advanced Manufacturing Technology* 80.1 (2015): 555-565.

[63].Heigel, Jarred C., and Brandon M. Lane. "Measurement of the melt pool length during single scan tracks in a commercial laser powder bed fusion process." *Journal of Manufacturing Science and Engineering* 140.5 (2018): 051012.

[64].Gan, Zhengtao, et al. "Benchmark study of thermal behavior, surface topography, and dendritic microstructure in selective laser melting of Inconel 625." *Integrating Materials and Manufacturing Innovation* 8.2 (2019): 178-193.

[65].Özel, Tuğrul, et al. "Focus variation measurement and prediction of surface texture parameters using machine learning in laser powder bed fusion." *Journal of manufacturing science and engineering* 142.1 (2020).

[66].Liu, Chao, et al. "Machine Learning-enabled feedback loops for metal powder bed fusion additive manufacturing." *Procedia Computer Science* 176 (2020): 2586-2595.

[67].Grasso, Marco, and Bianca Maria Colosimo. "Process defects and in situ monitoring methods in metal powder bed fusion: a review." *Measurement Science and Technology* 28.4 (2017): 044005.

[68].Yadav, Pinku, et al. "In situ monitoring systems of the SLM process: On the need to develop machine learning models for data processing." *Crystals* 10.6 (2020): 524.

[69].Mahmoudi, Mohamad, Ahmed Aziz Ezzat, and Alaa Elwany. "Layerwise anomaly detection in laser powder-bed fusion metal additive manufacturing." *Journal of Manufacturing Science and Engineering* 141.3 (2019): 031002.

[70].Mitchell, John A., et al. "Linking pyrometry to porosity in additively manufactured metals." *Additive Manufacturing* 31 (2020): 100946.

[71].Singh, A., et al. "Modelling of direct metal laser sintering of EOS DM20 bronze using neural networks and genetic algorithms." *Proceedings of the 37th international MATADOR conference*. Berlin/Heidelberg, Germany: Springer Science & Business Media, 2012.

[72].Gobert, Christian, et al. "Application of supervised machine learning for defect detection during metallic powder bed fusion additive manufacturing using high resolution imaging." *Additive Manufacturing* 21 (2018): 517-528.

[73].Snow, Zackary, et al. "Toward in-situ flaw detection in laser powder bed fusion additive manufacturing through layerwise imagery and machine learning." *Journal of Manufacturing Systems* 59 (2021): 12-26.

[74].Caggiano, Alessandra, et al. "Machine learning-based image processing for on-line defect recognition in additive manufacturing." *CIRP annals* 68.1 (2019): 451-454.

[75].Shevchik, Sergey A., et al. "Acoustic emission for in situ quality monitoring in additive manufacturing using spectral convolutional neural networks." *Additive Manufacturing* 21 (2018): 598-604.

[76].Shevchik, Sergey A., et al. "Deep learning for in situ and real-time quality monitoring in additive manufacturing using acoustic emission." *IEEE Transactions on Industrial Informatics* 15.9 (2019): 5194-5203.

[77].Asadi, Farshid, et al. "Gaussian process (GP)-based learning control of selective laser melting process." *2021 American Control Conference (ACC)*. IEEE, 2021.

[78].Reiff, Colin, et al. "Learning feedforward control for laser powder bed fusion." *Procedia CIRP* 96 (2021): 127-132.

[79].Liu X, Zhao C, Zhou X, Shen Z, Liu W. Microstructure of selective laser melted AlSi10Mg alloy. Mater Des 2019;168:107677.

[80].Tang M, Pistorius PC, Narra S, Beuth JL. Rapid Solidification: Selective Laser Melting of AlSi10Mg. Jom 2016;68:960–6.

[81].Yadroitsev I, Smurov I. Surface morphology in selective laser melting of metal powders. Phys Procedia 2011;12:26470.

[82].Maleki E, Bagherifard S, Guagliano M. Application of artificial intelligence to optimize the process parameters effects on tensile properties of Ti-6Al-4V fabricated by laser powder-bed fusion. Int J Mech Mater Des 2022;18:199222.

[83].Sames WJ, List FA, Pannala S, Dehoff RR, Babu SS. The metallurgy and processing science of metal additive manufacturing. Int Mater Rev 2016;61:315–60.

[84].Zhang Z, Sun C, Xu X, Liu L. Surface quality and forming characteristics of thinwall aluminium alloy parts manufactured by laser assisted MIG arc additive manufacturing. Int J Light Mater Manuf 2018;1:89–95.

[85].Li R, Liu J, Shi Y, Wang L, Jiang W. Balling behavior of stainless steel and nickel powder during selective laser melting process. Int J Adv Manuf Technol 2012;59: 1025–35.

[86].Denti, Lucia, and Antonella Sola. "On the effectiveness of different surface finishing techniques on A357. 0 parts produced by laser-based powder bed fusion: surface roughness and fatigue strength." *Metals* 9.12 (2019): 1284.

[87].Fiocchi, Jacopo, Ausonio Tuissi, and Carlo Alberto Biffi. "Heat treatment of aluminium alloys produced by laser powder bed fusion: A review." *Materials & Design* 204 (2021): 109651.

[88].Kreitcberg, Alena, Vladimir Brailovski, and Sylvain Turenne. "Effect of heat treatment and hot isostatic pressing on the microstructure and mechanical properties of Inconel 625 alloy processed by laser powder bed fusion." *Materials Science and Engineering: A* 689 (2017): 1-10.

[89].Çevik, Zihni Alp, Koray Özsoy, and Ali Erçetin. "The effect of machining processes on the physical and surface morphology of Ti6Al4V specimens produced through powder bed fusion additive manufacturing." *International Journal of 3D Printing Technologies and Digital Industry* 5.2 (2021): 187-194.

[90].Yang, Kyung-Tae, et al. "Investigation of laser powder bed fusion manufacturing and post-processing for surface quality of as-built 17-4PH stainless steel." *Surface and Coatings Technology* 422 (2021): 127492.

[91].Yadollahi, Aref, et al. "Effects of process time interval and heat treatment on the mechanical and microstructural properties of direct laser deposited 316L stainless steel." *Materials*

Science and Engineering: A 644 (2015): 171-183.

[92].Kong, Decheng, et al. "Mechanical properties and corrosion behavior of selective laser melted 316L stainless steel after different heat treatment processes." *Journal of Materials Science & Technology* 35.7 (2019): 1499-1507.

[93].Montero Sistiaga, M. L., et al. "Effect of heat treatment of 316L stainless steel produced by selective laser melting (SLM)." (2016).

[94].Kong, Decheng, et al. "Heat treatment effect on the microstructure and corrosion behavior of 316L stainless steel fabricated by selective laser melting for proton exchange membrane fuel cells." *Electrochimica Acta* 276 (2018): 293-303.

[95].Zhong, Yuan, et al. "Intragranular cellular segregation network structure strengthening 316L stainless steel prepared by selective laser melting." *Journal of Nuclear Materials* 470 (2016): 170-178.

[96].Shen, Bingnan, et al. "Influence of laser post-processing on pore evolution of Ti–6Al–4V alloy by laser powder bed fusion." *Journal of Alloys and Compounds* 818 (2020): 152845.

[97].Ahmed, Aymen A., et al. "The effect of shot peening parameters and hydroxyapatite coating on surface properties and corrosion behavior of medical grade AISI 316L stainless steel." *Surface and Coatings Technology* 280 (2015): 347-358.

[98].Bagherifard, Sara, et al. "Fatigue behavior of notched steel specimens with nanocrystallized surface obtained by severe shot peening." *Materials & Design* 45 (2013): 497-503.

[99].Fridrici, V., S. Fouvry, and Ph Kapsa. "Effect of shot peening on the fretting wear of Ti–6Al–4V." *Wear* 250.1-12 (2001): 642-649.

[100].Liu, Z. G., H. J. Fecht, and M. Umemoto. "Microstructural evolution and nanocrystal formation during deformation of Fe–C alloys." *Materials Science and Engineering: A* 375 (2004): 839-843.

[101].Lu, K. A. L. J., and Jian Lu. "Nanostructured surface layer on metallic materials induced by surface mechanical attrition treatment." *Materials Science and Engineering: A* 375 (2004): 38-45.

[102].Sun, Yong, Richard Bailey, and Adam Moroz. "Surface finish and properties enhancement of selective laser melted 316L stainless steel by surface mechanical attrition treatment." *Surface and Coatings Technology* 378 (2019): 124993.

[103].AlMangour, Bandar, and Jenn-Ming Yang. "Improving the surface quality and mechanical properties by shot-peening of 17-4 stainless steel fabricated by additive manufacturing." *Materials & Design* 110 (2016): 914-924.

[104].AlMangour, Bandar, and Jenn-Ming Yang. "Improving the surface quality and mechanical properties by shot-peening of 17-4 stainless steel fabricated by additive manufacturing." *Materials & Design* 110 (2016): 914-924.

[105].Wang, Di, et al. "Theoretical and experimental study on surface roughness of 316L stainless steel metal parts obtained through selective laser melting." *Rapid Prototyping Journal* 22.4 (2016): 706-716.

[106].Kaynak, Yusuf, and Ozhan Kitay. "The effect of post-processing operations on surface characteristics of 316L stainless steel produced by selective laser melting." *Additive Manufacturing* 26 (2019): 84-93.

[107].Soundararajan, Balaji, et al. "Review on modelling techniques for powder bed fusion processes based on physical principles." *Additive Manufacturing* 47 (2021): 102336.

[108].Bauereiß, A., T. Scharowsky, and C. Körner. "Defect generation and propagation mechanism during additive manufacturing by selective beam melting." *Journal of Materials Processing Technology* 214.11 (2014): 2522-2528.

[109].Gu, Heng, et al. "Multi-physics modelling of molten pool development and track formation in multi-track, multi-layer and multi-material selective laser melting." *International Journal of Heat and Mass Transfer* 151 (2020): 119458.

[110].Le, Kim Quy, et al. "Discontinuity of overhanging melt track in selective laser melting process." *International Journal of Heat and Mass Transfer* 162 (2020): 120284.

[111].Flint, Thomas F., et al. "A thermal fluid dynamics framework applied to multi-component substrates experiencing fusion and vaporisation state transitions." *Communications Physics* 3.1 (2020): 196.

[112].Vallabh, Chaitanya Krishna Prasad, et al. "Predicting melt pool depth and grain length using multiple signatures from in-situ single camera two-wavelength imaging pyrometry for laser powder bed fusion." *Journal of Materials Processing Technology* 308 (2022): 117724.

[113].Incropera, Frank P., and David P. De Witt. "Fundamentals of heat and mass transfer." (1985).

[114].Fassani, R. N. S., and O. V. Trevisan. "Analytical modelling of multipass welding process with distributed heat source." *Journal of the Brazilian Society of Mechanical Sciences and Engineering* 25 (2003): 302-305.

[115].Lindgren, Lars-Erik. *Computational welding mechanics*. Elsevier, 2014.

[116].Behúlová, M., and E. Babalová. "Heat source models for numerical simulation of laser welding processes–a short review." *Journal of Physics: Conference Series*. Vol. 2712. No. 1. IOP Publishing, 2024.

[117].Goldak, John, Aditya Chakravarti, and Malcolm Bibby. "A new finite element model for welding heat sources." *Metallurgical transactions B* 15.2 (1984): 299-305.

[118].Farias, R. M., P. R. F. Teixeira, and L. O. Vilarinho. "Variable profile heat source models for numerical simulations of arc welding processes." *International Journal of Thermal Sciences* 179 (2022): 107593.

[119].Jia, Xiaolei, et al. "A new method to estimate heat source parameters in gas metal arc

welding simulation process." *Fusion Engineering and Design* 89.1 (2014): 40-48.

[120].Ravisankar, A., et al. "Influence of welding speed and power on residual stress during gas tungsten arc welding (GTAW) of thin sections with constant heat input: A study using numerical simulation and experimental validation." *Journal of Manufacturing Processes* 16.2 (2014): 200-211.

[121].Chukkan, Jazeel Rahman, et al. "Simulation of laser butt welding of AISI 316L stainless steel sheet using various heat sources and experimental validation." *Journal of materials processing technology* 219 (2015): 48-59.

[122].Moslemi, Navid, et al. "A novel systematic numerical approach on determination of heat source parameters in welding process." *journal of materials research and technology* 18 (2022): 4427-4444.

[123].Chujutalli, John H., Marcelo I. Lourenço, and Segen F. Estefen. "Experimental-based methodology for the double ellipsoidal heat source parameters in welding simulations." *Marine Systems & Ocean Technology* 15.2 (2020): 110-123.

[124].Kik, Tomasz. "Heat source models in numerical simulations of laser welding." *Materials* 13.11 (2020): 2653.

[125].Deng, Dean, Wei Liang, and Hidekazu Murakawa. "Determination of welding deformation in fillet-welded joint by means of numerical simulation and comparison with experimental measurements." *Journal of Materials Processing Technology* 183.2-3 (2007): 219-225.

[126].Rong, Youmin, et al. "Laser penetration welding of ship steel EH36: A new heat source and application to predict residual stress considering martensite phase transformation." *Marine Structures* 61 (2018): 256-267.

[127].Farrokhi F, Endelt B and Kristiansen M 2019 Opt. Laser Technol. 111 671–686

[128].A. Quarteroni and A. Valli. Numerical Approximation of Partial Differential Equations. Springer Verlag, Heidelberg, 1994.

[129].M. Raissi, P. Perdikaris, and G.E. Karniadakis. Physics-informed neural networks: A deep learning framework for solving forward and inverse problems involving nonlinear partial differential equations. Journal of Computational Physics, 378:686 – 707, 2019.

[130].George Em Karniadakis, Ioannis G. Kevrekidis, Lu Lu, Paris Perdikaris, Sifan Wang, and Liu Yang. Physics-informed machine learning. Nature Reviews Physics, 3(6):422 – 440, 2021.

[131].Salvatore Cuomo, Vincenzo Schiano Di Cola, Fabio Giampaolo, Gianluigi Rozza, Maziar Raissi, and Francesco Piccialli. Scientific machine learning through physics–informed neural networks: Where we are and what’s next. Journal of Scientific Computing, 92:88, 2022.

[132].Yeonjong Shin, Zhongqiang Zhang, and George Em Karniadakis. Theoretical foundations

of physics-informed neural networks and deep neural operators: A brief review. In Siddhartha Mishra and Alex Townsend, editors, Numerical Analysis Meets Machine Learning, volume 25 of Handbook of Numerical Analysis, pages 293–358. Elsevier, 2024.

[133].A. Quarteroni, F. Saleri, and P. Gervasio. Scientific Computing. 4th ed. Springer Berlin, Heidelberg, 2014.

[134].I.E. Lagaris, A.C. Likas, and D.G. Papageorgiou. Neural-network methods for boundary value problems with irregular boundaries. IEEE Transactions on Neural Networks, 11(5):1041–1049, 2000.

[135].George Em Karniadakis, Ioannis G. Kevrekidis, Lu Lu, Paris Perdikaris, Sifan Wang, and Liu Yang. Physics-informed machine learning. Nature Reviews Physics, 3(6):422 – 440, 2021.

[136].Sifan Wang, Xinling Yu, and Paris Perdikaris. When and why PINNs fail to train: A neural tangent kernel perspective. Journal of Computational Physics, 449:110768, 2022.

[137].Matthew Tancik, Pratul Srinivasan, Ben Mildenhall, Sara Fridovich-Keil, Nithin Raghavan, Utkarsh Singhal, Ravi Ramamoorthi, Jonathan Barron, and Ren Ng. Fourier features let networks learn high frequency functions in low dimensional domains. In H. Larochelle, M. Ranzato, R. Hadsell, M.F. Balcan, and H. Lin, editors, Advances in Neural Information Processing Systems, volume 33, pages 7537–7547. Curran Associates, Inc., 2020.

[138].Sifan Wang, Yujun Teng, and Paris Perdikaris. Understanding and mitigating gradient flow pathologies in physics-informed neural networks. SIAM Journal on Scientific Computing, 43(5):A3055A3081, 2021.

[139].Yeonjong Shin, J ́erˆome Darbon, and George Em Karniadakis. On the convergence of physics informed neural networks for linear second-order elliptic and parabolic type PDEs. Communications in Computational Physics, 28(5):2042 – 2074, 2020.

[140].Roberto Molinaro. Applications of Deep Learning to Scientific Computing. PhD thesis, ETH Zurich, 2023.

[141].Siddhartha Mishra and Roberto Molinaro. Estimates on the generalization error of physicsinformed neural networks for approximating a class of inverse problems for PDEs. IMA Journal of Numerical Analysis, 42(2):981 – 1022, 2022.

[142].Siddhartha Mishra and Roberto Molinaro. Estimates on the generalization error of physicsinformed neural networks for approximating PDEs. IMA Journal of Numerical Analysis, 43(1):143, 2023.

[143].J. Nocedal. Theory of algorithms for unconstrained optimization, pages 199–242. Cambridge University Press, 1991.

[144].J.-L. Lions. Optimal Control of Systems Governed by Partial Differential Equations. Springer Verlag, New York, 1971.

[145].A. Manzoni, A. Quarteroni, and S. Salsa. Optimal Control of Partial Differential Equations. Analysis, Approximation, and Applications. Springer Cham, 2022.

[146].Francesco Regazzoni, Stefano Pagani, Alessandro Cosenza, Alessandro Lombardi, and Alfio Quarteroni. A physics-informed multi-fidelity approach for the estimation of differential equations parameters in low-data or large-noise regimes. Rendiconti Lincei, 32(3):437–470, 2021.

[147].I.E. Lagaris, A.C. Likas, and D.G. Papageorgiou. Neural-network methods for boundary value problems with irregular boundaries. IEEE Transactions on Neural Networks, 11(5):1041–1049, 2000.

[148].Isaac Elias Lagaris, Aristidis Likas, and Dimitrios I. Fotiadis. Artificial neural networks for solving ordinary and partial differential equations. IEEE Transactions on Neural Networks, 9(5):987 1000, 1998.

[149].Yeonjong Shin, Zhongqiang Zhang, and George Em Karniadakis. Theoretical foundations of physics-informed neural networks and deep neural operators: A brief review. In Siddhartha Mishra and Alex Townsend, editors, Numerical Analysis Meets Machine Learning, volume 25 of Handbook of Numerical Analysis, pages 293–358. Elsevier, 2024.

[150].Xuhui Meng and George Em Karniadakis. A composite neural network that learns from multifidelity data: Application to function approximation and inverse pde problems. Journal of Computational Physics, 401:109020, 2020.

[151].E. Kharazmi, Z. Zhang, and G. E. Karniadakis. Variational physics-informed neural networks for solving partial differential equations. arXiv preprint arXiv:1912.00873, 2019.

[152].Ehsan Kharazmi, Zhongqiang Zhang, and George E.M. Karniadakis. hp–VPINNs: Variational physics–informed neural networks with domain decomposition. Computer Methods in Applied Mechanics and Engineering, 374:113547, 2021.

[153].Weinan E and Bing Yu. The Deep Ritz Method: A deep learning-based numerical algorithm for solving variational problems. Communications in Mathematics and Statistics, 6(1):1 – 12, 2018.

[154].C. Wu, H. Wang, Y. Zhang, A new heat source model for keyhole plasma arc welding in fem analysis of the temperature profile, Welding Journal 85 (2006) 284–s–291–s.

[155].F. Farrokhi, B. Endelt, M. Kristiansen, A numerical model for full and partial penetration hybrid laser welding of thick-section steels, Optics & Laser Technology 111 (2019) 671–686.

[156].L. Lu, X. Meng, Z. Mao, G. E. Karniadakis, Deepxde: A deep learning library for solving differential equations, SIAM review 63 (2021) 208–228.

[157].S. Piandoro, A. Fortunato, E. Liverani, A. Ascari, Numerical investigation of pulsed welding on aluminum alloy with a dual-region laser source: Exploring non-equal pulse

parameters, Materials Research Proceedings, 54 (2025) 2130-2140.
[158].European standard EN ISO 6892-1:2009, Metallic materials. Tensile testing. Part 1 – Method of test at room temperature. European Committee for Standardisation, 2009
[159].ISO 1143:2010 - Metallic materials – Rotating bar bending fatigue testing, ISO, 2010.
[160].Raab, M. and Bambach, M., 2023. Fatigue properties of Scalmalloy® processed by laser powder bed fusion in asbuilt, chemically and conventionally machined surface condition. Journal of Materials Processing Technology, 311, p.117811.
[161].A.B. Spierings, K. Dawson, T. Heeling, P.J. Uggowitzer, R. Sch ̈aublin, F. Palm, K. Wegener, Microstructural features of Sc- and Zr-modified Al-Mg alloys processed by selective laser melting, Mater. Des. 115 (2017) 52–63
[162].Cortis, D., Campana, F., Orlandi, D. and Sansone, S., 2023. Strength and fatigue behavior assessment of the SCALMALLOY® material to functionally adapt the performance of L-PBF components within CAE simulations. Progress in Additive Manufacturing, 8(5), pp.933-946.
[163].Dixon, W.J., 1950. Analysis of extreme values. The Annals of Mathematical Statistics, 21(4), pp.488-506.
[164].Dong, Fei, et al. "Improving the surface quality and its mechanism in ultraprecision machining of Al–Mg–Si alloy by multiple high energy shot peening pretreatment." Journal of Materials Research and Technology 30 (2024): 70517064.
[165].Gan, Jin, et al. "Effect of stress shot peening on the microstructure and residual stress of Al18B4O33 whisker reinforced aluminum matrix composite." Surface and Coatings Technology 479 (2024): 130546.
[166].Xu, Juan, and Wenbo Ding. "Investigating the role of shot peening pressure on microstructure, grain structure, and hydrogen embrittlement of age-hardened copper alloy." Vacuum (2025): 114551.
[167].Yang, C., Y. G. Liu, and M. Q. Li. "Characteristics and formation mechanisms of defects in surface layer of TC17 subjected to high energy shot peening." Applied Surface Science 509 (2020): 144711.